USGS
science for a changing world

Modeling 3-D Slope Stability of Coastal Bluffs Using 3-D Ground-Water Flow, Southwestern Seattle, Washington

Scientific Investigations Report 2007–5092

U.S. Department of the Interior
U.S. Geological Survey

Modeling 3-D Slope Stability of Coastal Bluffs, Using 3-D Ground-Water Flow, Southwestern Seattle, Washington

By Dianne L. Brien and Mark E. Reid

Scientific Investigations Report 2007-5092

U.S. Department of the Interior
U.S. Geological Survey

U.S. Department of the Interior
DIRK KEMPTHORNE, Secretary

U.S. Geological Survey
Mark D. Myers, Director

U.S. Geological Survey, Reston, Virginia: 2007

This report and any updates to it are available online at:
http://pubs.usgs.gov/sir/5092/

For product and ordering information:
World Wide Web: http://www.usgs.gov/pubprod
Telephone: 1–888–ASK–USGS

For more information on the USGS—the Federal source for science about the Earth, its natural and living resources, natural hazards, and the environment:
World Wide Web: http://www.usgs.gov
Telephone: 1–888–ASK–USGS

Cataloging-in-Publication data are on file with the Library of Congress (URL http://www.loc.gov/).

Produced in the Western Region, Menlo Park, California
Manuscript approved for publication, May 15, 2007
Text edited by James W. Hendley II
Layout and design by Stephen L. Scott

COVER—Aerial photograph of a deep-seated landslide
(Photograph by Leonard Palmer, FEMA, 1997.)

Contents

Figures

Tables

Modeling 3-D Slope Stability of Coastal Bluffs Using 3-D Ground-Water Flow, Southwestern Seattle, Washington

By Dianne L. Brien and Mark E. Reid

Abstract

Landslides are a common problem on coastal bluffs throughout the world. Along the coastal bluffs of the Puget Sound in Seattle, Washington, landslides range from small, shallow failures to large, deep-seated landslides. Landslides of all types can pose hazards to human lives and property, but deep-seated landslides are of significant concern because their large areal extent can cause extensive property damage. Although many geomorphic processes shape the coastal bluffs of Seattle, we focus on large (greater than 3,000 m^3), deep-seated, rotational landslides that occur on the steep bluffs along Puget Sound. Many of these larger failures occur in advance outwash deposits of the Vashon Drift (Qva); some failures extend into the underlying Lawton Clay Member of the Vashon Drift (Qvlc).

The slope stability of coastal bluffs is controlled by the interplay of three-dimensional (3-D) variations in gravitational stress, strength, and pore-water pressure. We assess 3-D slope-stability using SCOOPS (Reid and others, 2000), a computer program that allows us to search a high-resolution digital-elevation model (DEM) to quantify the relative stability of all parts of the landscape by computing the stability and volume of thousands of potential spherical failures. SCOOPS incorporates topography, 3-D strength variations, and 3-D pore pressures.

Initially, we use our 3-D analysis methods to examine the effects of topography and geology by using heterogeneous material properties, as defined by stratigraphy, without pore pressures. In this scenario, the least-stable areas are located on the steepest slopes, commonly in Qva or Qvlc. However, these locations do not agree well with observations of deep-seated landslides. Historically, both shallow colluvial landslides and deep-seated landslides have been observed near the contact between Qva and Qvlc, and commonly occur in Qva. The low hydraulic conductivity of Qvlc impedes ground-water flow, resulting in elevated pore pressures at the base of Qva, thereby increasing the potential for landslides. Our analysis simulates the ground-water flow using the results of a 3-D ground-water flow model, MODFLOW-2000 (Harbaugh and others, 2000), to generate a 3-D pore-pressure field. Areas of elevated pore pressure reflect the influence of a perched ground-water table in Qva, as well as ground-water convergence in the coastal re-entrants. We obtain a realistic model of deep-seated landsliding by combining 3-D pore pressures with heterogeneous strength properties. The results show the least-stable areas where pore pressures are locally elevated in Qva. We compare our results with records of past landslides. The predicted least-stable areas include two historically active deep-seated landslides and areas adjacent to these landslides.

Introduction

Mass wasting on steep coastal cliffs or bluffs (defined as a cliff with a steep, broad face (Bates and Jackson, 1980)), combined with marine or lacustrine processes, shapes the geomorphic evolution of Earth's coastal cliffs (Emery and Kuhn, 1982; Bird and Schwartz, 1985; Hampton and Griggs, 2004). Coastal cliffs occur throughout the world, along 80 percent of the oceans' shorelines (Emery and Kuhn, 1982). In the United States, retreat of coastal cliffs is a concern on parts of the coasts of the Pacific Ocean, the Great Lakes, and the Atlantic Ocean in New England (Hampton and Griggs, 2004).

Along the steep coastal bluffs of the Puget Sound in Seattle, Washington, landslides are common (Tubbs, 1974, 1975; Gerstel and others, 1997; Baum and others, 1998; Laprade and others, 2000; Shipman, 2001). Here, coastal landslides range from small (a few cubic meters), shallow failures to large (from a few hundred cubic meters to more than a million cubic meters), deep-seated landslides. Deep-seated landslides are less common than other types of landslides but have historically caused severe damage to land and structures (Baum and others, 1998). Although many geomorphic processes shape the coastal bluffs of Seattle, we focus on large (greater than 3,000 m^3), deep-seated, rotational landslides that occur on the steep bluffs along Puget Sound.

Hillslope stability is controlled by several factors, including topography, geology, and hydrology, each of which varies in three dimensions. Ground-water hydrology plays an important role in Seattle and other parts of the world in the stability of coastal cliffs (Sterrett and Edil, 1982; Higgins and Osterkamp, 1990; Norris and Back, 1990, Jaffe and others, 1998).

In Seattle, bluffs consist primarily of relatively flat-lying layers of coarse- and fine-grained glacial deposits. Fine-grained deposits can impede ground-water flow and thereby

cause the formation of perched water tables. Many of the large, deep-seated landslides in Seattle have occurred in the advance outwash deposits of the Vashon Drift (Qva) (Tubbs 1974, 1975; Wait, 2001), a sand-and-gravel unit stratigraphically above the Lawton Clay Member of the Vashon Drift (Qvlc) in the study area. Qvlc is a fine-grained, lower-permeability confining unit. A perched water table can form in Qva above Qvlc, resulting in increased pore pressures and decreased slope stability in Qva.

In addition to the influence of 3-D variations in hydrogeologic properties, topography also controls the distribution of 3-D pore pressures. In uniform material, ground-water flow diverges from topographic highs and converges toward drainages (Dunne, 1990). In a coastal topography, flow can diverge from headlands and converge toward reentrants.

Previous studies have used different approaches for predicting landslide susceptibility in Seattle. Some have used mapping or investigation of historical landslides (Laprade and others, 2000; Wait, 2001); others have used models to describe the physical processes causing instability (Savage and others, 2000a; Debray and Savage, 2001; Montgomery and others, 2001; Harp and others, 2006). Although some of these studies are site specific and analyze the conditions of a specific landslide that has already occurred (Savage and others, 2000a; Debray and Savage, 2001), others attempt to predict slope stability for large areas (Youngmann, 1979; Montgomery and others, 2001; Harp and others, 2006). Youngmann (1979) used slope, geology, and landslide locations to indicate relative stability of coastal slopes. Some studies have compared historical landslide locations in Seattle with models for shallow-landslide initiation (Montgomery and others, 2001; Harp and others, 2006), whereas other studies document the conditions and events during years of abundant landslide occurrence (Harp and others, 1996; Gerstel and others, 1997; Baum and others, 1998; Shipman, 2001).

Whereas simple topographic models for landslide susceptibility may include only slope or curvature of the ground surface, a common geotechnical approach for assessing slope stability is limit-equilibrium analysis. Limit-equilibrium analysis calculates a factor of safety, which is the ratio between driving force and resisting force for a potential failure. Limit-equilibrium analyses frequently use a 1-D or 2-D analysis to describe both the topography and the ground-water pore pressures. For simple topographies, 2-D methods of slope-stability analysis typically estimate lower stability than 3-D methods (Xing, 1988). Bromhead and others (2001) discuss several cases where a 2-D analysis would not be appropriate and would not necessarily give a lower factor of safety. It is difficult to adequately represent a complex topography, estimate potential failure volume, represent localized pore-pressure concentrations, or incorporate other important 3-D variations using a 2-D analysis.

In this study, we analyze the effects of 3-D ground-water flow on 3-D slope stability for a small area in Seattle. We use a 3-D ground-water flow model, MODFLOW-2000 (Harbaugh and others, 2000), to calculate total hydraulic head in each of the hydrogeologic units of our study area. From the results of the ground-water flow model, we then calculate a 3-D pore-pressure distribution for the model domain. To estimate slope stability, we use the 3-D pore-pressure distribution combined with a 3-D extension of Bishop's simplified limit-equilibrium analysis (Reid and others, 2000). We use the limit-equilibrium method to calculate the stability of thousands of potential failure surfaces in a digital landscape of the study area, defined by a high-resolution digital elevation model (DEM). This systematic exploration of the stability of numerous potential failure surfaces results in a map of relative slope stability, or landslide susceptibility, that is based on a sophisticated 3-D portrayal of the principal factors that control landsliding—topography, geologic materials and pore pressures. We then compare our results with observations and maps of the locations of deep-seated landslides.

Background

Location and Physiography

To assess 3-D slope stability in the Seattle area, we selected a study area located near Alki Point and Duwamish Head in southwestern Seattle (fig. 1). In the Seattle region, coastal bluffs that border Puget Sound are susceptible to landsliding. Our study area contains Alki Avenue SW (fig. 1, no. 3), one of two areas in Seattle with the highest reported historical landslide density (Laprade and others, 2000). The other area is Perkins Lane W on Magnolia Bluff (fig. 1, no. 2).

In our study area, the topography consists of flat to gently sloping uplands bordered by the coastal bluffs. The bluffs typically are 75 to 100 m high. The steep portions of the bluffs have slope angles between 30° and 50°, but local areas have slopes greater than 60° (fig. 2), as calculated from a 10-ft (~3-m) resolution DEM (City of Seattle, unpub. data). On the study area's western bluff, a gently sloping bench exists about midslope, and the slopes on this bench are commonly 10° to 20°. The northeastern bluff lacks a bench for much of its length, and is more uniform in slope. Several drainages or reentrants, including Fairmount Gulch on the eastern bluff, shape the landscape and potentially serve as areas of ground-water convergence.

Geology

The coastal bluffs and adjacent ground in Seattle are composed primarily of Quaternary glacial deposits (Mullineaux and others, 1965; Galster and Laprade, 1991; Troost and others, 2005). These geologic materials play an important role in slope stability, due to variations in material strength and hydrogeologic properties.

We use detailed geologic maps (1:12,000 scale) of the study area (Troost and others, 2005) to create layers for

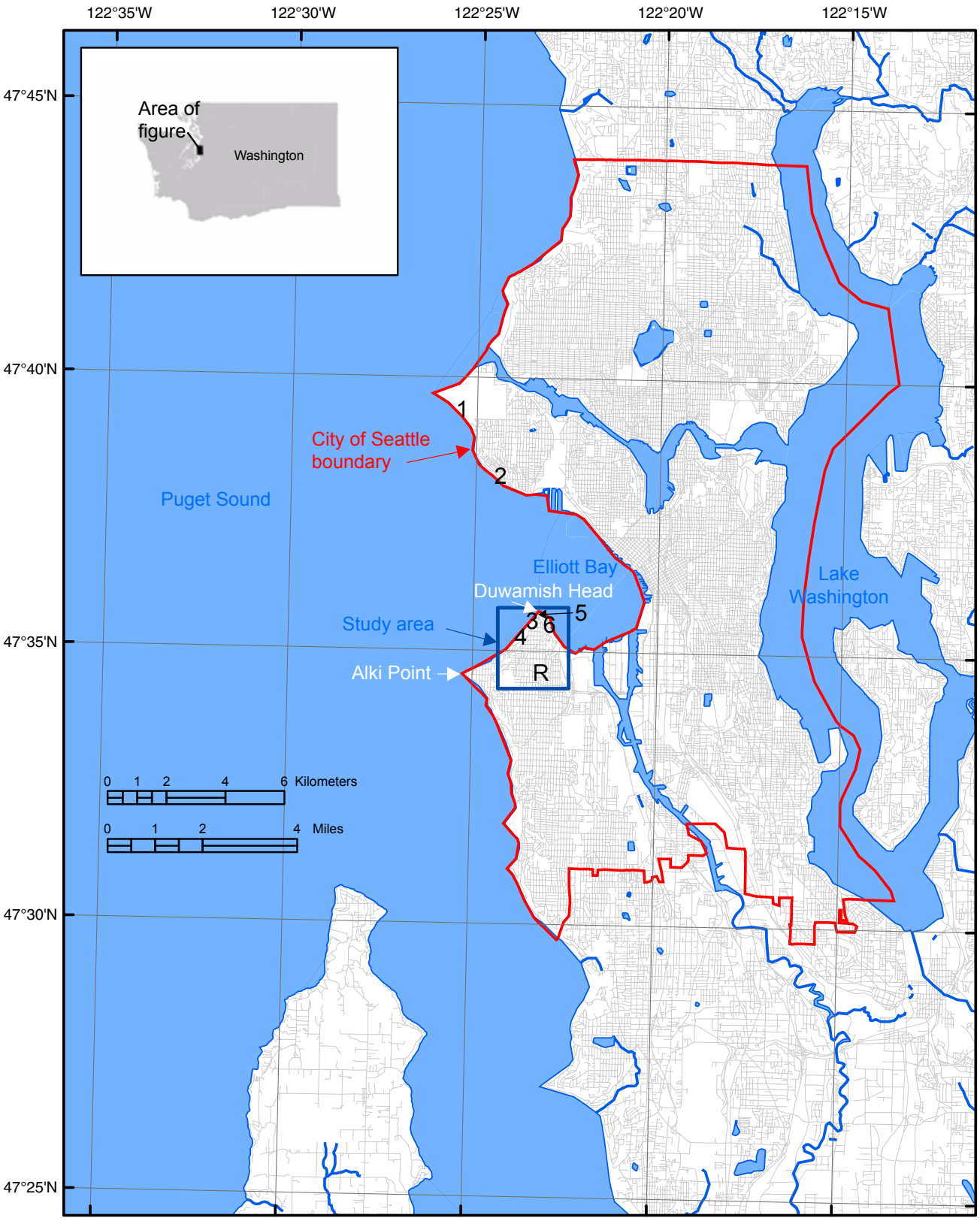

Figure 1. Location map of study area in Seattle, Washington. Black numbers are located near deep-seated landslides discussed in this paper—(1) Discovery Park, (2) Perkins Lane W (Magnolia Bluff), (3) Alki Avenue SW, (4) Bonair Drive, (5) Duwamish Head, and (6) California Way SW. The location of City of Seattle rain gage 14 is indicated by R.

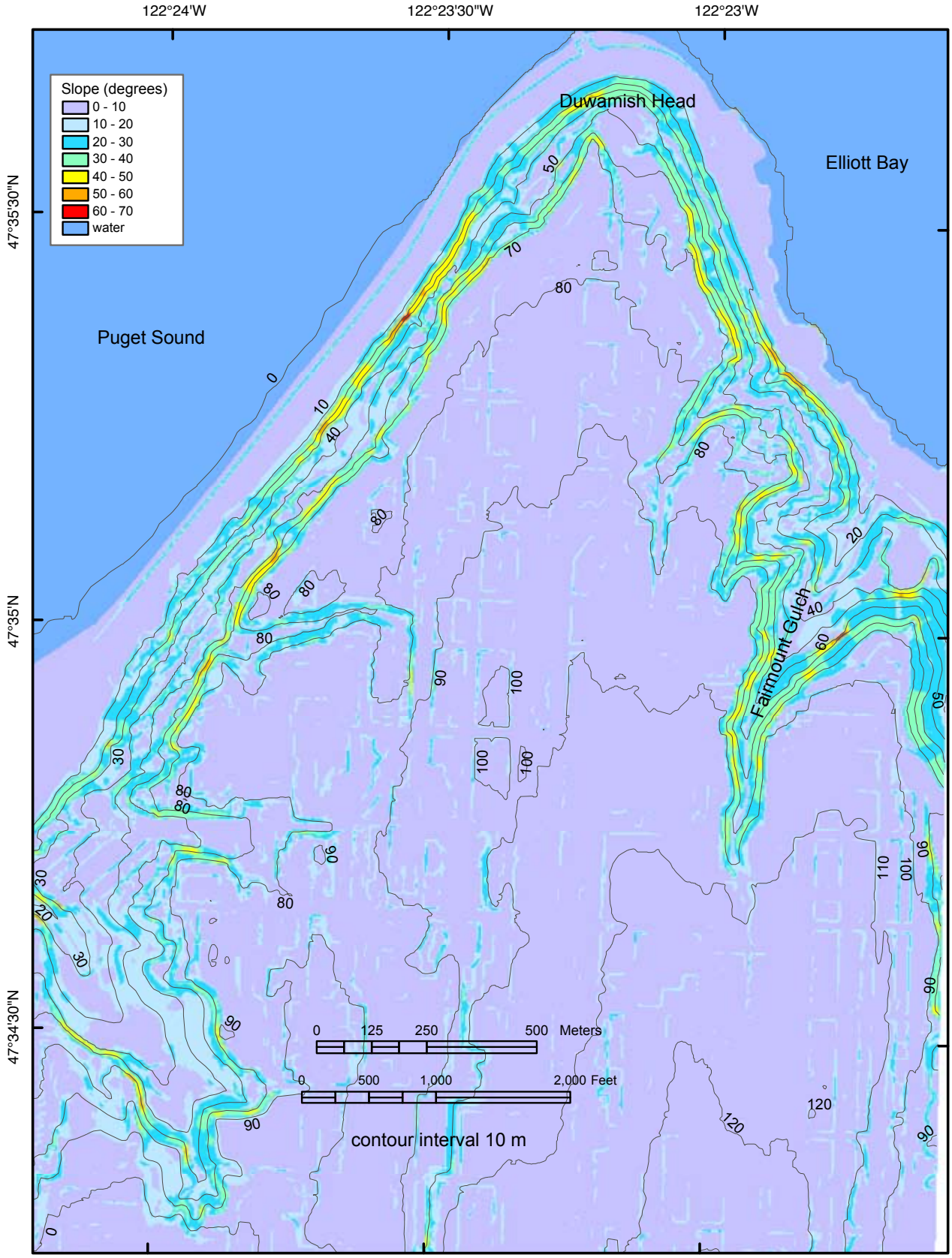

Figure 2. Slope map of study area. Topographic contours and slopes were generated from the 10-ft (~ 3-m) digital elevation model (City of Seattle, unpub. data). Slope was computed for each 10-ft grid cell using ArcGIS™ ArcInfo Workstation SLOPE command. Elevations (in meters) of selected topographic contours (gray lines) are labeled with black text.

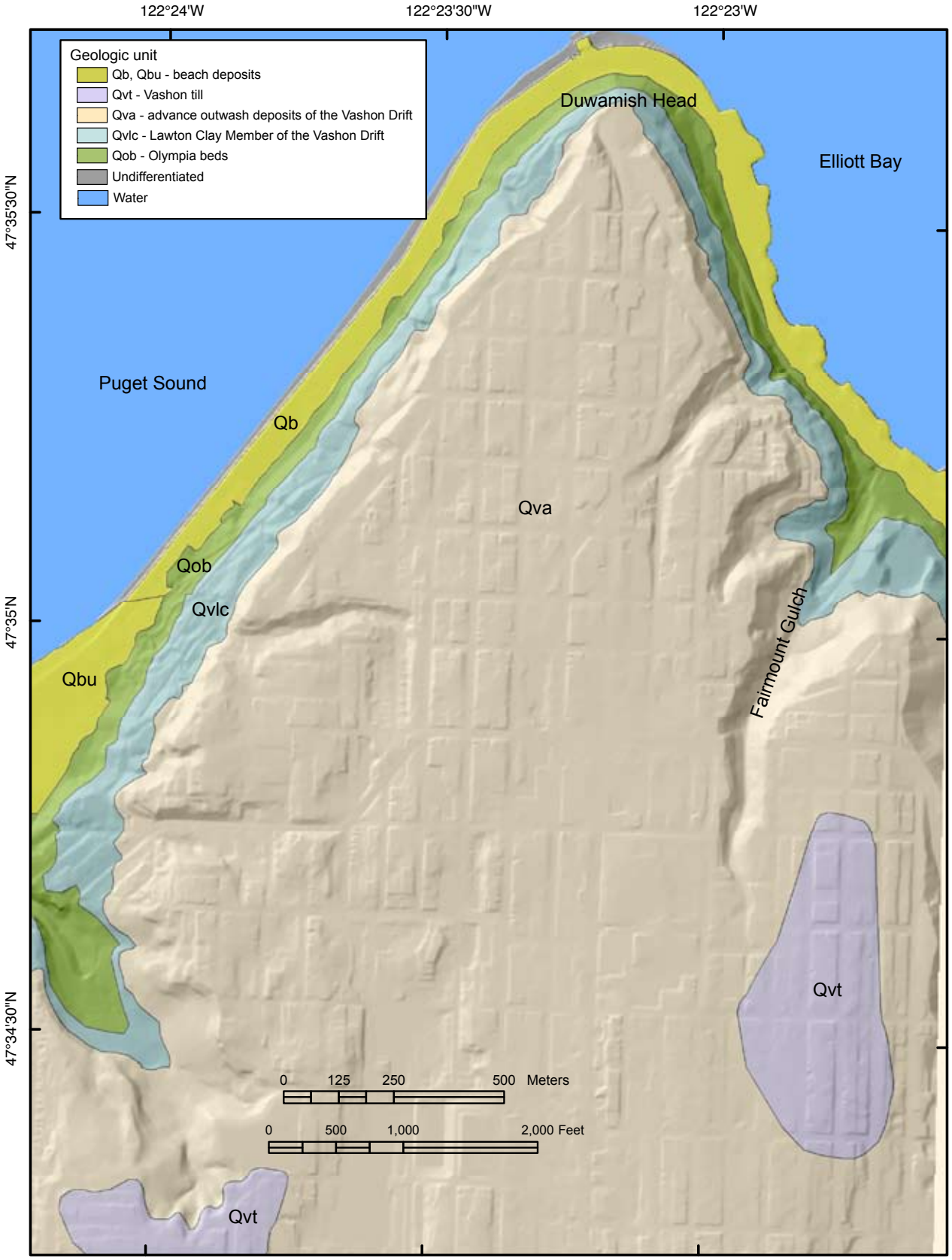

Figure 3. Map of geologic materials of study area (Troost and others, 2005), on shaded relief base generated from 10-ft (~ 3-m) digital elevation model (City of Seattle, unpub. data).

our 3-D analysis. Each of these layers is assigned different hydrogeologic and geotechnical properties. The geologic maps were compiled using field mapping of outcrops and excavations, subsurface exploration data, topographic and geomorphic analyses, and preexisting geologic maps. Figure 3 shows the geologic units exposed in the study area: beach deposits (Qb), uplifted beach deposits (Qbu), Vashon till (Qvt), advance outwash deposits of the Vashon Drift (Qva), Lawton Clay Member of the Vashon Drift (Qvlc), and the Olympia beds (Qob). The following descriptions of these units are derived from Troost and others (2005). Holocene beach deposits (Qb and Qbu) are loose sand and gravel deposited or reworked by wave action. The Vashon till (Qvt) consists of silt, sand, and gravel, glacially transported and deposited under glacial ice. Advance outwash deposits (Qva) are well-sorted sands and gravels deposited by melt-water streams generated by the advancing ice sheet; silt lenses are present in the upper part and common in the lower part. Qva includes the Esperance Sand Member of the Vashon Drift (Mullineaux and others, 1965), but this member is not distinguished in the study area. Qva grades downward, with increasing silt content, into the Lawton Clay Member (Qvlc). Qvlc consists of silt, clayey silt, and silty clay deposited in lowland or proglacial lakes. The Olympia beds (Qob) consist of discontinuously interbedded sand, silt, gravel, and peat and are distinguished from Qvlc by coarser grain size and the presence of organics.

Overlying the glacial and interglacial deposits is a layer of surficial colluvial soil formed by biological activity, slope wash, and mass wasting. Empirical models provide estimates of the thickness of this colluvium, which ranges from 0 to 8 m on the bluffs in the study area (Schulz, 2003; Schulz, written commun., 2004).

Regional Hydrogeology

Vaccaro (1992) and Vaccaro and others (1998) described the hydrogeology of the Puget Sound region as consisting of alluvial, glacial, and interglacial sediments, in which alternating layers of coarse- and fine-grained deposits define units of high hydraulic conductivity (aquifers) and low conductivity (semiconfining or confining units). The direction of ground-water movement is predominantly horizontal in the aquifers and vertical in the confining units.

Within our study area, Vaccaro (1992) and Vaccaro and others (1998) defined three hydrogeologic units above the confining unit formed by the underlying bedrock. The uppermost unit is the Fraser aquifer, generally consisting of Qvt and Qva. Below the Fraser aquifer is a confining unit consisting of Qvlc and fine-grained portions of Qob. Very few water wells have been drilled to depths below approximately 60 to 150 m from the land surface, and the lithology is not well known. These deeper deposits are undifferentiated and are grouped together in a unit referred to as the Puget aquifer.

The basement confining unit of the Puget Sound Aquifer system consists of bedrock of Tertiary age or older. The top of bedrock in our study area lies between 90 to 450 m below sea level (Jones, 1999).

The contact between Qva and the underlying Qvlc controls shallow ground-water flow because of the strong contrast in hydraulic conductivity between these units (Tubbs, 1974, 1975; Laprade and others, 2000). A perennial perched water table is present where Qva overlies Qvlc. During periods of above-average precipitation, a high water table in Qva can promote slope instability (Tubbs, 1974, 1975; Laprade and others, 2000).

Precipitation

The mean annual precipitation in Seattle is 800 to 900 mm (City of Seattle, unpub. data). Figure 4 shows the mean monthly precipitation at a City of Seattle rain gage (City of Seattle, gage 14, unpub. data; Godt, 2004) located in the study area (R in fig. 1). Approximately 80 percent of the precipitation, which typically falls as rain, occurs in the winter season

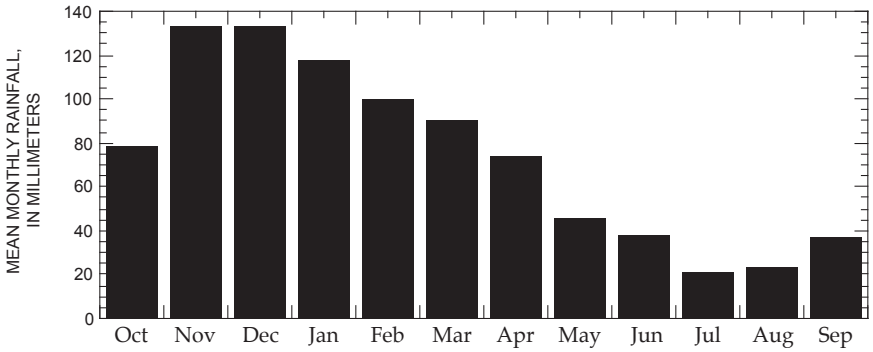

Figure 4. Mean monthly rainfall at a rain gage in study area (R in fig. 1) for the period 1978-1997 (City of Seattle, gage 14, unpub. data).

of October through April. At this rain gage, the mean monthly precipitation for the winter season is 104 mm, the maximum monthly precipitation is 284 mm, and the greatest one-day precipitation is 116 mm. The maximum annual precipitation at this gage was 1,086 mm, and the maximum precipitation for the rainy season (October to April) was 847 mm. All of these values are based on data from 1978 to 1997.

Precipitation and Landslides

Several studies in the Seattle area (Tubbs 1974, 1975; Chleborad 2000, 2003; Shipman, 2001) have analyzed the rainfall events preceding the occurrence of landslides, both shallow and deep-seated. Landslides typically occur during years of above-average precipitation. Years notable for the occurrence of landslides include 1933/34, 1955/56, 1959/60, 1960/61, 1966/67, 1968/69, 1971/72, 1973/74, 1985/86, 1995/96, and 1996/97 (Laprade and others, 2000). For deep-seated landslides, the 1998/99 rainy season also was notable (Shipman, 2001). Tubbs (1974, 1975) investigated the factors that contributed to landslides during the rainy season of 1971–1972. During the months of February, March, and April of 1972, there was approximately 40 percent more precipitation than normal. During this wet period, days of intense rainfall triggered many landslides. Many of the landslides were shallow colluvial landslides, but several deep-seated landslides also occurred. Tubbs (1974, 1975) found that when cumulative rainfall is average or below average, days of intense rainfall do not seem to trigger landsliding.

Chleborad (2000, 2003) analyzed a historical database containing records of 1,300 landslides. Approximately 86 percent of the landslides occurred between December and March. We analyzed this database (Laprade and others, 2000) for only the deep-seated landslides and found a similar pattern—approximately 83 percent of the deep-seated landslides occurred between December and March.

Chleborad (2003) calculated precipitation thresholds for initiation of landslides. Although the majority of the landslides in his study were shallow landslides, thresholds were also calculated for deep-seated landslides. For deep-seated landslides that occurred during the 2001-2002 and 2002-2003 rainy seasons, the 15-day cumulative precipitation before the reporting of the landslides ranged from approximately 67 to 103 mm, with a mean of approximately 84 mm.

Although landslides are typically attributed to short-term rainfall events and thresholds are calculated for these events, single intense rainstorms are most conducive to shallow landsliding. Deep-seated landslides, in contrast, are likely associated with the increase in ground-water levels due to above-average cumulative precipitation, over one or more seasons, rather than short-term rainfall events (Galster and Laprade, 1991; Shipman, 2001).

On the basis of long-term records that begin in 1891, the record four-month precipitation for Seattle occurred in 1998-1999, when the City received approximately 874 mm of precipitation during the period from November to February (National Climatic Data Center web site, http://www.ncdc.noaa.gov/oa/climate/extremes/1999/february/febext1999.html, last accessed March 23, 2007). During this winter season, shallow landslides were infrequent, but several large, deep-seated landslides in the Puget Sound region were active (Shipman, 2001).

Deep-Seated Landslides

Deep-seated landslides in the Puget Sound area are complex in nature. They may involve more than one geologic unit, commonly involve more than one mode of movement, and can be triggered by multiple driving forces, including precipitation, movement of adjacent landslides, or human activities (Tubbs, 1974, 1975). In this section, we describe deep-seated landslides in the Puget Sound area, and define the type and size of landslide we are assessing in our slope-stability analysis.

Varnes' (1958) classification is commonly used to describe landslides. Varnes classifies landslides by the type of material and the type of movement. The deep-seated landslides we are investigating typically move slowly by sliding that includes rotational and translational components. The geologic materials involved are deposits of sand, silt, and clay. Based on Varnes' classification, deep-seated landslides are called earth slumps or the more general category of earth slides. However, earth slides encompass a wide range of depths and volumes, and deep-seated landslides are a subset of this category. To further describe the kind of landslides we are analyzing, we consider criteria used by other authors to distinguish deep-seated landslides. In addition, we use volumes estimated for previous large landslides in Seattle to determine the volume range of potential failures used in our slope-stability analysis.

Figure 5 portrays the characteristics of typical deep-seated landslides along bluffs of the Puget Sound area, as well as the idealized evolution of a typical bluff. This figure shows initial conditions of a bluff with uniform slope. Initial sliding of the materials in the bluff occurs along arcuate slip surfaces, resulting in a rotational component to the movement. Failure surfaces may affect only the uppermost materials or may include the underlying less permeable materials. Rainwater infiltrates to form a perched water table on top of less permeable materials (fig. 5*A*), contributing to the instability of the sand and gravel unit. During or after the initial movement, material from the sand and gravel unit may slide from the upper bluff (fig. 5*B*), and wave erosion may move the material, although human modifications have slowed the action of wave erosion in many areas. Movement of the slide debris from the bench may decrease the buttressing of the upper bluff, leading to additional destabilization (fig. 5*C*). Movement along a deeper surface can also trigger additional movement on the mid-slope bench.

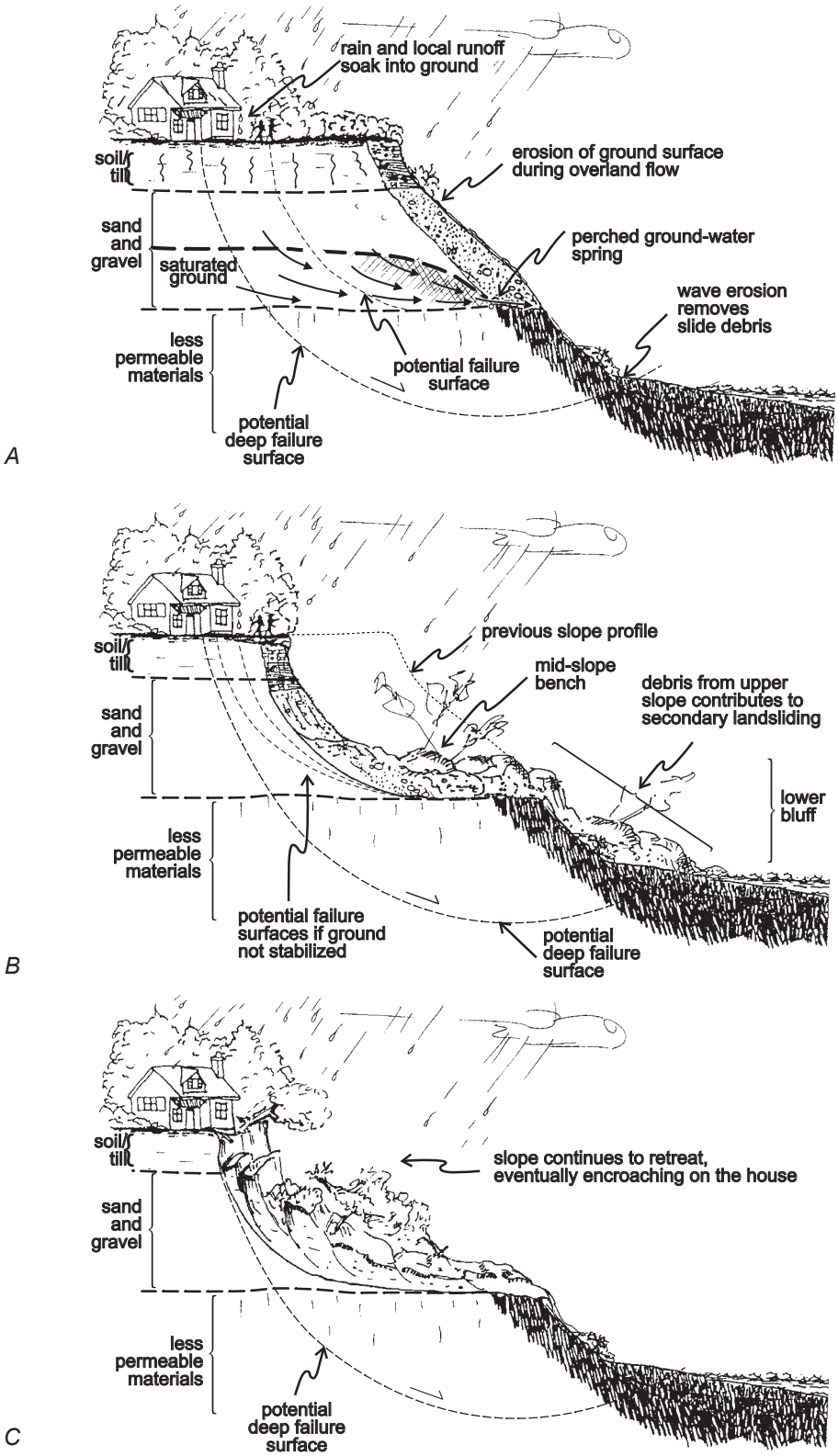

Figure 5. Schematic diagram showing evolution of coastal bluffs in the Seattle area (modified from Gerstel and others, 1997). *(A)* Coastal bluff with a perched water table forming on top of less permeable materials; *(B)* bluff after the initial landslide movement, showing material from the sand and gravel unit slide from the upper bluff; and *(C)* the bluff as the slope continues to retreat. "Potential failure surfaces" and "potential deep failure surface" illustrate potential deep-seated landslides.

Laprade and others (2000) classified landslides in the Puget Sound area into four types, one type consisting of deep-seated landslides. Of the 1,341 historical landslide records they compiled, 265 are classified as "deep seated" and 109 are classified as "deep seated" and "large", defined as having an areal extent greater than 10,000 ft^2 (approximately 900 m^2). For their study, deep seated was defined as movement to a depth greater than about 2 to 3 m.

Volume estimates for deep-seated landslides range from a few hundred to more than one million m^3 (Baum, written commun., 2003). Baum's data-set includes landslides of all sizes and types classified into categories. Some landslides were classified as deep seated, but other categories, such as earth slides, also include landslides that are deep seated. Therefore, to compile a size distribution of deep-seated landslides, we included both (1) landslides classified as deep seated and (2) landslides classified as deep seated, plus those of different classification but having an estimated depth greater than 2 m. Figure 6 shows cumulative probability distributions of landslide volumes for these two groups of data.

Photographs of deep-seated landslides in Seattle are shown in figures 7 to 9. Figures 7 and 8 show a deep-seated landslide on Magnolia Bluff (Perkins Lane), located north of the study area (fig. 1, no. 2) that has an estimated volume of approximately 10,000 to 50,000 m^3 (Baum, oral commun., 2005). The Woodway landslide (fig. 9), located on the coastal bluffs of Woodway, Washington, 25 km north of downtown Seattle, occurred on January 15, 1997 (Savage and others, 2000a), and has an estimated volume of 75,000 to 150,000 m^3 (Baum and others, 1998).

Along Alki Avenue SW, (fig. 1, no. 3) a large deep-seated landslide occurred in the spring of 1974, threatening properties and stripping vegetation from a 150-m-long section of the cliff (Tubbs and Dunne, 1977; Laprade and others, 2000). Other notable deep-seated landslides on the bluffs of Seattle include Bonair Drive (fig. 1, no. 4) (Tubbs and Dunne, 1977), with an approximate volume of 4,000 to 26,000 m^3 (Baum, oral commun., 2005), Discovery Park (fig.1, no. 1) (Tubbs and Dunne, 1977), Duwamish Head (fig.1, no. 5), and California Way SW (fig. 1, no. 6).

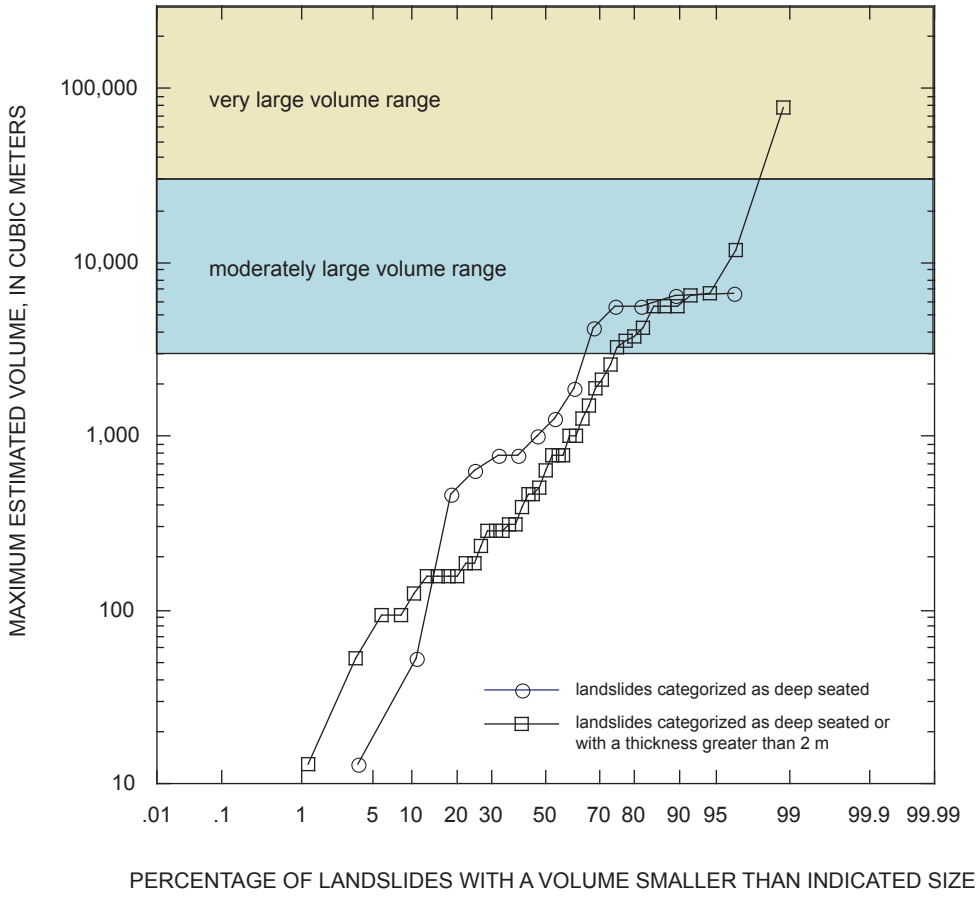

Figure 6. Cumulative probability distributions of landslide volumes in Seattle (data from R. Baum (written commun., 2003)), showing the range of landslide volumes used in our analyses. Circles show landslides categorized as deep seated; squares show these landslides combined with landslides having a thickness greater than 2 m from other categories.

Figure 7. Aerial photograph of large, deep-seated complex landslide on Magnolia Bluff (see fig. 1), after storm during 1996-1997 rainy season. Smaller landslide in slope behind homes is in Vashon till (Qvt). The topographic bench results from a large, deep-seated rotational landslide with a failure surface in advance outwash deposits of the Vashon Drift (Qva) (and possibly the Lawton Clay Member of the Vashon Drift, Qvlc). The failure surface extends below damaged homes and the mid-slope bench they occupy. (Photograph by Leonard Palmer, FEMA, 1997.)

Figure 8. Photograph of large, deep-seated complex landslide on Magnolia Bluff (see fig. 1), looking downslope from above headscarp. The topographic bench results from a large, deep-seated rotational landslide with a failure surface in advance outwash deposits of the Vashon Drift (Qva) (and possibly the Lawton Clay Member of the Vashon Drift, Qvlc). Note that few of the original structures shown in figure 7 remain. (Photograph by D. Brien, USGS, 2000.)

Mapped Deep-Seated Landslides

Maps of deep-seated landslides (fig. 10) provide information about their sizes, shapes, distribution, and appearance. The mapped landslides in our study area provide landslide locations to compare against the results of our slope-stability analysis. Historical and in some cases prehistorical landslides have been mapped by several authors (Youngmann, 1979; Laprade and others, 2000; Wait, 2001; Schulz, 2004; Troost and others, 2005) and by different methods, including from historical records, from field observations, or by interpretation of aerial photographs or high-resolution digital topography. The landslides have been mapped as points representing the center of the headscarp, lines defining the top of a headscarp, or polygons showing the area of the landslide.

Laprade and others (2000) mapped landslide locations as points located approximately at the center of the headscarp. These locations are based on records of historical landslides dating back to 1890 and field observations made during the 1990s. Youngmann (1979) included the boundaries of landslides on slope-stability maps of the Puget Sound area. These slope-stability maps were generated using aerial photographs, geologic mapping, topography, and field observations. Wait (2001) identified deep-seated landslide boundaries using aerial photographs, records of historical landslides, and field observations. Troost and others (2005) delineated landslide headscarps as part of a detailed geologic map that was generated using field mapping of outcrops and excavations, subsurface exploration data, topographic and geomorphic analyses, and pre existing geologic maps. Schulz (2004) mapped landslides from shaded relief images, slope maps, and topographic maps generated from a high-resolution LIDAR (light detection and ranging) DEM.

Each method of mapping has advantages and disadvantages (Schulz, 2004). Landslide locations identified from high-resolution topography (Schulz, 2004; Troost and others, 2005) are useful for identifying large landslide complexes and headscarps that result from a combination of historical and prehistorical landslides, whereas mapping from aerial photography and historical records is more effective for identifying recently active landslides. Topographic models generated from LIDAR have the advantage of being generated from measurements of ground surface elevation beneath vegetation (Haugerud and others, 2003).

On the basis of observations of landslides that occurred during the 1996-1997 rainy season (Baum and others, 1998; Shipman, 2001), much of the deep-seated landslide movement in the Puget Sound area consists of reactivation of preexisting landslide deposits, of the type shown in figure 5*B*, in response to unusually wet conditions or human activities. For example, a deep-seated landslide on Bonair Drive (fig. 1, no. 4) was an ancient landslide deposit that renewed movement when an excavation was made at the toe of the old deposit in 1974 (Tubbs and Dunne, 1977). Another example is the deep-seated landslide on Perkins Lane (fig. 1, no. 2) that was active in March 1996 (Harp and others, 1996); this landslide renewed its movement in January 1997 and again in February 1998 (Baum and others,

Figure 9. Aerial photograph of a deep-seated landslide near Woodway, Washington. (Photograph by E. Harp, USGS, May 1997.)

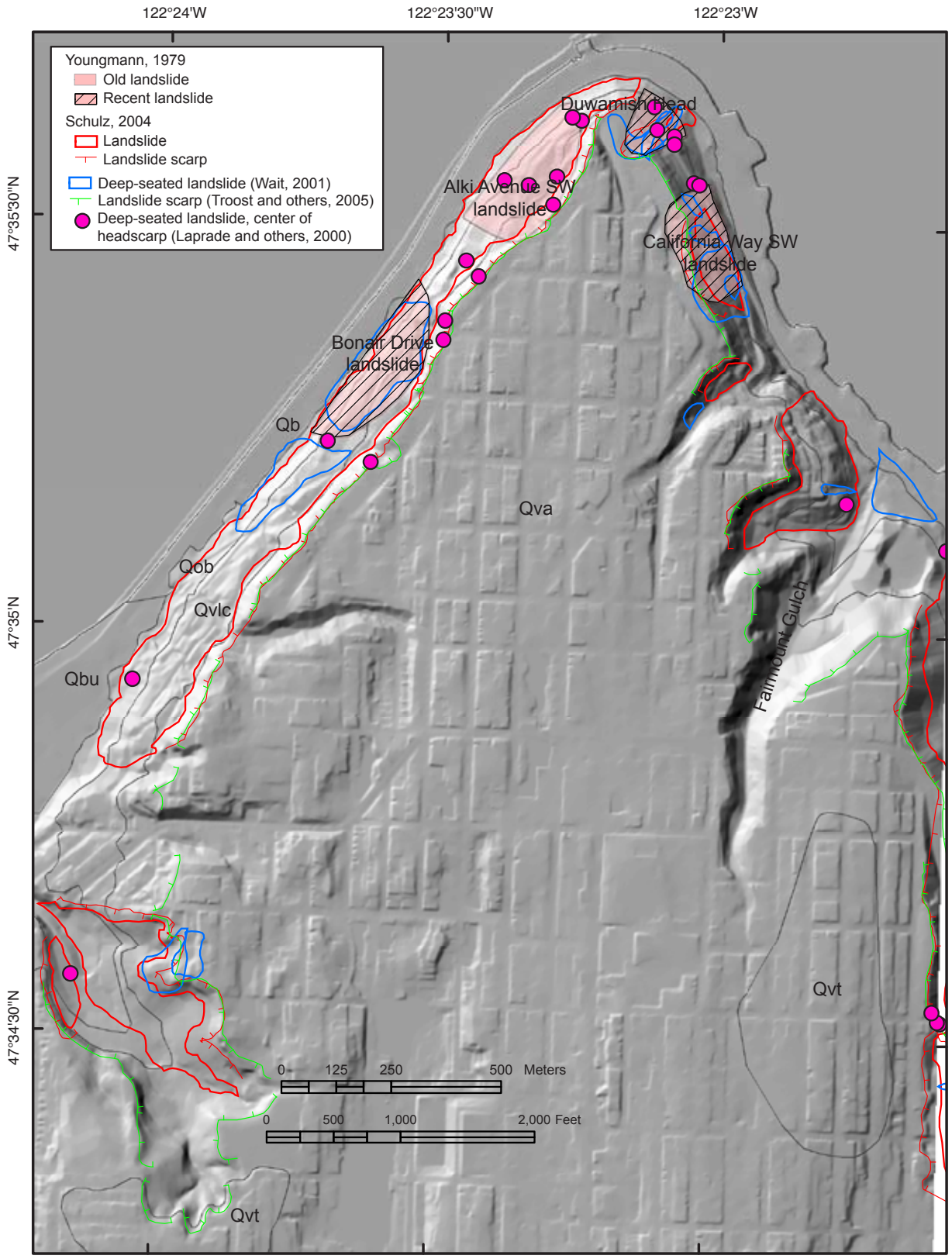

Figure 10. Mapped deep-seated landslides in the study area (Youngmann, 1979; Laprade and others, 2000; Wait, 2001; Schulz, 2004; Troost and others, 2005). Geologic contacts are shown as dark gray lines. See figure 3 for explanation of geologic unit symbols.

1998). Within our study area, one landslide located near Bonair Drive (Tubbs and Dunne, 1977), with an approximate volume of 4,000 to 26,000 m^3 (Baum, oral commun., 2005), has a recorded history of movement dating back to the early 1900s (Shannon & Wilson, Inc., 2000). Shipman (2001) suggests that many of the deep-seated landslides in Seattle originally formed hundreds or thousands or years ago, as glacial ice retreated or in response to large earthquakes. However, not all historical deep-seated landslide activity consists of reactivation of preexisting landslides. The Woodway landslide (Baum and others, 2000; Savage and others, 2000b) is one example where a deep-seated landslide initiated from intact materials.

Geologic Materials in Deep-Seated Landslides

Commonly, large deep-seated landslides in the Seattle area occur in advance outwash deposits or Vashon till, but some landslides may extend into the underlying Lawton Clay Member (Tubbs, 1974; Savage and others, 2000a; Wait, 2001; Baum, oral commun., 2004). Deep-seated landslides may also contain surficial materials, such as colluvium or artificial fill (Laprade and others, 2000; Baum, oral commun., 2004).

The Lawton Clay Member is a low permeability unit conducive to the development of perched water within the overlying material. This perched water table is an important factor affecting slope stability in the Seattle area. Tubbs (1975) found the presence of Lawton or older sediments beneath almost 80 percent of landslides. Tubbs (1975) defined a zone of high landslide hazard near the contact between Qva and Qvlc.
Modeling Methods

The availability of high-resolution digital topography, detailed geologic mapping, and a compilation of subsurface exploration logs allows us to build 3-D models of ground water and slope stability. To analyze the relative stability of coastal bluffs for potential large deep-seated landslides, we combine digital topography, represented by a DEM, with variable strength properties based on the geologic mapping and published strength values for the geologic units. We also include the influence of 3-D pore pressures based on the results of a 3-D ground-water flow model. We calibrate the results of the ground-water model with measured ground-water levels and compare areas of low slope stability in our analysis with mapped landslides.

Landslide Volumes Represented by our Slope-Stability Analysis

In this study, we search for potential failures in the volume range of the largest 25 percent of landslides classified either as deep seated or that have a depth greater than 2 m (fig. 6) based on U.S. Geological Survey (USGS) field observations (Baum, written commun., 2003). We limit our slope-stability analysis to search for potential failures with a volume between 3,000 and 300,000 m^3. Landslides of this magnitude are not the most common type of landslide in the Puget Sound area but are potentially the most destructive. Accurate 3-D modeling of small landslides would require topography of higher resolution than we have available, in addition to a detailed knowledge of local variations in 3-D strengths and pore pressures.

Our slope-stability analysis is appropriate for large landslides with a rotational component, especially those that are characterized by regional material strengths and regional ground-water flow, rather than by local heterogeneities in material strength or hydraulic properties. Our analysis applies to failure of intact bluff materials, rather than to renewed movement in materials that have slid previously. Thus, the analysis applies more to the conditions sketched in figure 5*A*, rather than to movement in preexisting slide debris, which often lies on a topographic bench and may have residual strength properties.

Digital Elevation Model

We combined a 10-ft (~3-m) resolution subaerial DEM with 30-m bathymetric data. The subaerial DEM was generated by the City of Seattle using photogrammetry (City of Seattle, unpub. data), and the bathymetry was obtained from the National Oceanic and Atmospheric Administration (NOAA) (http://estuarinebathymetry.noaa.gov/pacific.html, last accessed March 23, 2007). The bathymetric data was resampled to 10-ft. The combined DEMs (fig. 11) were used to define the ground surface and offshore bathymetry for the ground-water and slope-stability analysis. The region offshore is not affected in most documented bluff failures, but we included the bathymetry to model potential large failures which might extend under Puget Sound.

A higher resolution, 6-ft (~2-m), LIDAR DEM was also available (Terrapoint, 2000-2004). Although LIDAR can better represent the ground surface in areas covered by vegetation (Haugerud and others, 2003), we chose to use the same 10-ft resolution topographic base that was used for the geologic mapping used in this analysis (Troost and others, 2005). We ran our analysis with dry conditions for both DEMs and found that, for large landslides, small local variations in slope revealed by LIDAR do not produce a significant change in the locations of areas with lowest stability (appendix A).

Geologic Layers

The 3-D ground-water and slope-stability analysis include layers that represent the geologic units. We distinguish these layers in order to assign appropriate hydrogeologic and geotechnical properties for our analysis.

A geologic map (fig. 3) (Troost and others, 2005) provides the location of geologic contacts where they intersect the

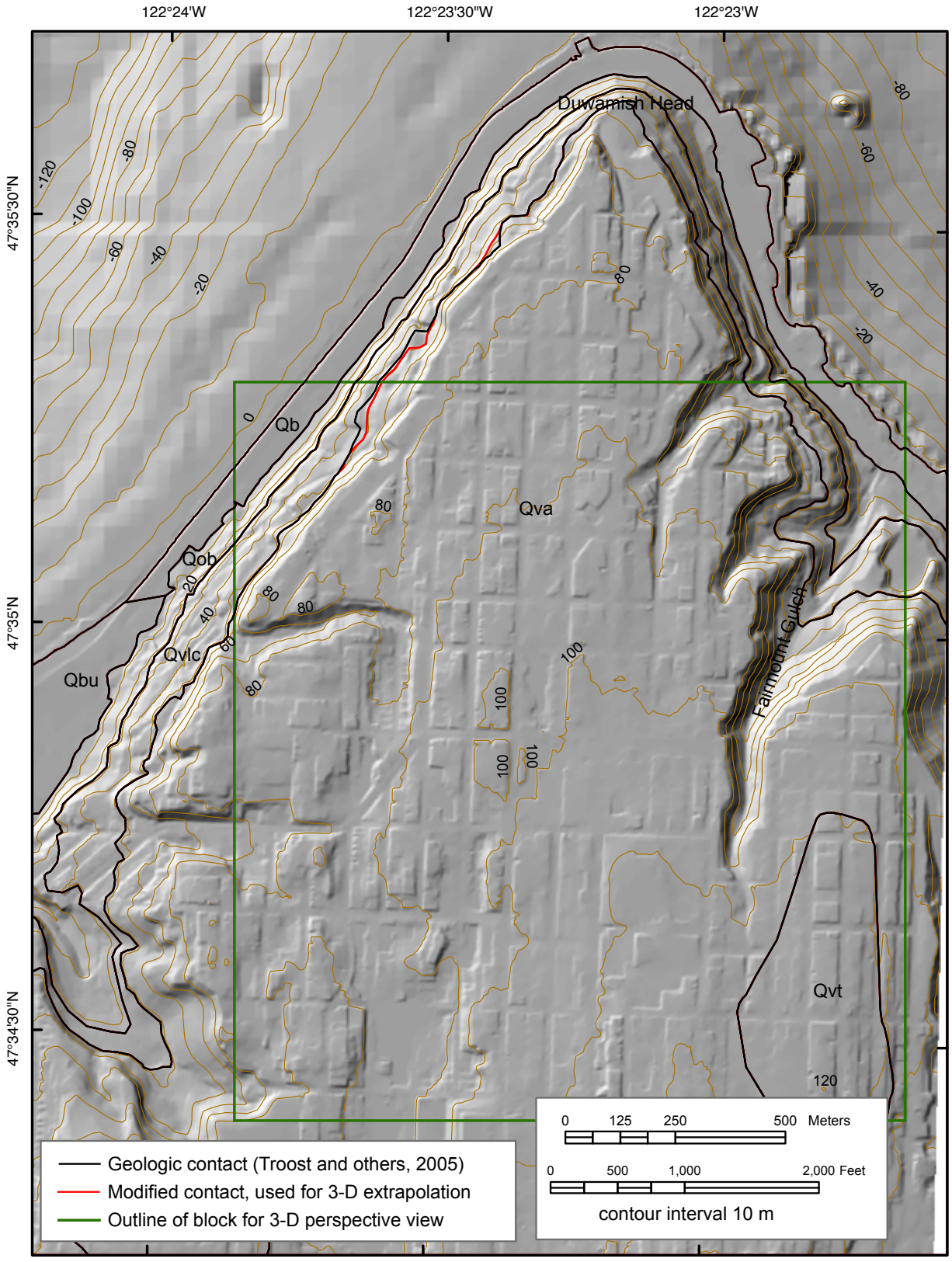

Figure 11. Shaded relief image showing topographic contours derived from digital elevation model (City of Seattle, unpub. data) combined with Puget Sound bathymetry (http://estuarinebathymetry.noaa.gov/pacific.htm, last accessed March 23, 2007). Also shown are original and modified geologic contacts and an outline showing the location of block diagram shown in figure 12. See figure 3 for explanation of geologic unit symbols.

ground surface. To create a 3-D geologic model, we needed to know the elevation of each geologic contact in the subsurface. We used the mapped geologic contacts to create these surfaces. We did not include information from boreholes, as this information was already used by the geologists in identifying the location of the surface contacts.

By combining mapped geologic contacts (Troost and others, 2005) with a DEM (City of Seattle, unpub. data), we determined the elevations of the geologic contacts at the land surface. We used the ESRI™ (Environmental Systems Research Institute) software, ArcGIS™ ArcInfo Workstation 8.x, to interpolate elevations of the bottom of each geologic unit, using an inverse-distance-weighted method. This method honors the mapped contacts and creates a smooth surface in the subsurface, where contact elevations are not available. Details of our method for defining the geologic contacts in the subsurface are provided in appendix B.

We created four layers corresponding to the mapped geologic units (fig. 12). The uppermost layer corresponds to advance outwash deposits (Qva) and Vashon till (Qvt). Although Qva and Qvt have different hydrologic and strength properties, Qvt is present only where it caps a small area of flat-lying ground in the southeast corner of the study area (fig. 3). Within the study area, this small volume of Qvt is insignificant to bluff instability, and we combine it with Qva to simplify the model. Beneath Qva is the Lawton Clay Member (Qvlc). The bottom layer in the 3-D geologic model consists of Olympia beds (Qob) and older deposits. These three layers—(1) Qva combined with Qvt, (2) Qvlc, and (3) Qob and older deposits—form the bluffs. The fourth layer is present along the shoreline of the Puget Sound, where we model thin beach deposits (Qb and Qbu).

Elevations of the bottom of the uppermost two layers were calculated using the inverse-distance-weighted method (appendix B). The bottom elevation of the beach deposits (Qb) was assigned based on this unit's typical thickness of 3 to 5 m in the study area (Troost, written commun.). This unit has relatively low strength properties, so, for a conservative estimate of slope stability, we assigned a uniform thickness of 4.5 m, just slightly less than the upper limit of typical thickness. The layer containing Qob and older deposits constitutes all material below Qvlc or Qb.

Figure 13 shows the modeled elevations of the bottom of Qva and Qvlc layers (figs. 13*A* and *B*) and isopach maps showing modeled thicknesses of these deposits (figs. 13*C* and *D*). The modeled thickness of Qva is 0 to 85 m, with a mean thickness of 45 m. The modeled thickness of Qvlc is 0 to 34 m, with a mean thickness of 19 m. These variations in thickness result almost entirely from differences in elevation of the ground surface.

Although the surfaces defining the geologic contacts are approximately horizontal, they are not perfectly flat, as evidenced by the fact that the geologic contacts do not exactly follow elevation contours around the bluff. The modeled sur-

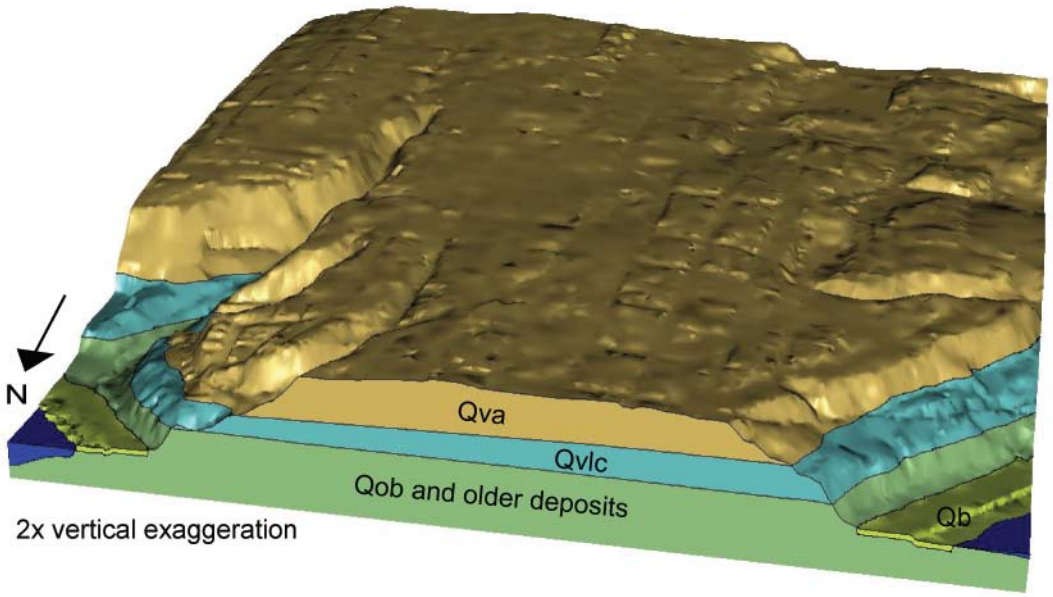

Figure 12. Perspective view of our 3-D model of geologic units in the study area, looking south-southeast; figure 11 shows outline of area. The geologic layers shown are based on our 3-D interpretation of the geologic map by Troost and others (2005); note that Vashon till (Qvt) is combined with advance outwash deposits (Qva) in our modeled layers. Topography is from the City of Seattle digital elevation model (unpub. data) combined with bathymetry (http://sposerver.nos.noaa.gov/bathy/pacific.htm). See figure 3 for explanation of geologic unit symbols.

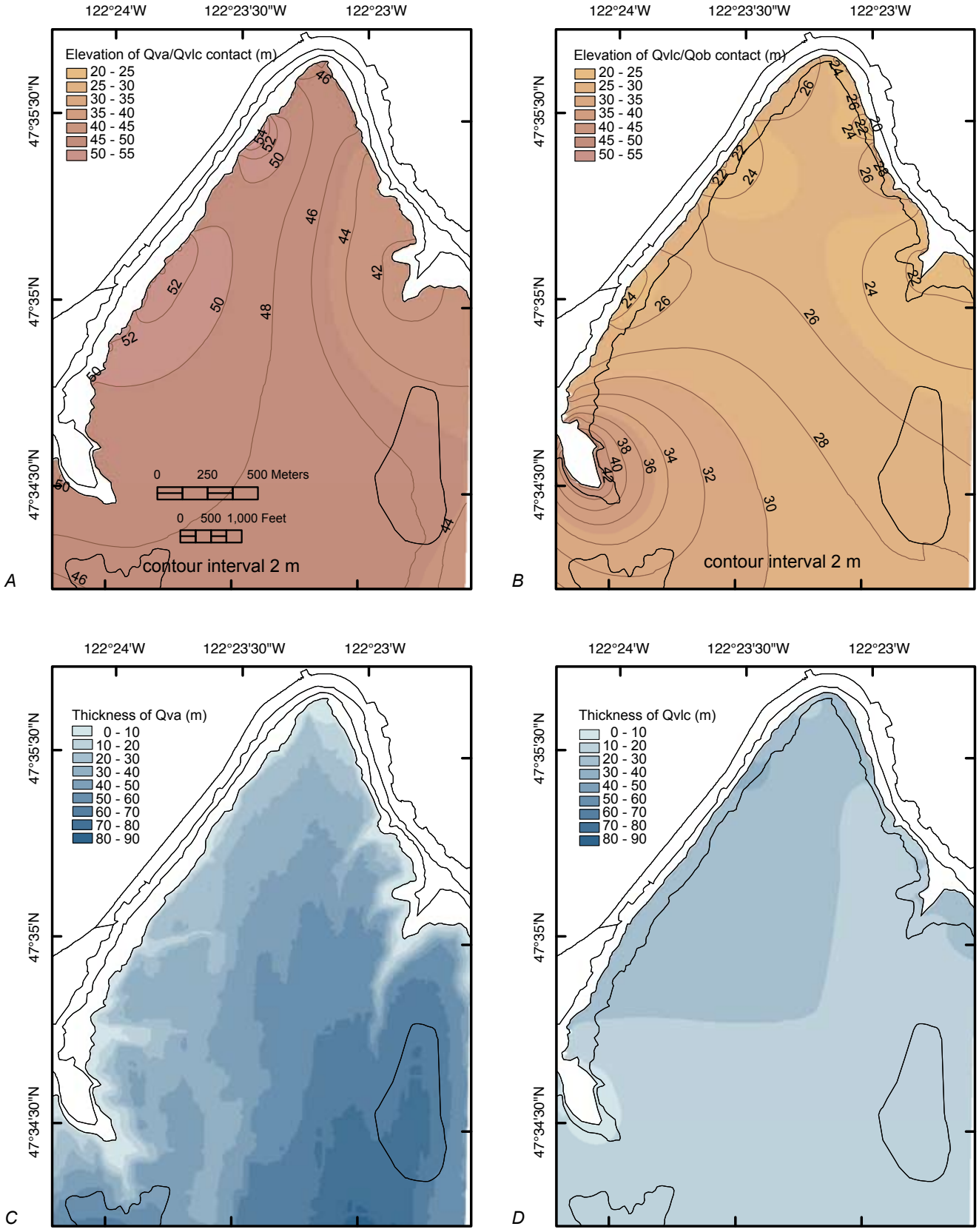

Figure 13. Maps showing elevation of modeled subsurface geologic contacts beneath study area and thickness of geologic units: *(A)* elevation of bottom of Qva, *(B)* elevation of bottom of Qvlc, *(C)* thickness of Qva, and *(D)* thickness of Qvlc. Geologic contacts are shown as black lines. See figure 3 for explanation of geologic unit symbols.

faces reflect these local variations in the elevation of the geologic contacts as mapped at the ground surface. In this regard, areas where the surfaces slope steeply tended to cause problems for our ground-water model. Model cells in these areas would often dry out and several early versions of our model failed to converge. For this reason, we compromised between (1) honoring the geologic contact exactly as mapped and (2) reducing abrupt elevation changes in the surfaces representing the geologic contacts. Abrupt changes can be identified where a geologic contact crosses several topographic contour lines over a short distance (fig. 11). Within the Bonair Drive landslide (see location on fig. 10), the unmodified Qva-Qvlc geologic contact reflects landslide displacement and is correct on the ground surface. However, our purposes require the location of the contact in undisturbed ground of the subsurface, and to more accurately reflect the location in the subsurface, we made a minor modification to the Qva-Qvlc contact (fig. 11) before interpolating our subsurface contact. At one other location, north of the Bonair Drive landslide, the elevation of the mapped geologic contact changes abruptly and we adjusted it slightly.

The contour maps of the interpolated geologic contacts (figs. 13*A* and *B*) reflect local undulations in the modeled geologic contacts. Local highs and lows in the modeled surfaces are most pronounced near the bluff face, where the surfaces closely follow the mapped contacts.

3-D Ground-Water Flow Model

Numerical Model

We simulated ground-water flow in the study area using MODFLOW-2000, a modular three-dimensional finite-difference ground-water flow model (McDonald and Harbaugh, 1988; Harbaugh and others, 2000). This model uses a block-centered finite-difference solution to the 3-D, transient ground-water flow equation:

$$\frac{\partial}{\partial x}(K_{xx}\frac{\partial h}{\partial x})+\frac{\partial}{\partial y}(K_{yy}\frac{\partial h}{\partial y})+\frac{\partial}{\partial z}(K_{zz}\frac{\partial h}{\partial z})-W=S_s\frac{\partial h}{\partial t} \qquad (1)$$

where:

K_{xx}, K_{yy}, and K_{zz} are values of hydraulic conductivity along the x, y, and z coordinate axes;

h is the hydraulic head;

W is a volumetric flux per unit volume and represents sources and/or sinks of water;

S_s is the specific storage of the porous material; and

t is time.

We used a series of steady-state simulations to describe the general pattern of ground-water flow and examine how ground-water flow in a 3-D topography influences slope stability. In steady state, the right hand term in equation 1 equals 0. Our simulation includes two contributions to W in equation 1—recharge, R, is a source, and flow out of drain cells, which we use to simulate seepage from the face of the bluff, is a sink. Our slope-stability analysis is designed for steady-state scenarios. Therefore, we did not conduct more complicated transient simulations of the ground-water model, which would be more difficult to calibrate and require knowledge of storage parameters that are not well known.

Input for the ground-water model includes the horizontal dimensions of the finite-difference grid and elevations for the top of the model (the ground surface). Each layer in the model is defined by a bottom elevation, a boundary array, values for initial head, the layer type (convertible or confined), and vertical and horizontal hydraulic conductivity. Other model inputs are rainfall recharge, location of drain cells, and drain conductance.

Model Domain

The model domain is discretized into a finite-difference grid with dimensions of 912 rows and 682 columns (fig. 14). The horizontal dimensions of all grid cells are approximately 3 m (10 ft) by 3 m. This cell size is equal to the DEM resolution and is also the resolution used in the 3-D slope-stability analysis. The number of active cells within the grid is 267,401. Active cells consist of cells north of the southern no-flow boundary (described below under 'boundary conditions') that have a land-surface elevation above the water level of Puget Sound.

Although generalized regional ground-water flow could be described with a grid of lower resolution than the DEM, the slope-stability analysis requires pore-pressure values at each DEM node. MODFLOW-2000 calculates a hydraulic head at the center of each cell for each layer. By using the same resolution for both the ground-water and slope-stability analysis, we used the same input grids for both models. Thus, we used the output results from the ground-water model to directly calculate a detailed description of the 3-D pore pressures for the slope-stability analysis. A ground-water model with a grid of coarser resolution might provide the advantage of converging to a solution more quickly, but the output would then need to be resampled to the resolution of the slope-stability analysis.

Boundary Conditions

The horizontal boundaries of the model domain (fig. 14) are defined by the extent of subaerial topography on the north, east, and west sides. The southern extent of the model is a no-flow boundary that corresponds to the approximate location of an inferred ground-water divide. We estimated the location of this southern ground-water boundary by identifying

the surface-water divide as computed in the ESRI™ software, ArcGIS™ ArcInfo Workstation, using the FLOWDIRECTION and BASIN commands. This southern boundary is a no-flow boundary, whereas the other horizontal boundaries, on the north, east, and west limits of the model, are defined by approximately 3 rows (9 m) of constant-head cells. These cells are assigned a constant head equal to the elevation of Puget Sound.

Another boundary condition exists in cells located on the bluff in Qva or Qvlc. These cells represent parts of the topography where ground-water seepage can occur and are modeled as drain cells in MODFLOW.

The top of basement rock in the study area lies between 90 m and 450 m below sea level (Jones, 1999). A no-flow boundary defining the bottom of the model at the top of basement rock is set at a constant elevation of 150 m below sea level.

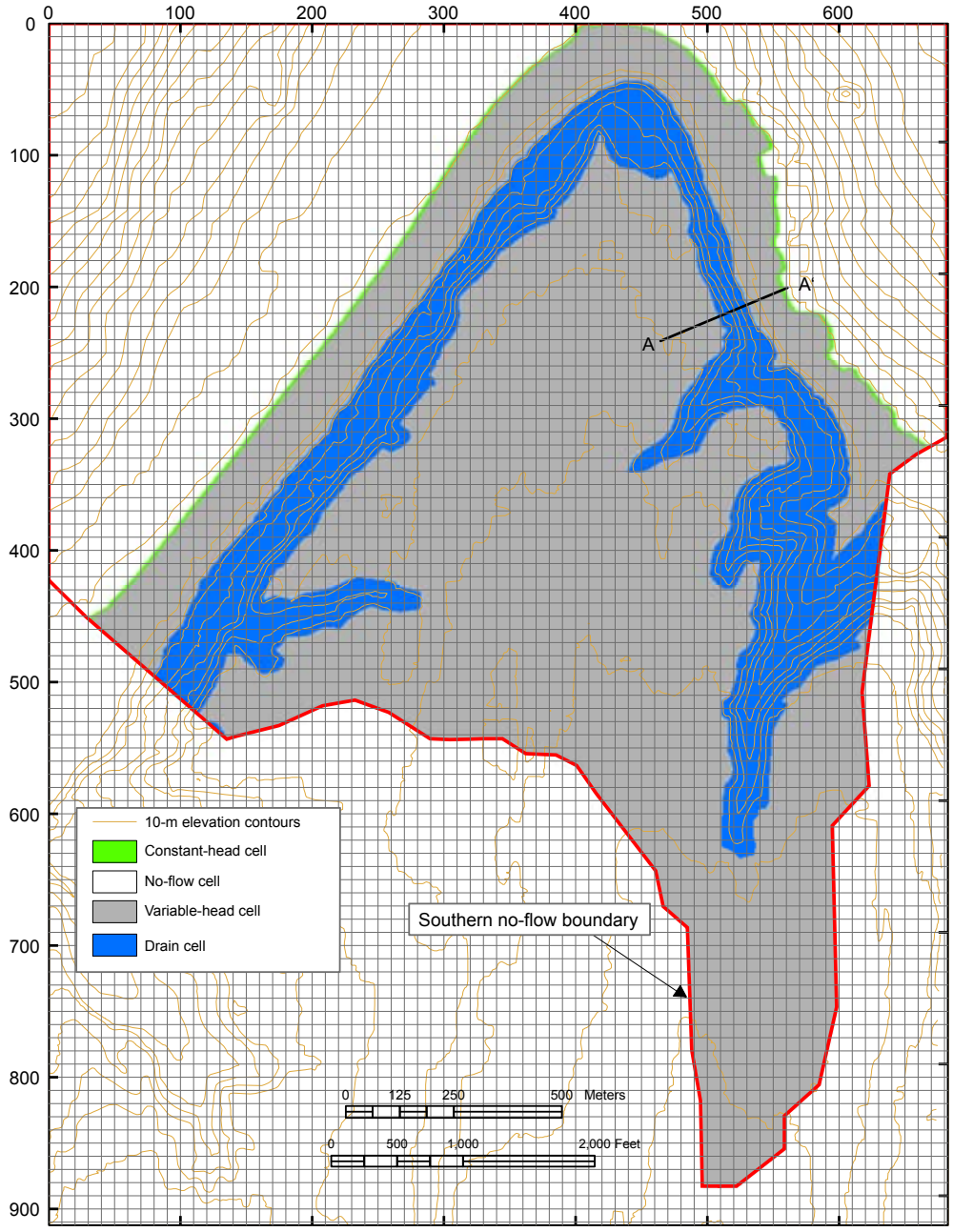

Figure 14. Map showing horizontal boundary conditions for ground-water flow model, southern no-flow boundary, and topographic and bathymetric contours (brown lines). Each grid cell shown in the figure contains 100 (10x10) model cells. Axes labels refer to cell number. A–A' is the location of the cross section shown in figure 17.

Hydrogeologic Layers

We divided the model domain into four layers based on hydraulic properties of geologic materials. The hydrogeologic layers for the ground-water model are similar to the geologic layers shown in figure l2, with two exceptions—(1) beach deposits (Qb and Qbu), which have limited volume in the study area, are combined with Qob and older deposits and (2) the Lawton Clay Member (Qvlc) is divided into two layers. The four layers in the ground-water model are (1) advance outwash deposits (Qva) plus a small volume of Vashon till (Qvt), (2) upper portion of Qvlc, (3) a thin layer at the bottom of Qvlc, and (4) all other materials (Qob and older deposits, plus the small volume of Qb and Qbu).

Assuming predominantly horizontal flow in aquifers and vertical flow in confining units, the results of the ground-water model using four layers are sufficient to describe the 3-D pore pressure distribution for our slope-stability analysis. The basis of these assumptions is (1) in aquifers with hydraulic conductivities much higher than the conductivities in the confining beds, flow is typically horizontal (Freeze and Cherry, 1979); and (2) ground-water models for Puget Sound assume this pattern (Vaccaro 1992; Vaccaro and others, 1998).

The uppermost layer (layer 1) is the upper aquifer corresponding to Qva and Qvt. Beneath the upper aquifer is a confining unit, the Lawton Clay Member (Qvlc). For confining layers with predominantly vertical flow, at least two head values in the unit are required to describe the 3-D pore-pressure distribution. We consequently subdivided Qvlc into two layers, layers 2 and 3, having the same hydraulic parameters, allowing us to compute a vertical hydraulic gradient. The computed vertical hydraulic gradient was used subsequently to describe 3-D pore pressures for the 3-D slope-stability analysis.

We divided the Lawton Clay Member such that layer 2 encompasses most of its thickness, and layer 3 is a thin layer (typically less than 0.3 m) at the base of the unit. Layer 2 was assigned a bottom elevation just above the bottom of the Lawton. To avoid cells of negligible thickness in layer 3, which have a tendency to dry out and create problems with convergence to a solution, we defined the elevation of the bottom of layer 2 slightly differently where the thickness of the Lawton is extremely small (less than 1 ft or approximately 0.3 m). The bottom of layer 2 was calculated as:

$$z_2 = z_3 + (z_1 - z_3)\ 0.01, \text{ if } z_1 - z_3 > 0.3 \text{ m, or} \quad (2)$$

$$z_2 = z_3 + (z_1 - z_3) / 2, \text{ if } z_1 - z_3 < 0.3 \text{ m} \quad (3)$$

where z_n is the elevation of the bottom of layer 1, 2, or 3.

The bottom layer in the model, layer 4, is an aquifer consisting of Olympia beds (Qob), undifferentiated deposits older than the Olympia beds, and beach deposits (Qb and Qbu). The beach deposits differ in conductivity from the other units in this layer, but we combined the units because the beach deposits are present in only a small portion of the study area and are thin (approximately 3 to 5 m in thickness). We initially chose a constant value of -150 m for the bottom elevation of layer 4. Sensitivity of computed hydraulic heads to this boundary condition was examined in our sensitivity analyses.

Layer Types

MODFLOW-2000 allows layers to be defined as a confining unit, confined aquifer, or convertible aquifer. A convertible aquifer is an aquifer that can be either confined or unconfined, where unconfined aquifers have variable saturated thickness and a hydraulic head below the elevation of the top of the layer. The advance outwash deposits (layer 1) and the Olympia beds (layer 4) were modeled as convertible aquifers. The Lawton (layers 2 and 3) could be defined as a confining unit rather than an aquifer, but MODFLOW-2000 does not provide calculations of head in units defined as confining units. Because our slope-stability calculations require estimates of pore pressure at any elevation, we modeled the Lawton as an aquifer rather than a confining unit. Because the Lawton is confined from above by layer 1 and its saturated thickness likely does not vary as head varies, we defined the Lawton as a confined (rather than convertible) aquifer.

Initial Heads

To obtain a steady-state solution with MODFLOW-2000, estimates of initial head are needed. When we attempted to use a constant value for initial head in each layer, numerous cells would dry out and the solution would not converge. However, the resulting heads showed a flow pattern similar to what we would expect. We used the MODFLOW-2000 wetting option to convert dry cells to variable head cells, but this did not solve the convergence problems.

To resolve difficulties with model convergence, we used the ESRI™ software, ArcGIS™ ArcInfo Workstation, to import heads from one simulation that did not converge, replaced the dry cells with an average head value from surrounding cells, created a new array of initial heads, and ran the model with this new array. We repeated these steps if necessary. Following this iterative process, we succeeded in obtaining model convergence. Once we found initial heads that produced a successful simulation, we were able to use these initial heads and vary other model parameters. If we modified the model parameters in such a way as to cause a significant change in head distribution, we needed to repeat the process of finding initial heads.

Hydraulic Conductivities

Deposits in the study area have a wide range of published values for hydraulic conductivity. Previous studies provide summaries of conductivities (Vaccaro, 1992; Woodward and others, 1995; Vaccaro and others, 1998; Savage and others,

2000b). Table 1 summarizes some of the published values for hydraulic conductivity, as well as layer descriptions and conductivities used in our simulations. Initially, we used median conductivities from these earlier studies. We then adjusted these values to obtain simulated hydraulic heads in reasonable agreement with the measured ground-water levels. Our adjusted values are within the range of published values.

Information on the ratio of horizontal to vertical hydraulic conductivity is limited. Some studies estimate an anisotropy ratio of approximately 10 in the coarse-grained aquifers, such as Qva (Morgan and Jones, 1996). Our initial-case simulation used isotropic conductivities, and we examined the effect of anisotropic conductivity in the upper aquifer in our sensitivity analyses.

Recharge

We used three steady-state recharge scenarios to examine plausible ground-water conditions— (1) recharge estimated from average annual precipitation was used to compare the model results with measured ground-water levels, (2) recharge estimated from the average monthly precipitation during the rainy season was used to simulate the conditions during an average rainy season, and (3) recharge estimated from the maximum recorded 4-month precipitation was used to simulate conditions during an extremely wet year. In all three scenarios, the recharge estimate was applied as a steady-state rate, even if it was derived from rainy-season precipitation. Recharge for the three scenarios was calculated using a regression equation developed by Vaccarro and others (1998).

Our estimate of average annual recharge (scenario 1), used for our model calibration, is based on average annual precipitation at a City of Seattle rain gage located within the study area (unpub. data, 1978-1997). The average annual precipitation, based on 19 years of records, is 873 mm at this gage. To estimate recharge, we used this value, combined with the following regression equation developed for outwash-covered areas in the Puget Sound region (Vaccaro and others, 1998):

$$R = 0.838\ P - 248 \quad (4)$$

where:
R is mean annual recharge in millimeters, and
P is mean annual precipitation in millimeters.

Using equation 4 with average annual precipitation, we obtained an estimated recharge of approximately 480 mm. This amount (as well as for subsequent recharge scenarios) was converted to a rate with the same units as hydraulic conductivity for our steady-state analysis.

Average recharge for the rainy season (scenario 2) was calculated using the mean monthly precipitation of 104 mm for October through April (City of Seattle, unpub. data, 1978-1997). Although this precipitation rate does not occur throughout the year, to estimate recharge equivalent to steady-state, we applied the rainy-season precipitation to a full year and obtained an estimate of annual recharge of approximately 800 mm from equation 4.

For slope-stability analysis, we are interested in conditions during the rainy season when pore pressures are elevated and landslides are likely to occur. As an upper limit on recharge, or a "worst case" extremely wet scenario (scenario 3), we used the maximum 4-month precipitation of record, which is from 1999 (National Climatic Data Center (NCDC) web site (http://www.ncdc.noaa.gov/oa/climate/extremes/1999/february/febext1999.html, last accessed March 23, 2007). We applied this maximum four-month precipitation of 874 mm to equation 4 and obtained an annual recharge estimate of 1,950 mm.

Simulation of Seepage Faces

To simulate the effect of ground-water seepage from the bluff, we used the MODFLOW-2000 drain package. This package is designed to simulate the effect of features similar to an agricultural drain (McDonald and Harbaugh, 1988) and is commonly used to simulate seepage faces in regional ground-water flow models (Sapik and others, 1988; Anderson and Woessner, 1992; Morgan and Jones, 1996; Fabritz and others, 1998; Vaccaro and others, 1998). Drain cells have the effect of removing water from the aquifer at a rate proportional to the difference between the head in the aquifer and the elevation of the drain. If the head in the aquifer falls to an elevation below the elevation of the drain, the drain cell has no effect. For each drain cell in the model, discharge flowing out of the drain is computed as (McDonald and Harbaugh, 1988):

$$Q_{dr} = C_{dr}\,(h - d) \text{ for } h > d, \quad (5)$$

$$Q_{dr} = 0 \quad \text{for } h <= d, \quad (6)$$

where:
Q_{dr} is discharge out of the drain,
C_{dr} is drain conductance,
h is total hydraulic head, and
d is drain elevation.

In our model, cells located on the bluff in layer 1, 2, or 3 (Qva and Qvlc) are drain cells (fig. 14).

We calculated the drain elevation for each cell as a function of the DEM elevation at the cell and slope computed from the eight adjoining cells. Figure 15 shows a simplified 3-D representation of the drain elevation and area exposed to the bluff. Drain elevation, d, was calculated as:

$$d = z - \tan(\text{slope})\, dx, \quad (7)$$

where:
z is ground surface elevation of the cell;
slope is slope of DEM, calculated with GRID SLOPE command; and
dx is grid spacing.

Table 1. Summary of hydrogeologic-layer descriptions, ranges of published values for hydraulic conductivity (K), and values of hydraulic conductivity used for the ground-water modeling.

Description of hydrogeologic layers				Ranges of published *K* values			*K* values used for groundwater modeling	
Model layer	Predominant geologic unit	Unit type	Hydrogeologic unit*,†	Minimum *K* (m/s)	Maximum *K* (m/s)	Median *K* (m/s)	*K* values for sensitivity analyses (m/s)	*K* calibrated to measured water levels (m/s)
1	Advance outwash deposits (Qva)	convertible aquifer	Fraser Aquifer	$4x10^{-7}$*	$2x10^{-2}$*	$1x10^{-4}$* $3x10^{-4}$§	$2.5x10^{-5}$ - $1.0x10^{-4}$	$2.5x10^{-5}$
2 and 3	Lawton Clay Member (Qvlc)	confined aquifer	confining unit	$3x10^{-10}$*	$1x10^{-8}$*	$5x10^{-9}$*	$2.5x10^{-9}$ - $1.0x10^{-8}$	$2.5x10^{-9}$
4	Olympia beds (Qob)	convertible aquifer	Puget Aquifer	$2x10^{-6}$†	$2x10^{-2}$†	No data	$1.5x10^{-6}$ - $1.5x10^{-4}$	$1.5x10^{-5}$

* Vaccarro and others, 1998.
† Vaccarro and others, 1992.
§ Woodward and others, 1995.

The generalized equation for conductance, *C*, is (Harbaugh and others, 2000):

$$C = \frac{KA}{L} \quad (8)$$

where:
C is conductance;
K is hydraulic conductivity;
A is cross-sectional area perpendicular to the flow; and
L is length parallel to the flow path.

For 3-D flow, the value of drain conductance, C_{dr}, depends on the characteristics of the convergent flow pattern toward the drain, as well as the characteristics of the drain, and there is no general formulation for calculating C_{dr} (McDonald and Harbaugh, 1988). Using the definition of drain conductance (equation 8) as a function of both hydraulic conductivity and the area of the cell exposed to the bluff, we used an approach similar to that of Morgan and Jones (1996) to calculate an initial value for conductance. We then adjusted C_{dr} in our calibration.

Morgan and Jones (1996) estimated the area used in the calculation of drain conductance by assuming that the seepage face spans the entire width of the cell and that the height of the seepage face is half the thickness of the cell. They used a flow-path length equal to the distance from the cell center to the seepage face. We changed this formulation slightly by estimating the area as the height of the cell exposed to the bluff (fig. 15) times the width of the cell. Our initial estimate of drain conductance was calculated as:

$$C_{dr} = \frac{KA}{L} = \frac{Kbw}{L} \quad (9)$$

where:
K is hydraulic conductivity,
b is height of the cell exposed to the bluff,
w is width of the cell, and
L is length of flow path.

In our case, *w* equals 10 ft (about 3m), and *L* equals the distance from the center to the edge of the cell or 5 ft (about 1.5m). Equation 9 simplifies to:

$$C_{dr} = 2\,K\,b \quad (10)$$

We estimated height of the cell exposed to the bluff as the DEM elevation minus the drain elevation:

$$b = z - d \quad (11)$$

Figure 16 shows the height of each drain cell in the model domain. The drain conductance of cells is lower where the slope is gentle and therefore a small portion of the cell is exposed to the bluff. Note that, although the entire bluff face contains drain cells, only cells where hydraulic head is greater than drain elevation will drain water (equations 5 and 6).

Sensitivity and Calibration of Ground-Water Flow Model

We tested the sensitivity of simulated total hydraulic heads to changes in recharge, drain conductance, elevation of the bottom of the model, hydraulic conductivity in each layer, and anisotropic conductivity in layer 1. Although changing the values of each of these parameters affects the calculated heads

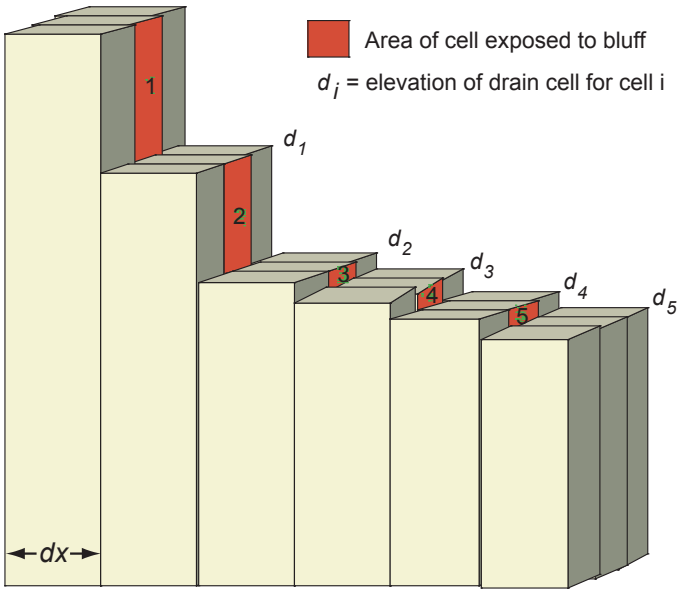

Figure 15. Schematic representation of drain elevation (d) and area of cell exposed to bluff. In this simplified example, only the middle cell (from front to back) shows the area exposed to the bluff and $d_1 = z_2$, $d_2 = z_3$, …., where d is the drain elevation and z is ground surface elevation of the given cell. Cell size is dx. The figure is not to scale.

in all layers, some of the parameter modifications caused negligible changes to hydraulic head in layer 1 (Qva). The most significant changes to hydraulic head in layer 1 were caused by changes in drain conductance, hydraulic conductivity in layer 1 or layer 2, and recharge. The goal of calibration is to adjust the steady-state model to match observations of average hydraulic head conditions in Qva. With the calibrated model, we then tested sensitivity to increased recharge.

Initially, we used average annual recharge, and adjusted the hydraulic conductivities (based on median values) and drain conductance (based on equation 10) until we obtained a model that would converge to a solution. Starting from these initial parameters, we then calibrated the model by varying the model parameters in three independent steps—(1) drain conductance, (2) hydraulic conductivities, and (3) increased recharge. We compared the results for steps 1 and 2 to the available measured ground-water levels in the study area to determine the best-fit parameters. We then used this best-fit model to examine the effects of increased recharge in step 3.

Numerical Model

Adjustment of Initial Parameters

We started adjusting initial parameters by using our estimate of average annual recharge, median hydraulic conductivities (for units where this value was available), and our initial estimate of drain conductance. No median value for conductivity was available for the units in layer 4, but this layer typically has a hydraulic conductivity less than $4x10^{-5}$ m/s (Jones, 1999). We assigned a conductivity to layer 4 equal to half the conductivity of layer 1. These parameters (median conductivities and our initial estimate for drain conductance) resulted in numerous dry cells and a ground-water model that would not converge to a solution. To obtain a numerical solution, we lowered hydraulic conductivity for layer 1 and lowered drain conductance in layers 1, 2, and 3. We found that the model converged to a solution when we lowered our initial estimate of drain conductance by two orders of magnitude and used a layer-1 conductivity equal to half of the median value. Starting with these adjusted initial parameters, we then calibrated the model against measured ground-water levels.

Comparison with Measured Ground-Water Levels

Model parameters were adjusted to calibrate water levels in layer 1 against water-level observations from 33 borehole logs (Schulz, written commun., 2003). These 33 borehole logs were drilled in Qva. We excluded water levels measured in colluvium or other units, as well as anomalously high water levels in Qva that appeared to be from locally perched layers. Twenty-four of the boreholes were not deep enough to reach the water table, and therefore provide only an upper limit for water level.

Each well had only one recorded measurement; and most measurements were made in different years and seasons. We did not find a significant difference between water level measurements in the rainy and dry seasons, and therefore we combined the data to represent overall average conditions. The lack of a distinction in seasonal water levels may result from measurement during different years or may result from a small sample size that made it difficult to distinguish differences resulting from spatial versus temporal patterns. Although none of the wells in the study area had long-term records of water levels, observations from wells in other parts of Seattle show that seasonal water-level fluctuations in the uppermost aquifer range from less than 1 m to 3.5 m (Vaccaro, 1992; Woodward and others, 1995).

To assess the fit of the modeled ground-water levels to measured ground-water levels in layer 1, we used the root-mean-square error for cells with water level measurements:

$$RMSE = \sqrt{\frac{1}{n}\sum_{1}^{n}\left(h_s - h_0\right)^2} \qquad (12)$$

where:
RMSE is root-mean-square error;
n is number of measured water levels;
h_o is observed water level; and
h_s is simulated hydraulic head.

To distinguish the influence of parameters independently, conductivity and drain conductance were varied separately using the parameters outlined in table 2. Although we changed the drain conductance in layers 1, 2, and 3 at the same time, the flow from drains in layers 2 and 3 is negligible and the model was most sensitive to changes in layer 1.

Effects of Drain Conductance

Drain conductance, C_{dr}, for a cell cannot be readily measured, and therefore drain conductance is one of the parameters with the most uncertainty. We examined the effects of drain conductance ranging over several orders of magnitude. Changes in drain conductance affected both the level of the water table and the shape of the water table (fig. 17*A*), with the most significant changes in layer 1.

We found that increasing the drain conductance from its initial value lowered the water table in layer 1 and resulted in a more steeply sloping water table near the bluff (fig. 17*A*, version 2). The calculated heads were lower than most of the measured ground-water levels.

Decreasing the drain conductance by one half from its initial value raised the water table slightly (fig. 17*A*, version 3). To significantly raise the elevation of the water table required decreasing the drain conductance by an order of magnitude (fig. 17*A*, version 4). In addition to raising the water table, this drain conductance resulted in a more gently sloping water table where the difference in water-table slope was greatest near the bluffs. The lowest *RMSE* for these cases occurred with a drain conductance equal to 0.01 $K\,b$ (table 2, version 3).

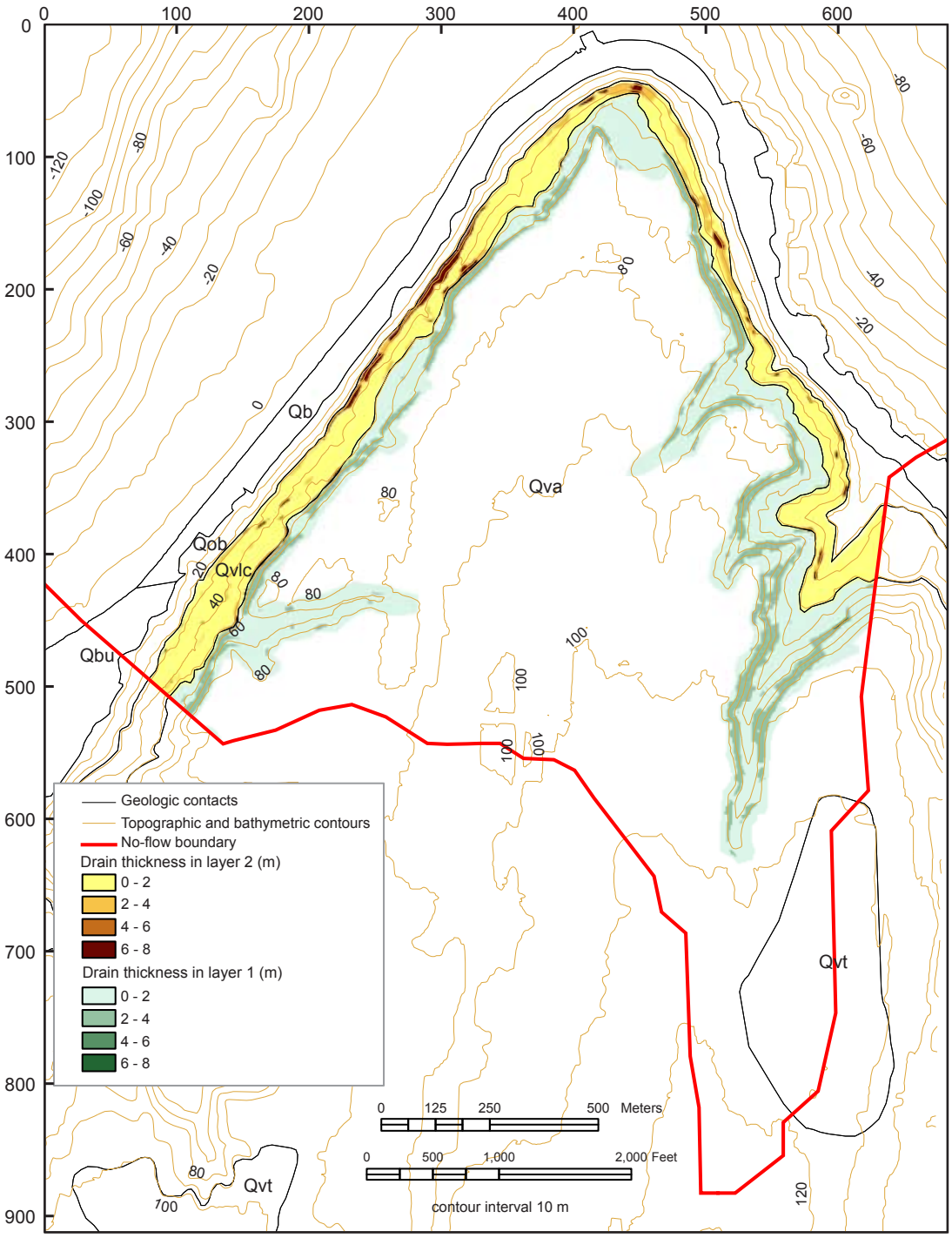

Figure 16. Map showing thickness of drain cells in ground-water flow model, geologic contacts, no-flow boundary, and topographic and bathymetric contours. See figure 3 for explanation of geologic unit symbols.

Table 2. Summary of parameters for the ground-water flow model and root-mean-square errors (RMSE) from sensitivity and calibration analyses of water levels in layer 1 (advance outwash deposits, Qva).

[C_{dr} is drain conductance, $C_{dr(initial)}$ is the drain conductance for version 1, K_n is the hydraulic conductivity of layer n, $K_{initial}$ is the hydraulic conductivity for version 1]

Version No.	Description	K_1 (m/s)	$K_{2,3}$ (m/s)	K_4 (m/s)	R(m/s)	C_{dr} (m^2/s)	RMSE
Step 1 - vary C_{dr}							
1	initial parameters	$1.0x10^4$	$5.0X10^9$	$1.5X10^5$	$1.5X10^8$	$0.02*K_{initial}$ *b	17.0
2	$5*C_{dr(initial)}$	$1.0X10^4$	$5.0X10^9$	$1.5X10^5$	$1.5X10^8$	$0.1*K_{initial}$ *b	18.1
2b	$2*C_{dr(initial)}$	$1.0X10^4$	$5.0X10^9$	$1.5X10^5$	$1.5X10^8$	$0.04*K_{initial}$ *b	17.6
3	$0.5*C_{dr(initial)}$	$1.0X10^4$	$5.0X10^9$	$1.5X10^5$	$1.5X10^8$	$0.01*K_{initial}$ *b	16.3
3b	$0.2*C_{dr(initial)}$	$1.0X10^4$	$5.0X10^9$	$1.5X10^5$	$1.5X10^8$	$0.004*K_{initial}$ *b	16.8
4	$0.1*C_{dr(initial)}$	$1.0X10^4$	$5.0X10^9$	$1.5X10^5$	$1.5X10^8$	$0.002*K_{initial}$ *b	20.4
Step 2 - using the best-fit parameters from step 1(version 3), vary K							
5	$0.5*C_{dr(initial)}$, $0.5*K_1$	$5.0X10^5$	$5.0X10^9$	$1.5X10^5$	$1.5X10^8$	$0.01*K_{initial}$ *b	15.3
6	$0.5*C_{dr(initial)}$, $0.25*K_1$	$2.5X10^5$	$5.0X10^9$	$1.5X10^5$	$1.5X10^8$	$0.01*K_{initial}$ *b	14.3
7	$0.5*C_{dr(initial)}$,$2*K_1$	$2.0X10^4$	$5.0X10^9$	$1.5X10^5$	$1.5X10^8$	$0.01*K_{initial}$ *b	17.1
8	$0.5*C_{dr(initial)}$, $0.5*K_2$	$1.0X10^4$	$2.5X10^9$	$1.5X10^5$	$1.5X10^8$	$0.01*K_{initial}$ *b	15.6
9	$0.5*C_{dr(initial)}$, $2*K_2$	$1.0X10^4$	$1.0X10^8$	$1.5X10^5$	$1.5X10^8$	$0.01*K_{initial}$ *b	62.5
9b	$0.5*C_{dr(initial)}$, $0.5*K_1$,$0.5*K_2$	$5.0X10^5$	$2.5X10^9$	$1.5X10^5$	$1.5X10^8$	$0.01*K_{initial}$ *b	14.7
10	$0.5*C_{dr(initial)}$, $0.25*K_1$,$0.5*K_2$	$2.5X10^5$	$2.5X10^9$	$1.5X10^5$	$1.5X10^8$	$0.01*K_{initial}$ *b	14.2
Step 3 - increase recharge using parameters with best RMSE (version 10)							
scenario 2	$0.5*C_{dr(initial)}$, $0.25*K_1$,$0.5*K_2$, R from average rainy-season precipitation	$2.5X10^5$	$2.5X10^9$	$1.5X10^5$	$2.5X10^8$	$0.01*K_{initial}$ *b	
scenario 3	$0.5*C_{dr(initial)}$, $0.25*K_1$,$0.5*K_2$, R from maximum 4-month precipitation	$2.5X10^5$	$2.5X10^9$	$1.5X10^5$	$6.0X10^8$	$0.01*K_{initial}$ *b	

Effects of Hydraulic Conductivity

Previously published estimates of hydraulic conductivity for each layer range over two or more orders of magnitude (table 1), making this a poorly constrained parameter. Using the best-fit estimate of drain conductance (version 3), we varied conductivity in layers 1, 2, and 3 (fig. 17*B* and *C*, versions 5-10). Decreasing the layer-1 conductivity (fig. 17*B*, versions 5 and 6) increased the layer-1 water table in the interior areas of the model domain and slightly decreased it near the bluff, significantly increasing the slope of the water table. Increasing the conductivity in layer 1 lowered the layer-1 water table for most of the study area, except near the bluffs, and decreased the slope of the water table (fig. 17*B*, version 7), resulting in a nearly flat water table.

Changes in conductivity for Qvlc (layers 2 and 3, where $K_2 = K_3$) also affected the level and shape of the layer-1 water table (fig. 17*C*). We found the lowest *RMSE* with a combination of decreasing the conductivity in layer 1 to one-fourth of the adjusted initial value and conductivity in layers 2 and 3 to one-half of the adjusted initial values (fig. 17*C*, version 10). We refer to this version, using recharge scenario 1, as our calibrated or best-fit model.

Effects of Increased Recharge

Using the calibrated ground-water model described above, we examined two recharge scenarios capable of elevating the water table at the bluff. Elevated pore pressures near the bluff could promote landsliding.

Increasing recharge to a value based on an average rainy-season monthly precipitation (fig. 17*D*, recharge scenario 2) increased heads in layer 1 by 0 to 8 m. Scenario 3, our "worst-case" scenario, used a recharge rate based on maximum 4-month precipitation and resulted in a water table elevated by as much as 28 m (fig. 17*D*). We used the heads resulting from the three recharge scenarios to calculate pore pressures for the 3-D slope-stability analysis described below.

Results of Ground-Water Flow Model

Simulated Water Levels

Figure 18 compares measured water-level observations in Qva to modeled heads in layer 1 for our best-fit model, the version with the lowest RMSE (version 10 with recharge scenario 1). Measured ground-water levels near the east bluff are higher than modeled estimates, whereas those near the west bluff are lower. Discrepancies may reflect measurement error in the water levels, or conditions that are different from the model, such as local heterogeneities, or inaccuracies in our layer descriptions or boundary conditions. Uniform variations in conductivities or recharge can raise or lower the water table, and variations in drain conductance can raise or lower the water table, with the most influence near the bluffs. However,

these uniform changes cannot raise water levels for one portion of the bluff while lowering water levels on another portion. Our best-fit model splits the difference in error between the east and west bluff.

Head Distribution, Hydraulic Gradients, and Flow Directions

Figure 19 shows the modeled hydraulic head in each of the layers with our best-fit parameters. Layer 1 and layer 4 (fig. 19*A* and *D)* are the aquifer units. The distribution of hydraulic heads in these layers is controlled by the conductivity of the layer, location and conductance of drains (layer 1), or location of constant head cells (layer 4). Layer 2 and 3 represent the Qvlc. The significant difference in head between layer 2 (fig. 19*B*) and layer 3 (fig. 19*C)* indicates a strong vertical component of flow between these two layers, both within Qvlc.

In this section, we focus mainly on the pressure heads and horizontal flow directions and gradients in Qva (layer 1), the layer we expect to have the greatest influence on slope stabil-

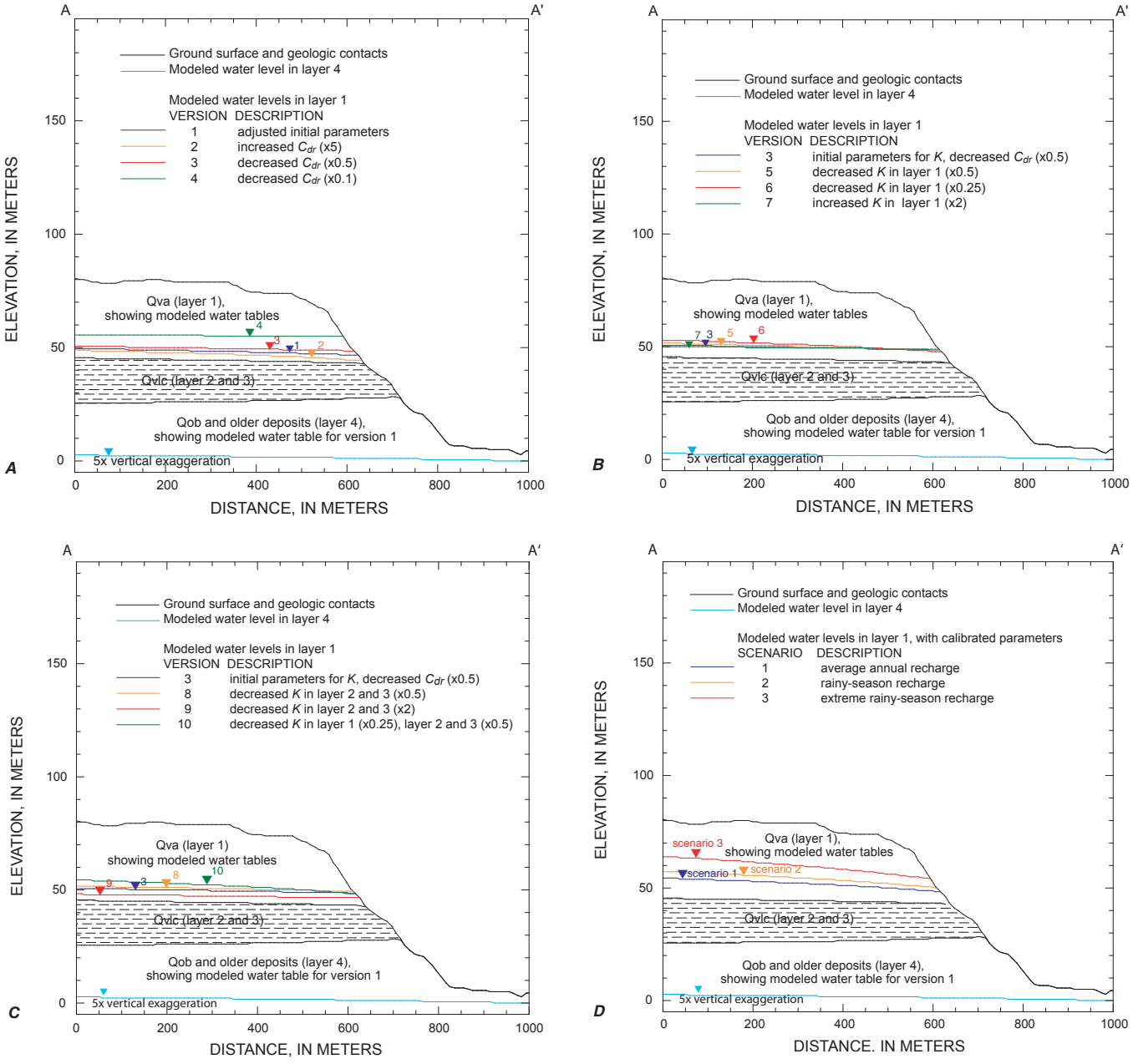

Figure 17. Results of ground-water-flow sensitivity analyses. Cross section A-A′ (see fig. 14 for location) shows simulated ground-water levels in layer 1 (Qva) for variations in several parameters: *(A)* drain conductance, C_{dr}, *(B)* hydraulic conductivity, *K*, in layer 1, *(C) K* in layers 1, 2, and 3, and *(D)* recharge, *R*. Note that version 10 with recharge scenario 1 is the calibrated model and the values for C_{dr} and *K* for this version are used with the other recharge scenarios. For layer 4, only the simulated water level with adjusted initial parameters is shown; the water level in this layer changed a maximum of 3 m with variations in the parameters. See figure 3 for explanation of geologic unit symbols.

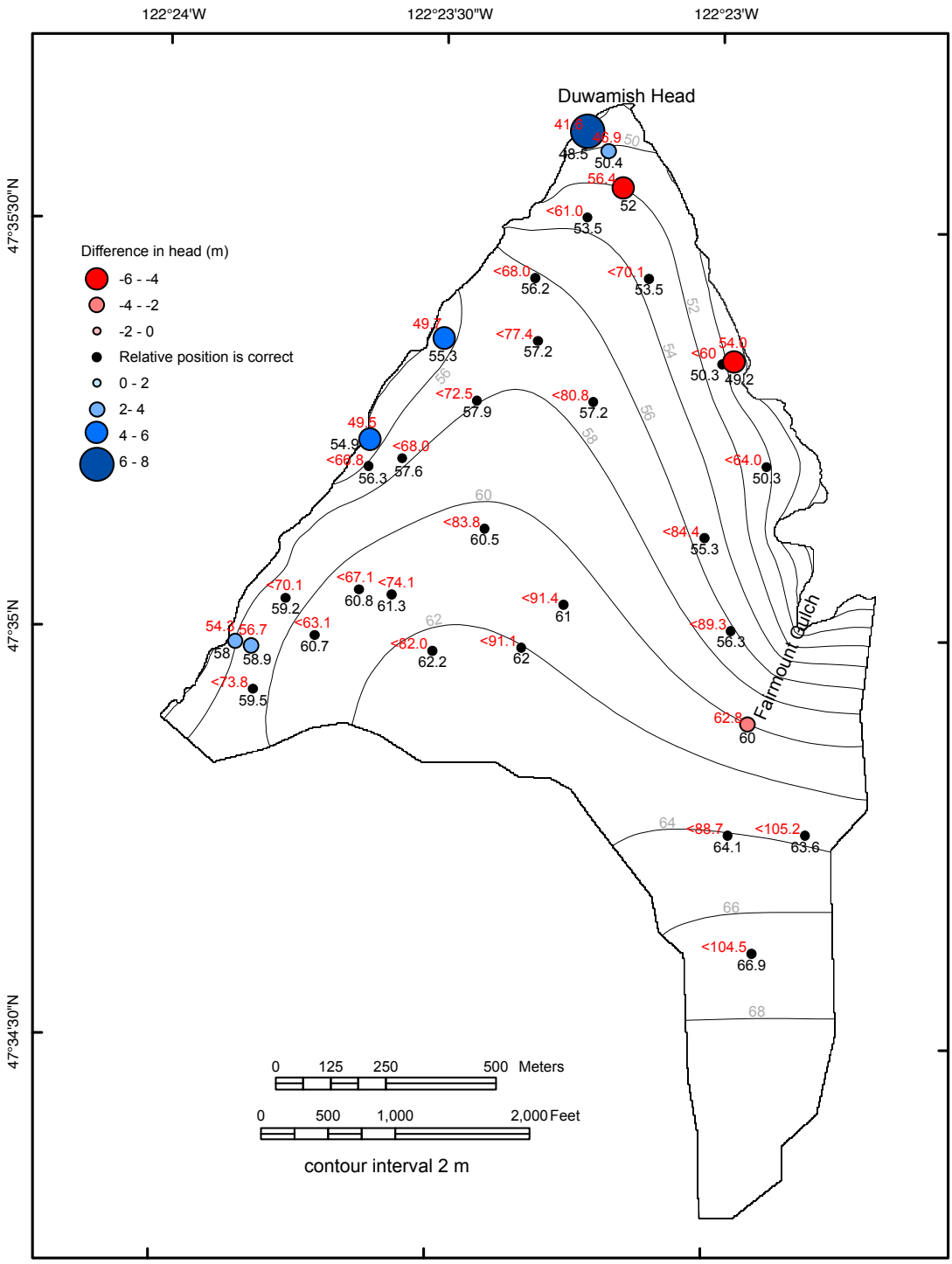

Figure 18. Contours of modeled hydraulic head in layer 1 (advance outwash deposits (Qva)) for the calibrated model, showing locations of measured water-level elevations used for calibration. Colored dots indicate differences between modeled and measured ground-water levels; red dots indicate where modeled head is lower than measured values, blue dots indicate where modeled head is higher than measured values, and black dots indicate where the borehole was not deep enough to reach the water table. Red numbers indicate measured elevation of water level and black numbers indicate modeled elevation of water level in layer 1; values are elevations in m. "Less than" symbols are used for boreholes not deep enough to reach the water table; these data constrain the relative position of the water table.

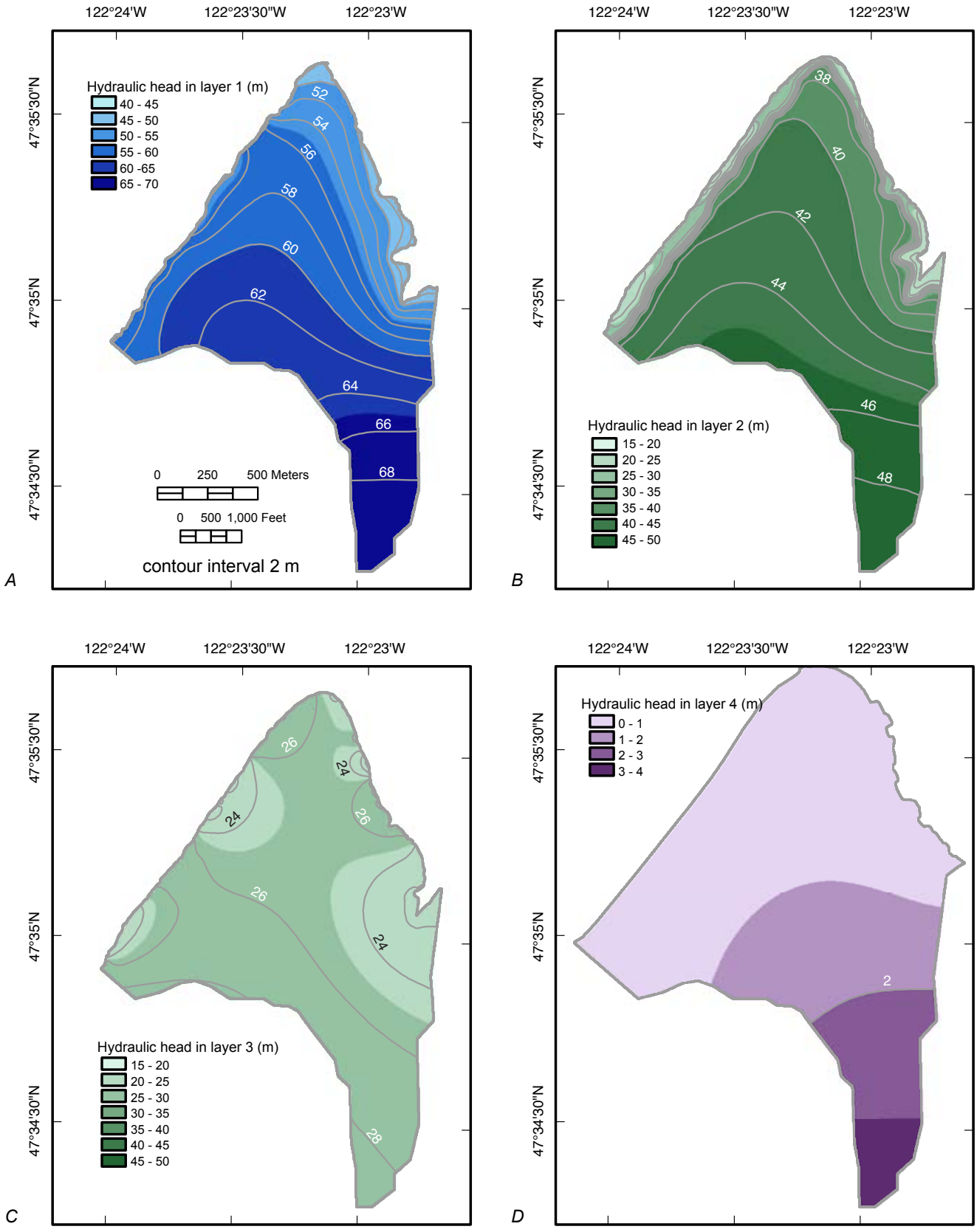

Figure 19. Map images showing modeled hydraulic head with calibrated parameters. Shown are heads *(A)* in Qva (layer 1), *(B)* in upper Qvlc (layer 2), *(C)* near bottom of Qvlc (layer 3), and *(D)* in Qob and older deposits (layer 4). See figure 3 for explanation of geologic unit symbols.

ity. For the slope stability analysis, we are interested in pore pressure, which can be directly calculated from pressure head. Pressure head is calculated from (Freeze and Cherry, 1979):

$$h = h_z + h_p \quad (13)$$

where:

h is total hydraulic head,
h_p is pressure head, and
h_z is elevation head.

Figure 20 shows the distribution of pressure head at the base of layer 1 for the three recharge scenarios. The scenarios with increased recharge (scenarios 2 and 3) show increases in pressure head, and therefore pore pressure, near the bluff. The largest pressure head increases occur near surface water drainages.

Figure 21 shows the generalized flow direction and horizontal hydraulic gradients, or slope of the water table, in layer 1 from our calibrated model. Flow is from the southern no-flow boundary toward the north, diverging from the inland areas toward the bluffs, and converging near major drainages. The flow pattern is affected by the land-surface topography that controls the location of seepage faces. Flow is also controlled by the elevation of the geologic contact between Qva and Qvlc. Water diverges away from higher elevation areas of this surface, resulting in relatively dry sections of the bluff, as along portions of the west bluff. Water converges in areas where this geologic contact occurs at relatively lower elevations, and these areas are generally wetter.

Vaccaro and others (1998) estimated horizontal hydraulic-head gradients for the upper aquifer of the Puget Sound aquifer system, based on generalized water-level configuration maps as ranging from $2x10^{-3}$ to $2x10^{-2}$, expressed in units of length/length (L/L). The modeled horizontal hydraulic gradients in layer 1 for our best-fit model are in this range or lower, ranging from $6.0x10^{-5}$ to $1.5x10^{-2}$, with a mean hydraulic gradient of $4x10^{-3}$. Although these values are on the low end of Vaccaro's estimates, our modeled water levels provide a reasonable match to measured ground-water levels and springflow (discussed below), and our values for hydraulic conductivity are within the range of published values. Gradients become slightly higher when recharge is increased—gradients resulting from average rainy-season precipitation range from $8.1x10^{-5}$ to $1.8x10^{-2}$, with a mean hydraulic gradient of $5.6x10^{-3}$, whereas those with recharge estimated from the maximum four-month precipitation are $1.4x10^{-4}$ to $2.7x10^{-2}$, with a mean hydraulic gradient of $9.1x10^{-3}$.

Water Budget

Inflow for the model comes solely from recharge at the ground surface, and outflow can leave from seepage faces, simulated as drain cells, or to the Puget Sound, simulated as constant head cells. The water budget for the average-annual-recharge simulation (scenario 1) allows 26 percent of the flow to exit through constant-head cells and 74 percent of the flow to exit through drain cells (table 3). As we increase recharge (scenarios 2 and 3), outflow increases from both the drain cells and the constant head cells. However, a higher percentage of flow exits through drain cells—82 percent with average rainy-season recharge (scenario 2), and 91 percent with recharge estimated from the maximum 4-month precipitation (scenario 3).

We compared the outflow from drain cells in our calibrated model using average annual recharge (scenario 1) to estimated flow from springs near the study area. Woodward and others (1995) estimated that spring flow along several bluff segments in southwestern King County ranges from 0.6 to 15 $m^3/s/km$. Our calibrated model yields 13 $m^3/s/km$ for the approximately 4.7 km length of bluff in the study area.

Seepage Zone

The seepage zone is the area of the ground surface where discharge from the drain cells occurs. Figure 22 shows the seepage zone in layer 1 (Qva) for our three recharge scenarios. Not shown is the seepage zone in layer 2 and 3; seepage from these layers is of negligible amount compared to layer 1. With increasing recharge, the area of the seepage zone increases upslope, with the largest increase typically in areas where ground surface slope is low, and near drainages, where ground-water flow converges. Figure 23 shows a 3-D perspective of the hydrogeologic layers and the seepage zone in Qva with recharge scenario 3.

Coupling of Slope-Stability Analysis with Ground-Water Flow Model

Our slope-stability analysis (described below) uses an estimate of pore pressure on the potential failure surface, in each column of the model. MODFLOW-2000 does not directly calculate pore pressures, but it does calculate a total hydraulic head in the center of each cell for each layer (fig. 24). In a separate step, before the slope-stability analysis, we use the output results from MODFLOW-2000 to calculate a 3-D pressure head distribution. This 3-D pressure-head distribution includes pressure heads at a number of specified elevations selected so that linear interpolation accurately calculates pressure head between these elevations. Potential slope instability near the bluff is a function of the pore-water pressure u, defined as:

$$u = \gamma_w h_p \quad (14)$$

where:

γ_w is the unit weight of water.

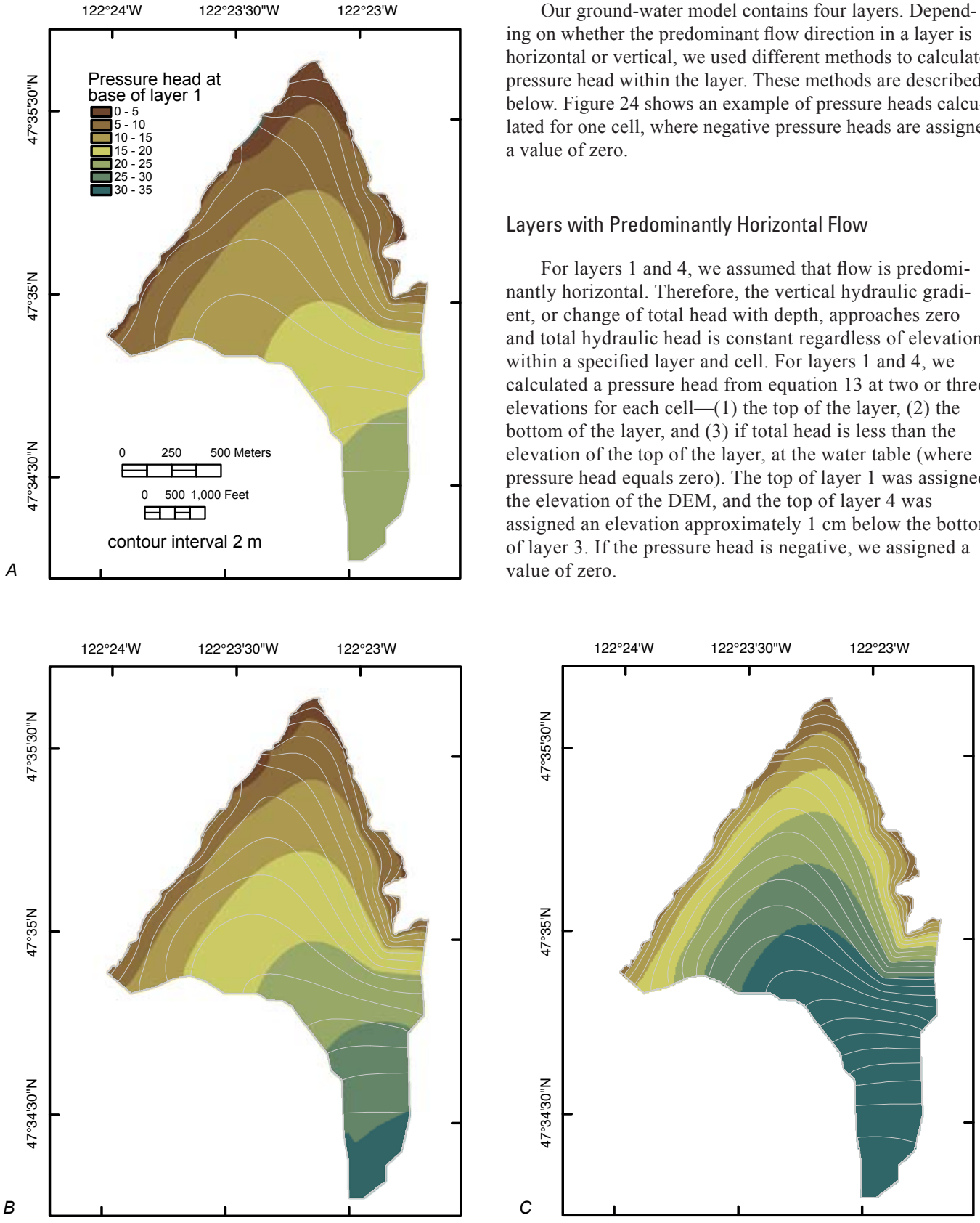

Our ground-water model contains four layers. Depending on whether the predominant flow direction in a layer is horizontal or vertical, we used different methods to calculate pressure head within the layer. These methods are described below. Figure 24 shows an example of pressure heads calculated for one cell, where negative pressure heads are assigned a value of zero.

Layers with Predominantly Horizontal Flow

For layers 1 and 4, we assumed that flow is predominantly horizontal. Therefore, the vertical hydraulic gradient, or change of total head with depth, approaches zero and total hydraulic head is constant regardless of elevation within a specified layer and cell. For layers 1 and 4, we calculated a pressure head from equation 13 at two or three elevations for each cell—(1) the top of the layer, (2) the bottom of the layer, and (3) if total head is less than the elevation of the top of the layer, at the water table (where pressure head equals zero). The top of layer 1 was assigned the elevation of the DEM, and the top of layer 4 was assigned an elevation approximately 1 cm below the bottom of layer 3. If the pressure head is negative, we assigned a value of zero.

Figure 20. Map images showing pressure-head distribution in layer 1 (advance outwash deposits, Qva) with calibrated parameters for three recharge scenarios: (*A*) average annual recharge (scenario 1, fig. 17*D*), (*B*) average rainy-season recharge (scenario 2, fig. 17*D*), and (*C*) extreme rainy-season recharge (scenario 3, fig. 17*D*). Contours show modeled hydraulic head in layer 1 for each recharge scenario.

Table 3. Summary of simulated groundwater outflow with three recharge scenarios.

Recharge scenario	Description of recharge scenario	Outflow through constant head cells (m^3/s)	Percentage of total to constant head cells	Outflow through drain cells (m^3/s)	Percentage of total to drain cells	Total outflow (m^3/s)
1	average annual	0.0068	25.8%	0.0195	74.2%	0.0263
2	average rainy season	0.0079	18.2%	0.0353	81.8%	0.0432
3	extreme rainy season	0.0099	9.4%	0.0949	90.6%	0.1048

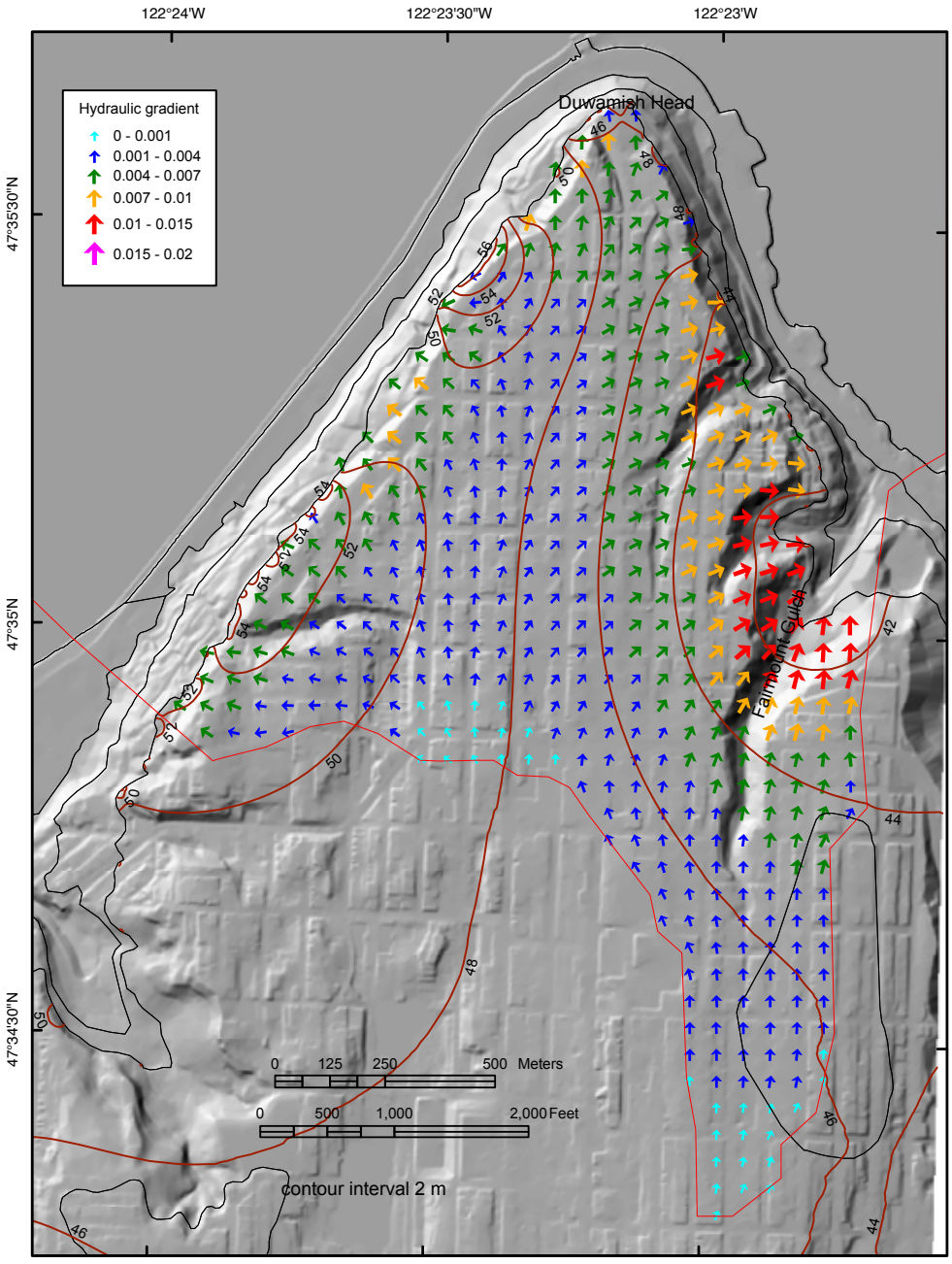

Figure 21. Map image showing generalized ground-water flow direction and hydraulic gradients in layer 1 (advance outwash deposits of the Vashon Drift, Qva) for calibrated parameters (fig. 17*C*, recharge scenario 1). Contours (red lines) and contour labels (black numbers) show elevation of geologic contact between Qva and Qvlc (Lawton Clay Member of the Vashon Drift). Geologic contacts are shown as black lines.

Layers with Predominantly Vertical Flow

If there is a dominant vertical component of flow, such as in Qvlc (layers 2 and 3 of the ground-water model), the total head changes with elevation. We calculated a vertical hydraulic gradient using total heads from layers within the hydrogeologic unit; for Qvlc, the layers are 2 and 3. For layers k and $k+1$ in cell i, j, the vertical hydraulic head gradient is defined as:

$$\frac{dh}{dz} = \frac{h_{i,j,k} - h_{i,j,k+1}}{z_{center(i,j,k)} - z_{center(i,j,k+1)}} \quad (15)$$

where:

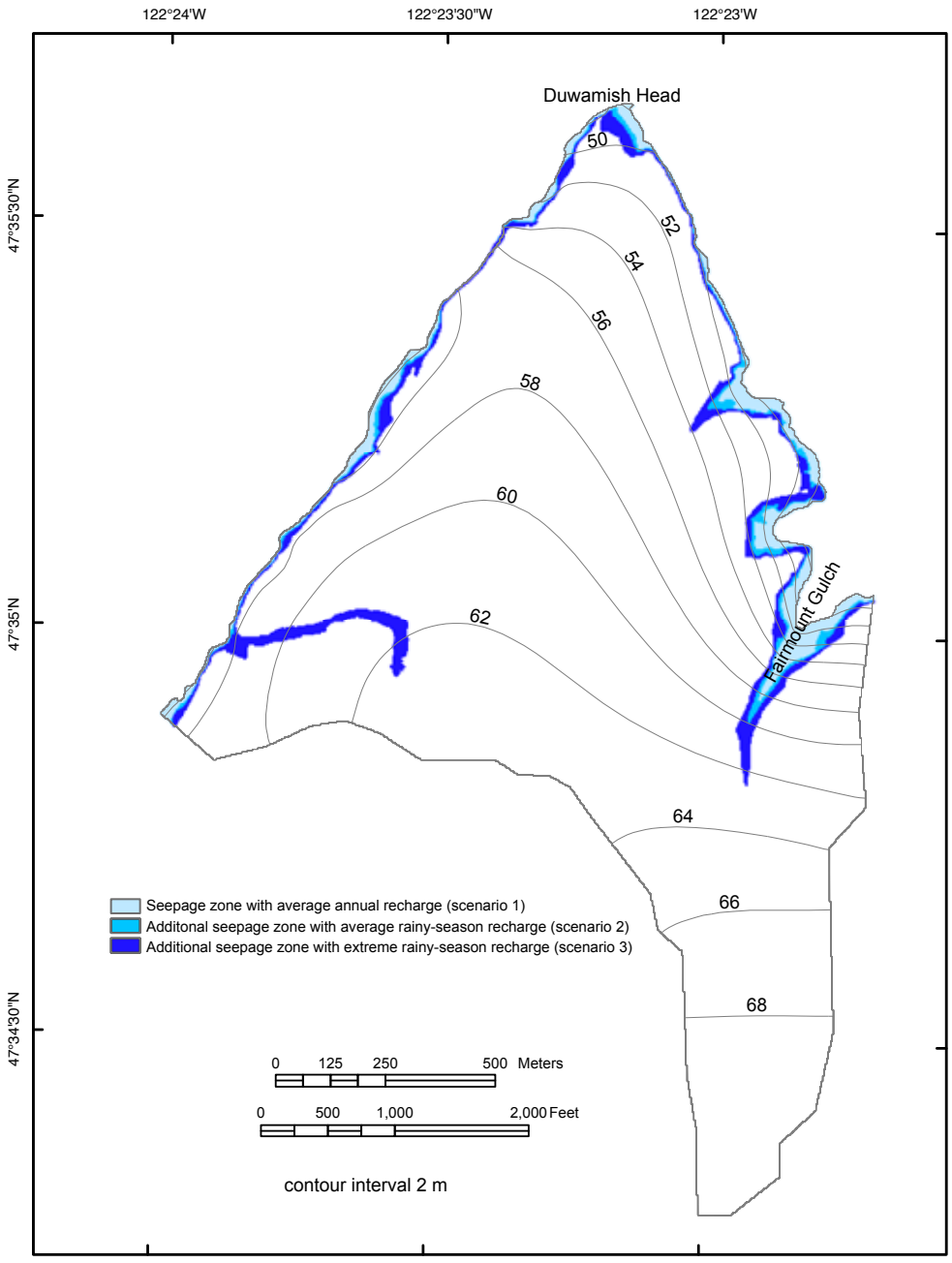

Figure 22. Image showing location of seepage zone using calibrated parameters for three scenarios of recharge: average annual recharge (scenario 1, fig. 17*D*), average rainy-season recharge (scenario 2, fig. 17*D*), and extreme rainy-season recharge (scenario 3, fig. 17*D*). Light-blue shading indicates area that has seepage in all three scenarios, medium blue is area added for scenario 2, and dark blue is area added for scenario 3. Contours (gray lines, black numbers) show modeled hydraulic head for scenario 1.

i, j, k are the numbers of the row, column, and layer; and $z_{center(i,j,k)}$ is the elevation at the center of the specified layer in the specified cell.

Note that z is positive upwards, but k increases downwards. For Qvlc, we calculated total hydraulic head at two elevations, the top of layer 2, and the bottom of layer 3. This procedure allows us to define the hydraulic head distribution over the complete thickness of Qvlc by extrapolating the vertical hydraulic gradient determined from the layer centers. The total head at the top of layer 2, calculated at approximately 1 cm below the top of the layer, is calculated with equations 16-18:

$$dz = (z_{top(i,j,k)} \text{-} 0.01 \text{ m}) \text{-} z_{center(i,j,k)} \quad (16)$$

where:

$z_{top(i,j,k)}$ is the elevation of the top of the layer at the specified cell.

$$dh = \frac{dh}{dz} * dz \quad (17)$$

Where dh/dz is obtained from equation 15. The total hydraulic head at the top of layer 2 is calculated:

$$h = h_{i,j,2} + dh \quad (18)$$

We then computed pressure head, h_p, from equation 13. If pressure head was negative, we assigned a value of zero. Using a similar set of equations, but substituting in the appropriate elevations, we computed pressure head at the bottom of layer 3.

Output to Slope-Stability Analysis

Using the methods described above, we calculated the 3-D pressure head distribution for each simulation. A file containing pressure head at the specified elevations was then used in our slope-stability analysis. The slope-stability analysis (described below) uses linear interpolation to calculate pressure head in a given cell on the potential failure surface using pressure head at the two closest elevations. Pore pressure was then calculated using equation 14.

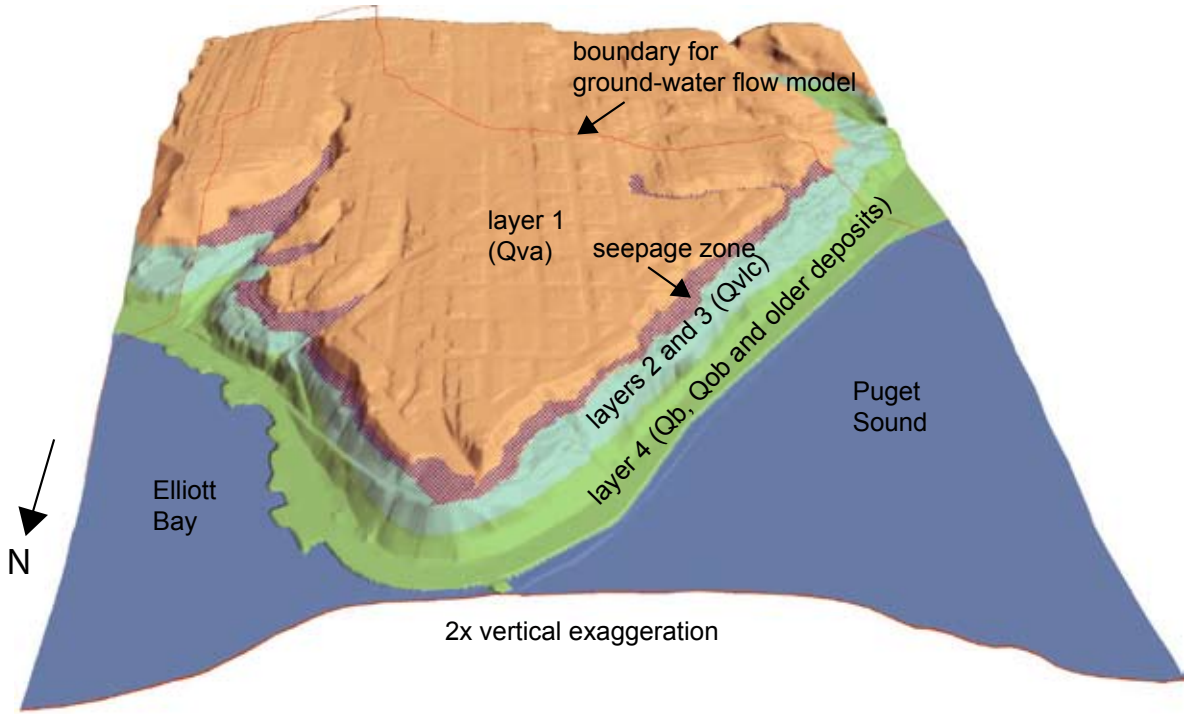

Figure 23. Perspective view of 3-D hydrogeologic layers used for ground-water flow model, showing seepage zone in layer 1 for extreme rainy-season recharge (recharge scenario 3, fig. 17*D*). Topography is from the City of Seattle digital elevation model (unpub. data) combined with bathymetry (http://sposerver.nos.noaa.gov/bathypacific.htm). See figure 3 for explanation of geologic unit symbols. Red line is the boundary for the ground-water flow model.

3-D Slope-Stability Analysis

To analyze stability of the bluffs in the study area, we used a 3-D limit-equilibrium analysis. Limit-equilibrium analysis examines the overall force balance of a rigid mass potentially sliding along a predefined failure surface. Potential for instability is assessed using a factor of safety (F) defined as the ratio of available shear strength to shear stress. Limiting equilibrium results when $F = 1$. A value of $F < 1$ indicates that the slope theoretically fails. For bluffs in the study area, we used an automated method that computes F for hundreds of thousands of potential failure surfaces encompassing all parts of the bluff. The computer program, named SCOOPS (Reid and others, 2000), keeps track of the minimum F (least-stable surface) computed for each node in the DEM.

We assumed arcuate failure surfaces, defined by the intersection of a sphere and the 3-D materials underlying the topography. Although shallow landslides can involve planar failure surfaces, deep-seated landslides in the Seattle area are often arcuate shaped as represented in schematic diagrams in previous studies (Laprade and others, 2000; Shipman, 2001).

SCOOPS uses a 3-D extension of Bishop's (1955) simplified method of slices for limit-equilibrium analyses. In 3-D, slices are extended to columns. SCOOPS computes 3-D limit-equilibrium in a manner similar to Hungr (1987). Bishop's (1955) limit-equilibrium analysis assumes that the average shear resistance, τ, acting on a potential failure surface, is defined by the Coulomb-Terzaghi failure rule:

$$\tau = c' + (\sigma_n - u)\tan\phi' \qquad (19)$$

where:
τ is average shear resistance,
c' is cohesion,
σ_n is total normal stress acting on the failure surface,
u is pore-fluid pressure on the failure surface, and
ϕ' is angle of internal friction.

Summing for all columns, the factor of safety, F, for our 3-D analysis is:

$$F = \frac{\sum R\left[c' A_c \cos\theta + (W - uA_c\cos\theta)\tan\phi'\right]/m_a}{\sum W(R\sin\alpha)} \qquad (20)$$

where:

(21)

F is factor of safety and is found iteratively,
R is the resisting force arm (equal to the failure surface radius),
A_c is the area of the failure surface intersecting the column,
θ is the true dip of the failure surface for the specified column,
W is the weight of the column above the failure surface, and
α is apparent dip of the failure surface for the specified column in the direction of slide movement.

SCOOPS extensively searches a DEM for potential failure surfaces (Reid and others, 2000). It systematically searches an orthogonal grid of search-grid points located above the DEM (fig. 25). Each search-grid point is the centroid of potential failure surfaces. From each search-grid point, SCOOPS identifies an initial radius and finds the intersection of the spherical surface and the DEM. If the intersection creates a potential failure mass with a volume equal to the minimum specified volume plus or minus a specified tolerance, a factor of safety for the mass is computed. The radius at each search-grid point is incremented by a defined amount until the volume reaches the maximum specified volume. During the search, SCOOPS keeps track of the potential failure surfaces with the minimum F calculated for each DEM grid node, these are called critical surfaces.

Points for calculation of head	
no.	h_p (m)
1	0
2	0
3	7.6
4	6.4
5	0
6	0
7	0
8	150.6

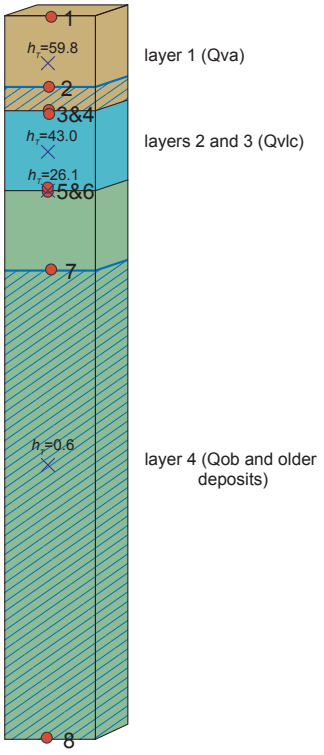

Figure 24. Diagram illustrating computation of pressure head in hydrogeologic layers. Shown is one cell with hydrogeologic layers, water tables, total hydraulic head (h_T) shown at the elevation of the middle of each layer, and elevations where pressure head (h_p) is calculated (black numbers with red dots: 1-8). Pressure heads calculated using equations 13, and 15-18 are shown in adjoining list. See figure 3 for explanation of geologic unit symbols.

Table 4. Summary of strength properties used in slope-stability analyses.

[c' is cohesion, ϕ' is angle of internal friction, γ_{dry} is unit weight of dry material, γ_{wet} is unit weight of saturated material. The unit weight for dry material is also used for partially saturated materials]

Geologic Unit	c' (kPa)	ϕ'	γ_{dry} (kN/m^3)	γ_{wet} (kN/m^3)
Advance outwash deposits - Qva	10	38	18	20
Lawton Clay Member - Qvlc	29	26	17	19
Olympia beds (Qob) and older	19	34	18	20
Beach sands - Qb	0	34	18	20

We assessed potential failures in two volume ranges—(1) moderately large failures, from 3,000 to 30,000 m^3, and (2) very large failures, from 30,000 to 300,000 m^3. The lower limit of 3,000 m^3 is approximately the size of the 75th percentile of Seattle landslides with an estimated depth greater than 2 m (fig. 6). The very large volume range is in the range of several historical deep-seated landslides, including the Perkins Lane and Woodway landslides. By using two volume ranges, we can evaluate stability of moderately large failures that might occur in locally steep areas, as distinguished from larger volume failures that might occupy large areas comparable in size to several of the largest historical landslides.

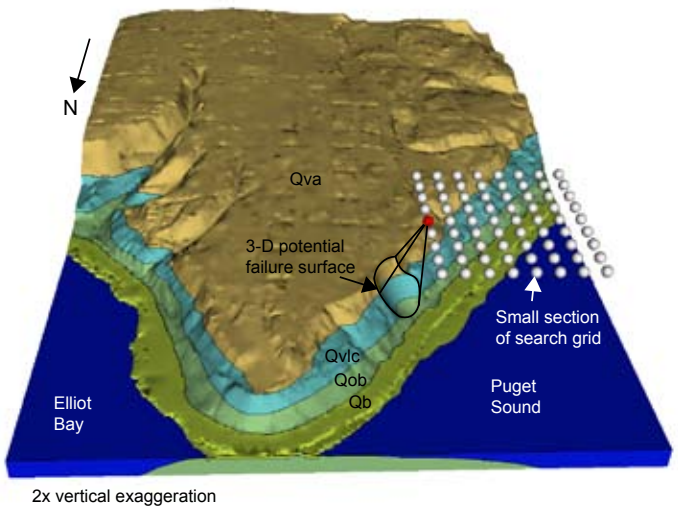

Figure 25. Schematic diagram of study area landscape as represented by a digital elevation model (DEM), geologic units, one layer of a section of the search grid, and a potential 3-D trial potential failure surface (outlined in black) projected from one search grid point (red dot). Topography is from the City of Seattle DEM (unpub. data) combined with bathymetry (http://sposerver.nos.noaa.gov/bathy/pacific.htm). See figure 3 for explanation of geologic unit symbols.

Geotechnical Properties

We assigned strength and unit-weight values to four geologic units in the study area (table 4) on the basis of previously published values (Savage and others, 2000b; Debray and Savage, 2001; Harp and others, 2006). Shear strength of geologic units is a function of cohesive strength *(c′)*, and frictional strength (ϕ'). Layers in the slope-stability analysis are similar to the hydrogeologic layers used in the ground-water model, with two exceptions—(1) beach deposits (Qb and Qbu) form a separate layer and (2) the Lawton Clay Member (Qvlc) consists of one layer rather than two. The four layers for the slope-stability analysis (fig. 25) are (1) Qva, (2) Qvlc, (3) Qob and older deposits, and (4) Qb and Qbu. Qvt is not present on the bluffs and was not included in any of the layers for the slope-stability analysis.

We assigned shear strengths to these four geologic layers from the values used for assessment of shallow landslide hazards (Harp and others, 2006). These values were based on average values from shear-strength tests. Unit weights were assigned based on the values used for a finite-element limiting-equilibrium analysis of the stability of the Woodway landslide (Debray and Savage, 2001). Sensitivity to these strength values is examined appendix C.

Results

The results of our slope-stability analysis are shown by maps of the factor of safety (F) and associated volumes for critical surfaces. Critical surfaces are the potential failure surfaces with the minimum calculated F at each DEM grid node. Here, we compare results for dry conditions with results using 3-D pore pressures calculated from our ground-water model for the three recharge scenarios.

Initially, we examined the effects of gravitational stress in dry materials with heterogeneous strength properties (figs. 26*A* and 27*A*). For the moderately large volume search (3,000 to 30,000 m^3), the minimum F for all critical surfaces (F_{min}) is 1.10. Although this global minimum is of interest, we would

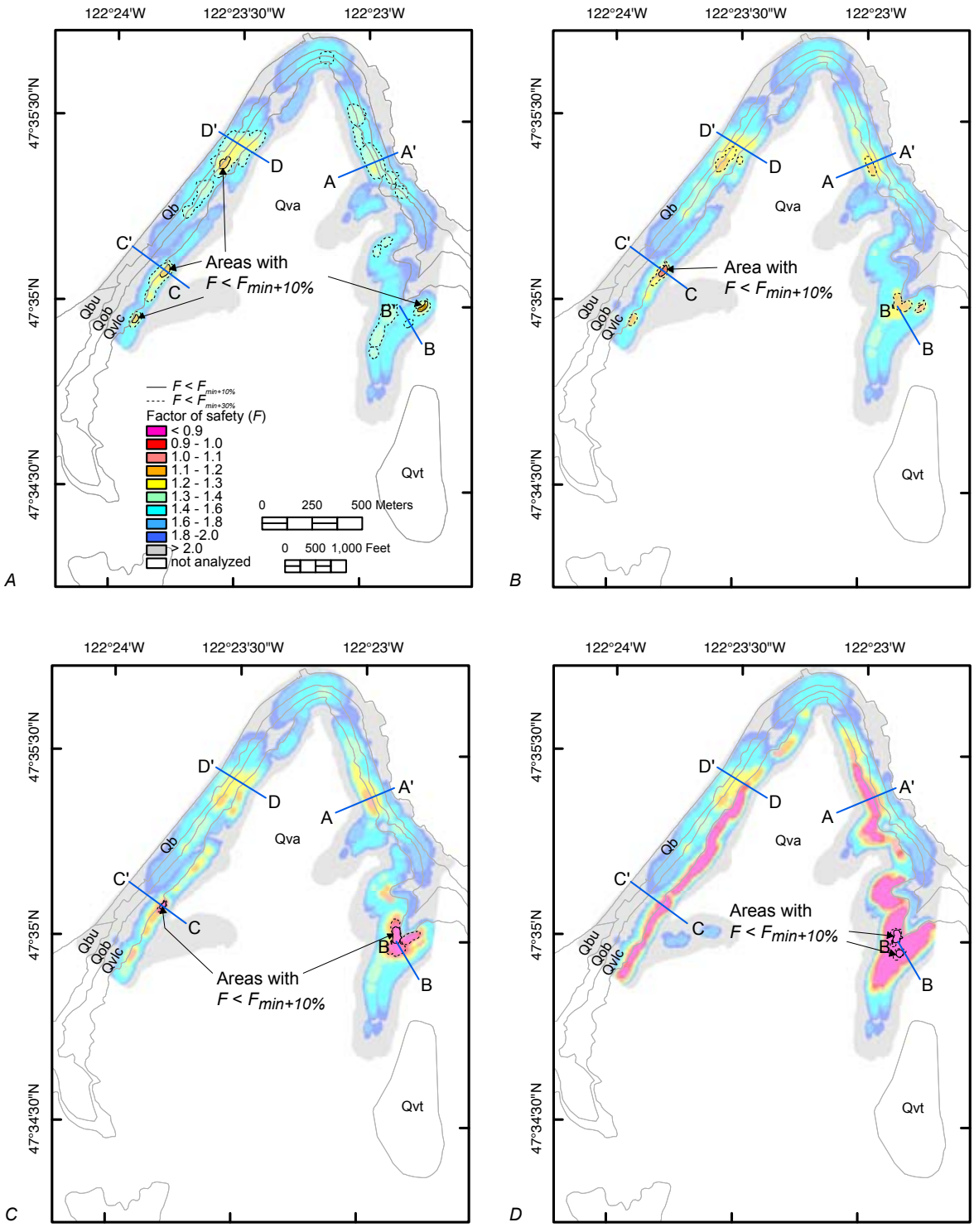

Figure 26. Map images showing factor of safety *(F)* for critical surfaces with associated volumes between 3,000 and 30,000 m^3. A critical surface is the potential failure with the lowest *F* at each digital elevation model grid node. *F* is indicated by color, and areas of relatively low stability are outlined: $F < F_{min+10\%}$, solid black line, and $F < F_{min+30\%}$, dashed black line. Results are shown for *(A)* dry conditions, *(B)* average annual recharge, *(C)* average rainy-season recharge, and *(D)* extreme rainy-season recharge. A-A', B-B', C-C', and D-D' are locations of cross sections in figure 32. Geologic contacts are shown as gray lines. See figure 3 for explanation of geologic unit symbols.

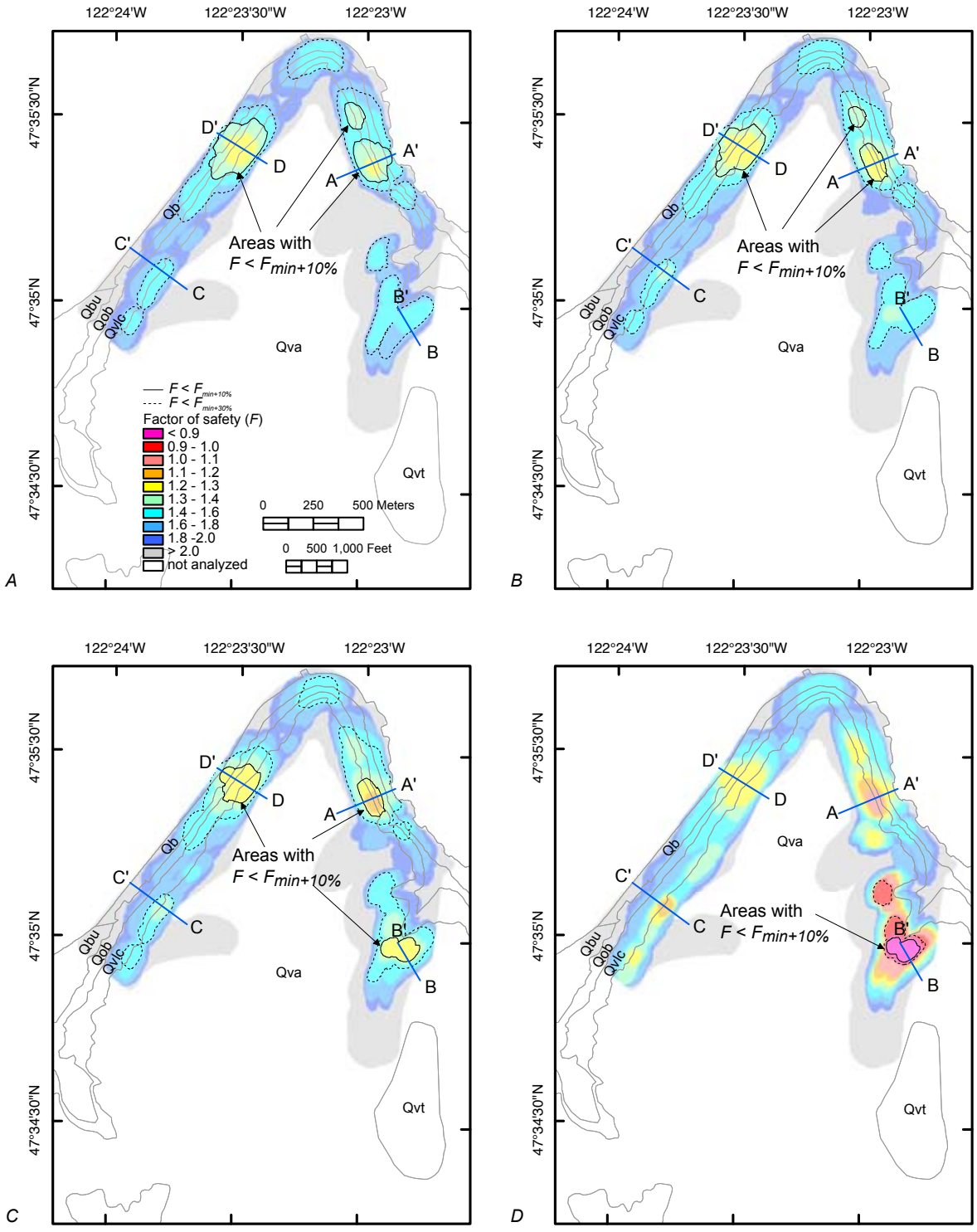

Figure 27. Map images showing factor of safety *(F)* for critical surface with associated volumes between 30,000 and 300,000 m^3. A critical surface is the potential failure with the lowest *F* at each digital elevation model grid node. *F* is indicated by color, and areas of relatively low stability are outlined: $F < F_{min+10\%}$, solid black line, and $F < F_{min+30\%}$, dashed black line. Results are shown for *(A)* dry conditions, *(B)* average annual recharge, *(C)* average rainy-season recharge, and *(D)* extreme rainy-season recharge. A-A', B-B', C-C', and D-D' are locations of cross sections in figure 32. Geologic contacts are shown as gray lines. See figure 3 for explanation of geologic unit symbols.

also like to identify areas of relatively low stability. To show the least-stable areas, we highlight areas with F less than F_{min} + 10%*F_{min} and less than F_{min} + 30%*F_{min}. We refer to these regions respectively as $F_{min+10\%}$ and $F_{min+30\%}$. For dry conditions and moderately large volumes (fig. 26*A*), the least-stable areas encompass steep topography and the surrounding areas (figs. 26*A*, and 28). Potential failures for the moderately large volume search commonly include only one geologic unit, but in some locations encompass multiple units.

For dry conditions with the very large volume (30,000 to 300,000 m^3) search, F_{min} is 1.29, and the least-stable surfaces typically encompass large areas in multiple geologic units (fig. 27*A)*. The focus here is less concentrated on small areas of locally steep ground.

With the addition of 3-D pore pressures calculated from our ground-water model using average annual recharge (ground-water model recharge scenario 1), locations of the least-stable surfaces change slightly for the moderately large volume search, and stability in Qva starts to decrease (figs. 26*B* and 27*B)* relative to the results for dry conditions. On the western bluff, there is a pattern of factors of safety almost identical to dry conditions; however, on the eastern bluff, some areas have lower stability (new yellow areas) relative to the surrounding areas (fig. 26*B)*. Results for the very large volume search also show decreased stability in Qva. The minimum F is 0.95 for the moderately large volume search and 1.22 for the very large volume search. The areas with $F < F_{min+30\%}$ change subtly for both volume ranges; changes are most apparent in Fairmount Gulch, and, for the very large volume search, near the yellow area on the eastern bluff.

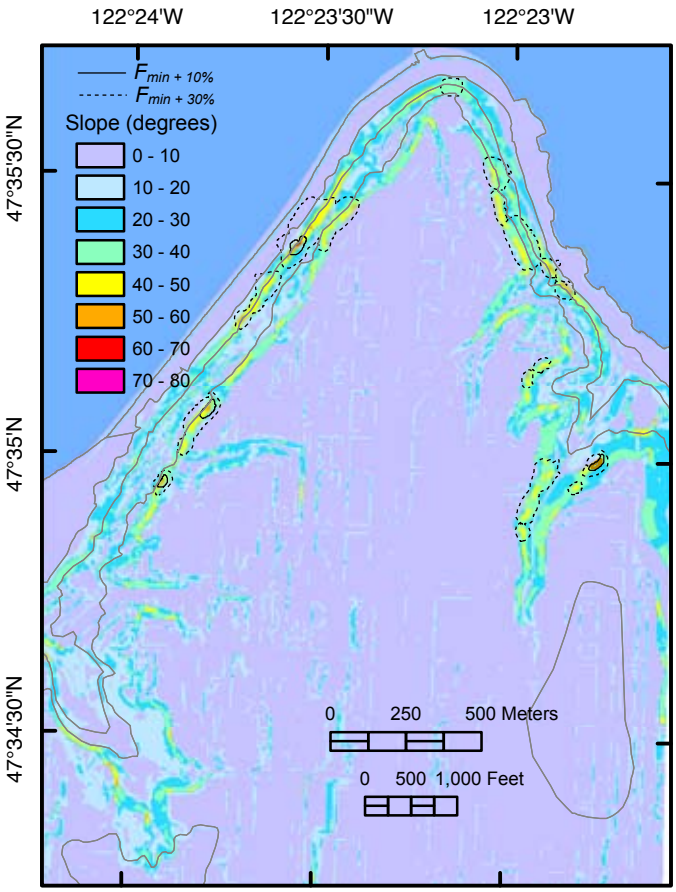

Figure 28. Slope map showing outlines of areas of relatively low stability for dry conditions and moderately large potential failure volume search: $F < F_{min+10\%}$, solid black line, and $F < F_{min+30\%}$, dashed black line. Geologic contacts are shown as dark gray lines.

Maps showing the percent difference ((F_{wet} - F_{dry})/F_{dry})*100) in stability from wet conditions to dry conditions highlight areas where the influence of pore pressures is greatest (figs. 29 and 30). With recharge scenario 1 and moderately large volumes, factor of safety decreases by as much as 52 percent in areas of ground-water convergence located near the contact between Qva and Qvlc (fig. *29A)*. With very large volumes, the factor of safety decreases by 22 percent or less (fig. 30*A)*. In this case, surfaces with the largest decrease in stability are deeper surfaces that include mostly Qva and are located near the Qva/Qvlc contact. For both volume ranges, areas with the largest percentage change in F are in Fairmount Gulch and in the smaller reentrants just north of Fairmount Gulch.

Next, we show results with the addition of average rainy-season recharge (recharge scenario 2). For moderately large volumes, factors of safety decrease and the areas with $F < F_{min+10\%}$ shift from Qvlc to Qva (fig. 26*C)*, with most of the least-stable surfaces located in Fairmount Gulch. The minimum factor of safety for moderately large potential failures decreases to 0.75. For very large volume potential failures (fig. 27*C)*, F_{min} is 1.18, and multiple geologic units are typically involved, except for areas in Fairmount Gulch where relatively unstable critical surfaces often intersect only Qva. Here, the maximum change in factor of safety between wet and dry conditions is 67 percent for moderately large volume potential failures (fig. 29*C)* and 33 percent for very large volume potential failures (fig. 30*C)*. The smaller decrease in stability for larger potential failures is due to the depth of very large volume potential failure surfaces; although they intersect more of the water table in Qva, they also include other hydrogeologic units with lower pore pressures.

Finally, by using 3-D pore pressures derived from extreme rainy-season recharge (recharge scenario 3), we show that a significant portion of the bluff in Qva has $F < 1$, indicated by pink and dark red areas on the maps (figs. 26*D* and 27*D)*. The least-stable surfaces for both volume ranges are located in Fairmount Gulch. F_{min} is equal to 0.31 for the moderately large volume search and equal to 0.75 for the very large volume search. Relative to dry conditions, the high pore pressures in this scenario significantly decrease stability over a large area of Qva (figs. 29*C*, and 30*C)*. Change in factor of safety between wet and dry conditions becomes as great as 85 percent with moderately large volume potential failures (fig. 29*C)*.

Volume maps show the volume associated with the critical surface at each DEM node. In our search for the least-stable potential failures encompassing moderately large volumes (3,000 to 30,000 m^3), potential failures with $F < F_{min+30\%}$

typically have volumes near the lower limit (3,000 m^3) of our search range (fig. 31*A*). We show volume maps for average rainy-season recharge. The volume maps for other recharge scenarios are similar.

In our larger volume search, the least-stable potential failures ($F_{min+30\%}$) encompass a range of volumes, with the majority near the low end (less than 50,000 m^3) of our volume limits (fig. 31*B*). One relatively unstable area on the northwest bluff also includes some larger volume potential failures (outlined in green, shaded with light browns), in the range of 200,000 to 250,000 m^3.

Figure 32 shows some examples of potential failure surfaces, the geologic units affected, and simulated water tables in Qva and Qob and older deposits. The potential failure surfaces illustrate typical critical surfaces and are the critical surfaces for at least one of the volume ranges with extreme rainy-season recharge; they are not necessarily the least-stable surfaces within the study area for all scenarios nor are they a critical surface for every recharge scenario, but other scenarios typically have a similar critical surface. For each cross section, we show at least one moderately large volume critical surface in Qva, and for an area on the west bluff (D-D') where Qvlc is steep and relatively unstable, we show a potential failure surface containing only Qvlc (fig. 32*D*). We also show one very large volume potential failure surface that may include Qva, Qvlc, and possibly Qob and older deposits. Factor of safety and change in factor of safety relative to dry conditions

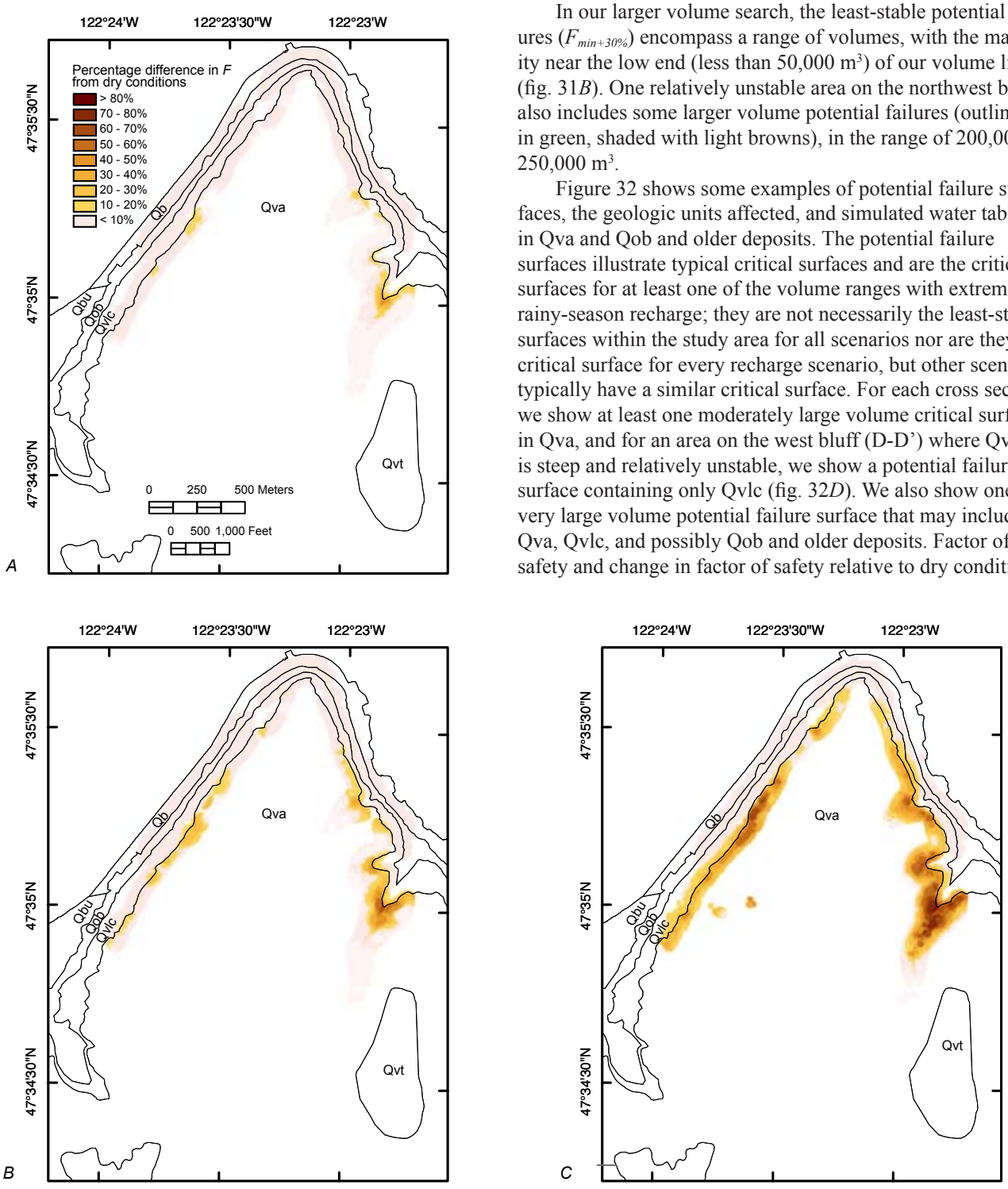

Figure 29. Map images showing percentage difference in factor of safety (F_{wet}/F_{dry} * 100) between wet conditions and dry conditions for critical surfaces with associated volumes between 3,000 and 30,000 m^3. Percentage difference shown for surfaces with $F < 2$ with wet conditions. Results are shown for (*A*) average annual recharge, *(B)* average rainy-season recharge, and *(C)* extreme rainy-season recharge. Geologic contacts are shown as black lines. See figure 3 for explanation of geologic unit symbols.

for each of these surfaces is listed in table 5. For moderately large volume potential failures intersecting Qva, increasing the water tables in Qva has a strong influence on stability.

Discussion

Historical observations (Tubbs 1974, 1975; Wait, 2001; Baum, oral commun., 2004) describe deep-seated landslides as often occurring in Qva or near the contact between Qva and Qvlc. We first compare this general observation with the results of our slope-stability analyses, and then we then compare mapped deep-seated landslides with our results for both volume searches.

Our results highlight the predicted least-stable portions of the bluff. With dry conditions and moderately large volume failures, these potential failures are found on the steepest areas of the bluff. With the addition of pore pressures generated from our 3-D ground-water flow model, we are better able to represent observed hydrologic conditions and predict relatively unstable areas similar to historical locations of landslides. The addition of 3-D pore pressures shifts the location of the least-stable surfaces away from locally steep areas in Qvlc to steep portions of Qva. This shift is most pronounced with 3-D pore pressures from average rainy-season recharge or extreme rainy-season recharge (ground-water scenarios 2 or 3).

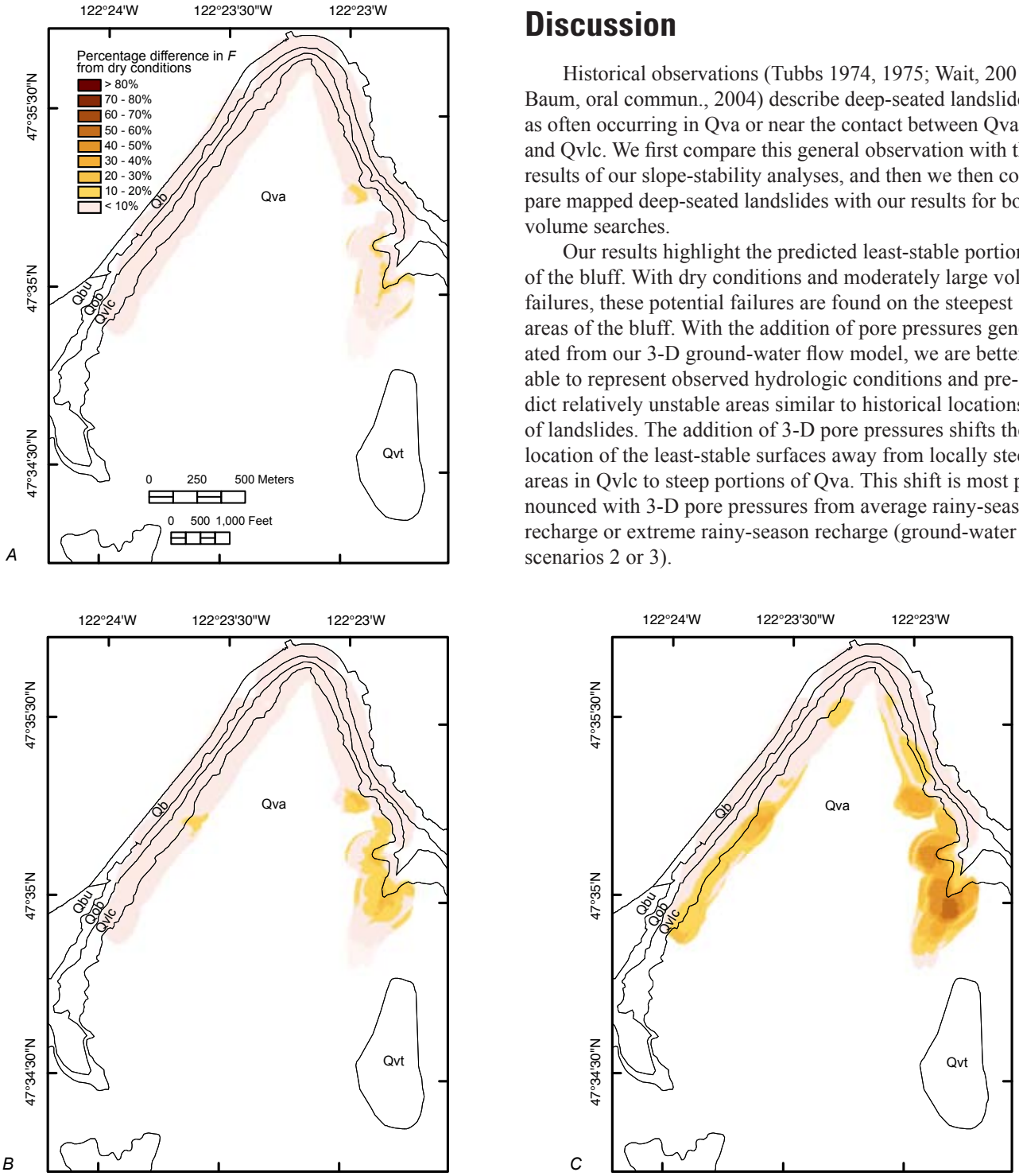

Figure 30. Map images showing percentage difference in factor of safety (F_{wet}/F_{dry} * 100) between wet conditions and dry conditions for critical surfaces with associated volumes between 30,000 and 300,000 m^3. Percentage difference shown for surfaces with $F < 2$ for wet conditions. Results are shown for (*A*) average annual recharge, (*B*) average rainy-season recharge, and (*C*) extreme rainy-season recharge. Geologic contacts are shown as black lines. See figure 3 for explanation of geologic unit symbols.

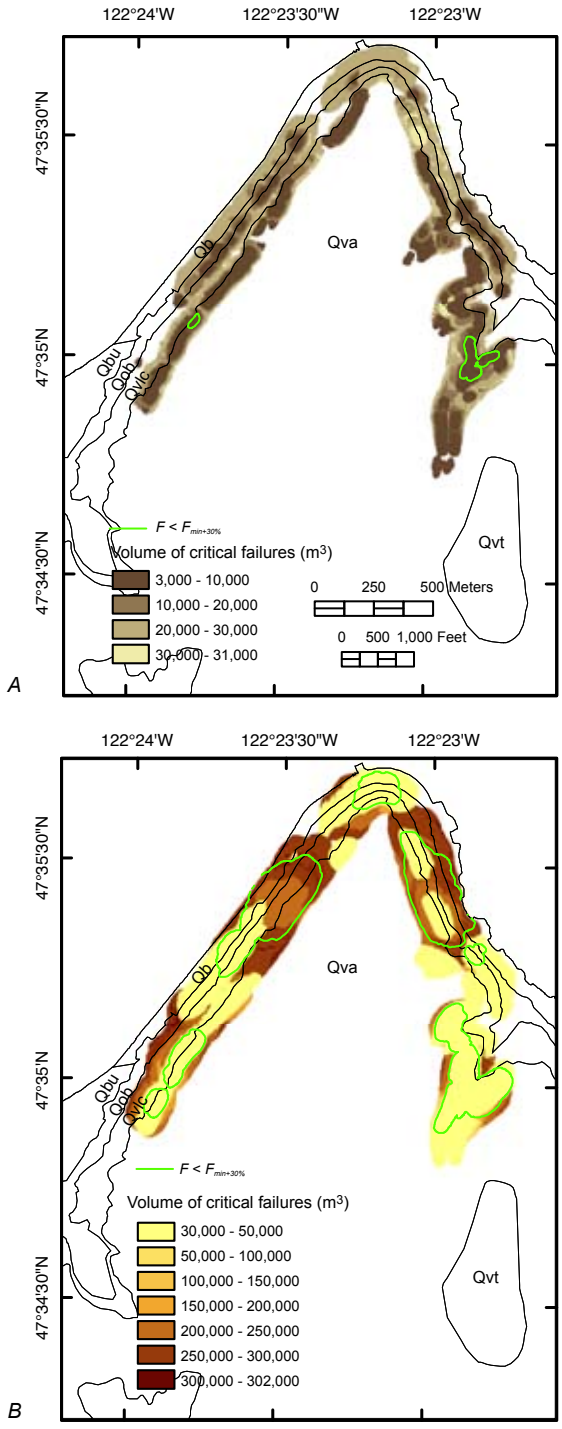

Figure 31. Map images showing volumes associated with critical surfaces identified using average rainy-season recharge. Volumes are shown for surfaces with $F < 2$. Green outline shows area with $F < F_{min+30\%}$. Results are shown for volume ranges between 3,000 and 30,000 m^3 (*A*), and between 30,000 and 300,000 m^3 (*B*). Note that simulations identify surfaces with volumes up to the maximum specified volume (V_{max}) plus a tolerance; therefore, some volumes are slightly greater the specified maximum. Geologic contacts are shown as black lines. See figure 3 for explanation of geologic unit symbols.

We briefly compare each landslide map (Youngmann, 1979; Laprade and others 2000; Wait, 2001; Schulz, 2004; Troost and others, 2005) with our simulation results for an average rainy-season recharge (recharge scenario 2). Each type of mapping has advantages and disadvantages (Schulz, 2004). The locations of mapped deep-seated landslides, when compared with our factor-of-safety map (figs. 33-35), reveal both similarities and differences between the locations of past landslides and the least-stable areas predicted by our analysis.

Laprade and others (2000) identified point locations at the center of historical landslide headscarps. These data include events from more than 100 years of historical records, and include 20 mapped deep-seated landslides in our study area. Portrayal as points is not ideal for comparison because points do not show the areas of the landslides. Some of the point locations identified as deep-seated landslides fall within the predicted less stable ground ($F < F_{min+30\%}$) of our simulations, but many point locations are within areas of predicted more stable ground ($F > F_{min+30\%}$). The success rate is slightly better for the simulations with very large potential failure volumes, in part because the least-stable surfaces encompass a larger area on the map.

Other previously compiled maps identify large landslide complexes (Schulz, 2004) or landslide scarps (Troost and others, 2005). The large areas delineated by these maps represent landslide complexes that have developed since the retreat of the last continental glacier from the region. These areas affect the entire western bluff and parts of the eastern bluff. The least-stable areas identified by our simulations occur mostly within these large mapped areas.

For comparison with our analysis, we would expect the most useful landslide maps to be those that identify landslides that have occurred historically and that define the area of the landslide, rather than a point or extremely large area. Two maps show areas of historically active, large deep-seated landslides (Youngmann, 1979; Wait, 2001); however, many of the mapped historically active landslides occur in reactivated old landslides and colluvial deposits. Many of the areas of historical landsliding are not identified as areas of least-stable ground in our simulations when we use average rainy-season recharge and moderately large volumes (fig. 33). Based on the area encompassed by individual mapped landslides, it is more appropriate to compare these landslides with results from our very large volume search.

Our simulation results using very large volumes and average rainy-season recharge identify low stability in two areas of historical instability (figs. 34, and 35). Areas of $F < F_{min+30\%}$ include most of the Bonair Drive and California Way SW landslides, plus areas adjacent to these landslides. The areas with lowest stability ($F < 1.3$, shown with red, orange and yellow) do not correspond directly with the mapped landslide locations but rather with adjacent steeper ground. Areas with $F < F_{min+30\%}$ do not encompass the areas of historical landsliding near Duwamish Head or Alki Avenue SW, rather the analysis identifies some areas where historical deep-seated landsliding has not been identified, although shallow colluvial

landslides have occurred, in particular, the Fairmount Gulch area (Laprade and others, 2000). The predicted low stability in Fairmount Gulch is due to simulated high pore pressures that result from convergence of ground-water flow. Seepage erosion, the entrainment of soil resulting from water flowing through and emerging from the soil (Dunne, 1990), is a common process in the development and growth of drainages (Baker and others, 1990; Dunne, 1990; Higgins and others,

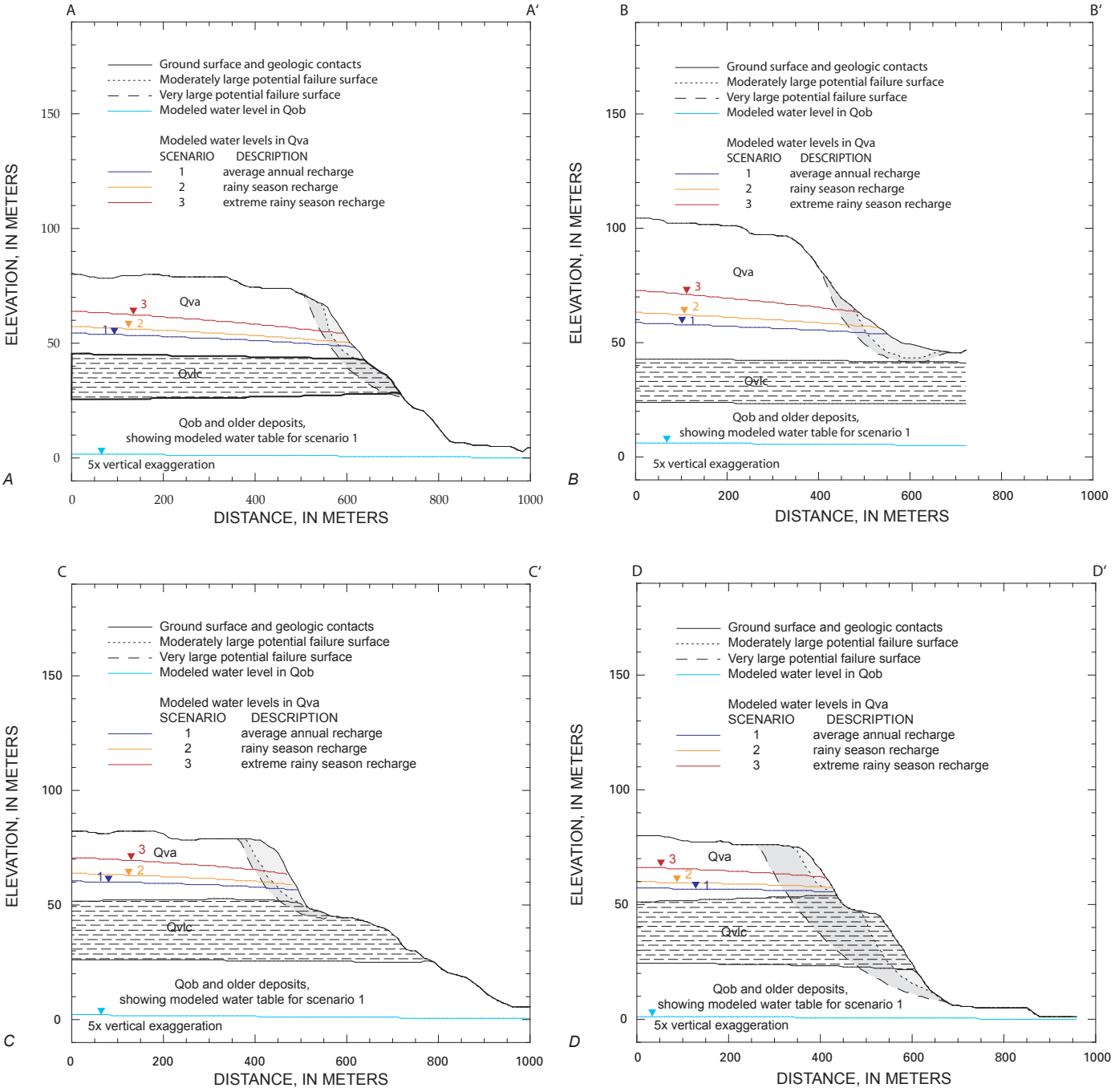

Figure 32. Cross sections showing examples of potential failure surfaces generated from moderately large volume (3,000 to 30,000 m^3) and very large volume (30,000 to 300,000 m^3) searches. The potential failure surfaces illustrate typical critical surfaces. These examples are critical surfaces with extreme rainy-season recharge. Simulated water tables in Qva for three recharge scenarios are shown. Water table in Qob and older deposits for average-annual recharge is shown. Cross sections shown are *(A)* Cross-section A-A′ on northeast bluff, *(B)* Cross-section B-B′ in Fairmount Gulch, *(C)* Cross-section C-C′ on northwest bluff, and *(D)* D-D′ on southwest bluff, see figures 26 and 27 for locations. See table 5 for factors of safety of the surfaces shown. See figure 3 for explanation of geologic unit symbols.

Table 5. Factors of safety *(F)*, percent change in factor of safety relative to dry conditions, geologic units (see fig. 3), and volumes for potential failures shown in figure 32.

Cross section	Geologic materials	Volume (m^3)	Factor of Safety, *F*				% change in factor of safety, *F*		
			Dry	Average annual recharge	Rainy-season recharge	Extreme rainy-season recharge	Average annual recharge	Rainy-season recharge	Extreme rainy-season recharge
A-A'	Qva	3,491	1.50	1.24	1.09	0.70	-17.4%	-27.5%	-53.7%
	Qva, Qvlc	32,904	1.29	1.22	1.18	1.07	-5.2%	-8.4%	-16.9%
B-B'	Qva	9,724	3.20	1.54	1.06	0.50	-51.9%	-67.0%	-84.4%
	Qva	30,922	2.45	1.54	1.26	0.76	-37.3%	-48.7%	-69.2%
C-C'	Qva	15,974	1.39	1.29	1.21	0.95	-7.0%	-13.2%	-31.4%
	Qva, Qvlc	32,933	1.46	1.41	1.36	1.17	-3.0%	-7.0%	-19.5%
D-D'	Qva	3,409	1.50	1.49	1.44	1.12	-0.4%	-4.3%	-25.1%
	Qva,Qvlc,Qob	224,072	1.30	1.30	1.28	1.25	-0.4%	-1.4%	-4.1%
	Qvlc,Qob	16,030	1.29	1.26	1.28	1.28	-2.3%	-1.3%	-1.3%

1990; Higgins and Osterkamp, 1990). Rainfall-induced high pore pressures in Fairmount Gulch and other drainages likely play an important role in mass wasting and erosional processes other than deep-seated landsliding, such as seepage erosion and shallow colluvial landslides.

Our simulations assess slope stability prior to failure and thus are designed to predict the locations of first-time failures. There are several possible reasons why our simulations do not correlate completely with historically active mapped landslides. The mapped landslides (Youngmann, 1979; Wait, 2001) are older or recent landslide deposits that have altered the topography of the preslide bluff. Some of these landslides deposits, such as Alki Avenue and Bonair Drive, have been active in the last few decades and occupy gentler slopes on a topographic bench above Qvlc. As such, these features are not likely to be identified as relatively unstable ground in our slope-stability analysis. These landslides are also probably influenced by factors not directly accounted for in our simulations, such as different patterns of ground-water flow in colluvium or lower residual strength properties in already-failed materials. Despite these factors, our results for very large volumes identify some sites of historical landslide deposits as having low stability (fig. 34). In addition, the results identify areas adjacent to some of these historical landslides as relatively unstable ground. For example, the area north of the Bonair Drive landslide and on the southern end of the California Way SW landslide have stability within 10 percent of the minimum factor of safety. These areas may be prone to future instability.

In contrast to models for shallow landsliding in Seattle (for example, Montgomery and others, 2001; Harp and others, 2006), our 3-D analysis provides a picture of stability significantly different from a slope map, because we integrate the influence of slope over large areas and include the influence of 3-D pore pressures. Other methods can identify large landslide complexes or landslide scarps along a large portion of the bluff (Schulz, 2004; Troost and others, 2005), but they do not delineate which parts of the bluff may be currently more stable than others.

Conclusions

Landslides on coastal bluffs throughout the world pose hazards to lives and property. The analysis tools presented here offer a method to quantify the influence of ground water, which is a common factor contributing to movement of deep-seated landslides on bluffs of Puget Sound (Tubbs 1974, 1975; Laprade and others, 2000) and elsewhere in the world (for example, Terzaghi, 1950; Sterrett and Edil, 1982; Higgins and Osterkamp, 1990; Norris and Back, 1990; Jaffe and others, 1998). We couple a 3-D ground-water model with a 3-D slope-stability analysis and incorporate variable material strengths, topography, and pore pressures. We extensively search a DEM for potential arcuate failures within a specified volume range and calculate a factor of safety (*F*) for each potential failure

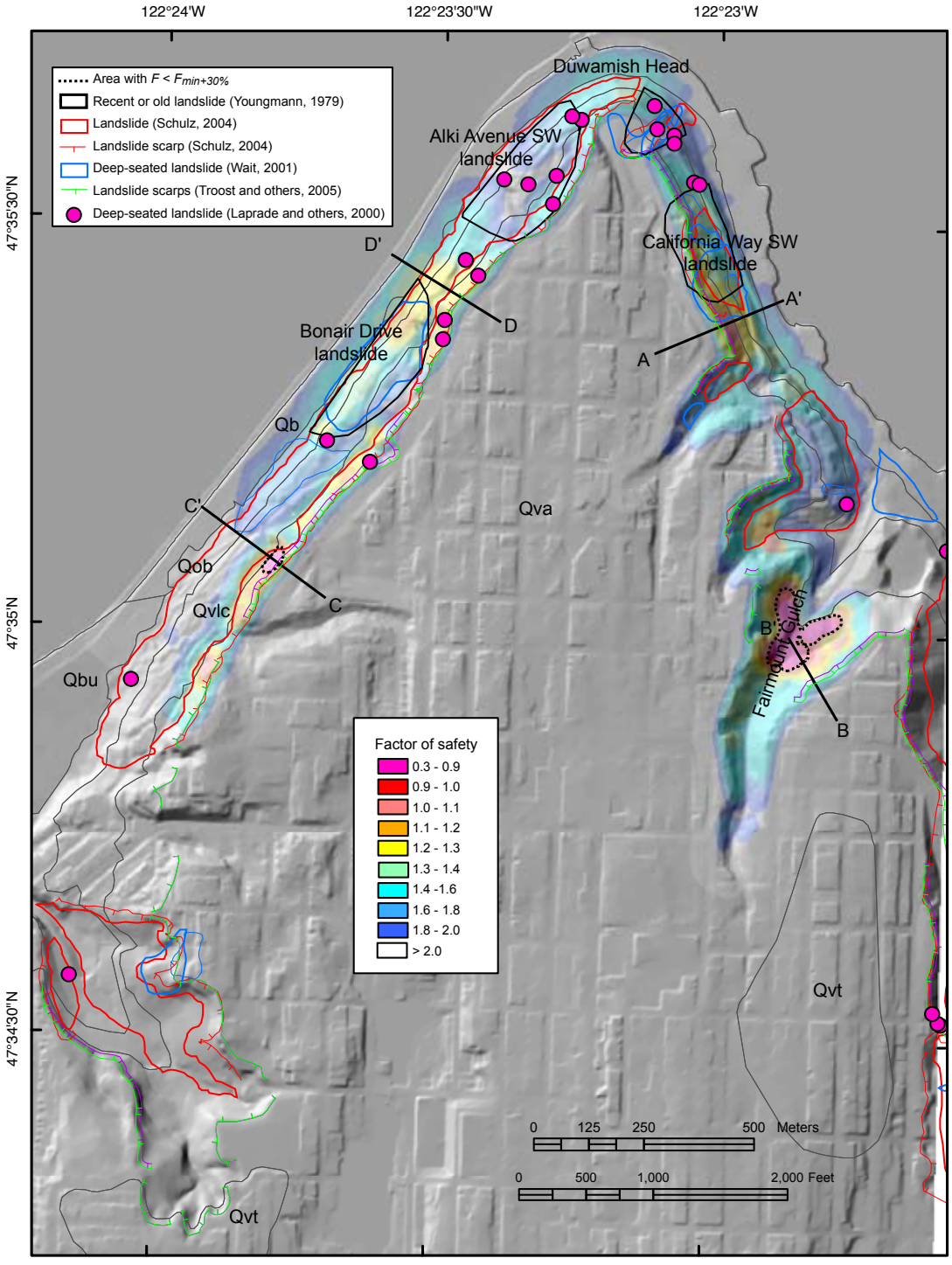

Figure 33. Map image showing factor of safety *(F)* for critical surfaces with volumes between 3,000 and 30,000 m^3, using average rainy-season recharge. The image shows mapped landslides (Youngmann, 1979; Laprade and others, 2000; Wait 2001; Schulz, 2004; Troost and others, 2005) compared with areas of relatively low factor of safety *($F < F_{min+30\%}$)*. Geologic contacts shown as gray lines. Cross-section locations for figure 32 are shown. See figure 3 for explanation of geologic unit symbols.

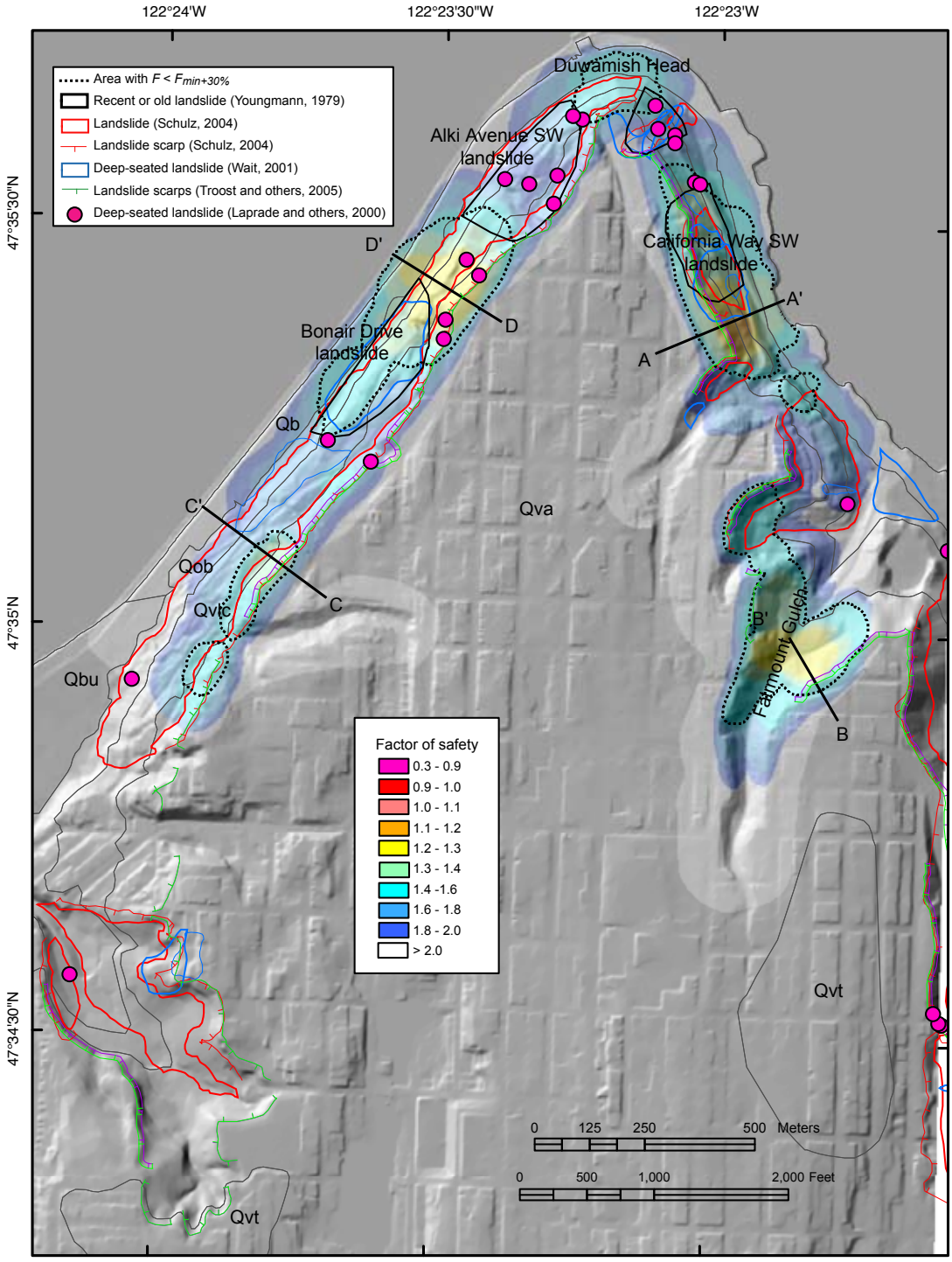

Figure 34. Map image showing factor of safety *(F)* for critical surfaces with volumes between 30,000 and 300,000 m^3, using average rainy-season recharge. The image shows mapped landslides (Youngmann, 1979; Laprade and others, 2000; Wait 2001; Schulz, 2004; Troost and others, 2005) compared with areas of relatively low factor of safety *($F < F_{min+30\%}$)*. Geologic contacts shown as gray lines. Cross-section locations for figure 32 are shown. See figure 3 for explanation of geologic unit symbols.

surface, while keeping track of the least-stable or critical surfaces for each DEM node. Our results include maps of predicted relative slope stability for the coastal bluff and associated volumes for the critical surfaces at each DEM node.

Our analysis for coastal bluffs in a study area near Alki Point and Duwamish Head in Seattle, Washington, leads to the following observations:

(1) Results obtained using dry conditions identified relatively unstable areas in locally steep portions of the landscape in all of the geologic units but did not agree with observations that landslides commonly have occurred near the contact between the advance outwash deposits (Qva) and the Lawton Clay Member (Qvlc).

(2) With the addition of 3-D pore pressures calculated from a ground-water model, stability maps include the influence of a perched ground-water table where Qva overlies Qvlc. A perched water table contributes to slope instability and leads to the occurrence of landslides of all types, including deep-seated landslides, near the contact between these geologic units. Our factor-of-safety maps identify areas where the modeled pore pressures are high and the bluff is steep, areas that constitute potential source areas for future large, deep-seated landslides. With the addition of 3-D pore pressures to our slope-stability analysis, elevated pore pressures in Qva shift the locations of the least-stable potential failures away from locally steep portions of the landscape to areas in Qva or near the contact between Qva and Qvlc. These locations agree with historical observations, thereby providing a more realistic estimate of where large deep-seated landslides are likely to occur in the future. The results using average rainy-season recharge and extremely large volume potential failures indicate low stability at two historically active landslides—Bonair Drive landslide and the California Way SW landslide—as well as some areas adjacent to these landslides. Some of the areas with the lowest stability

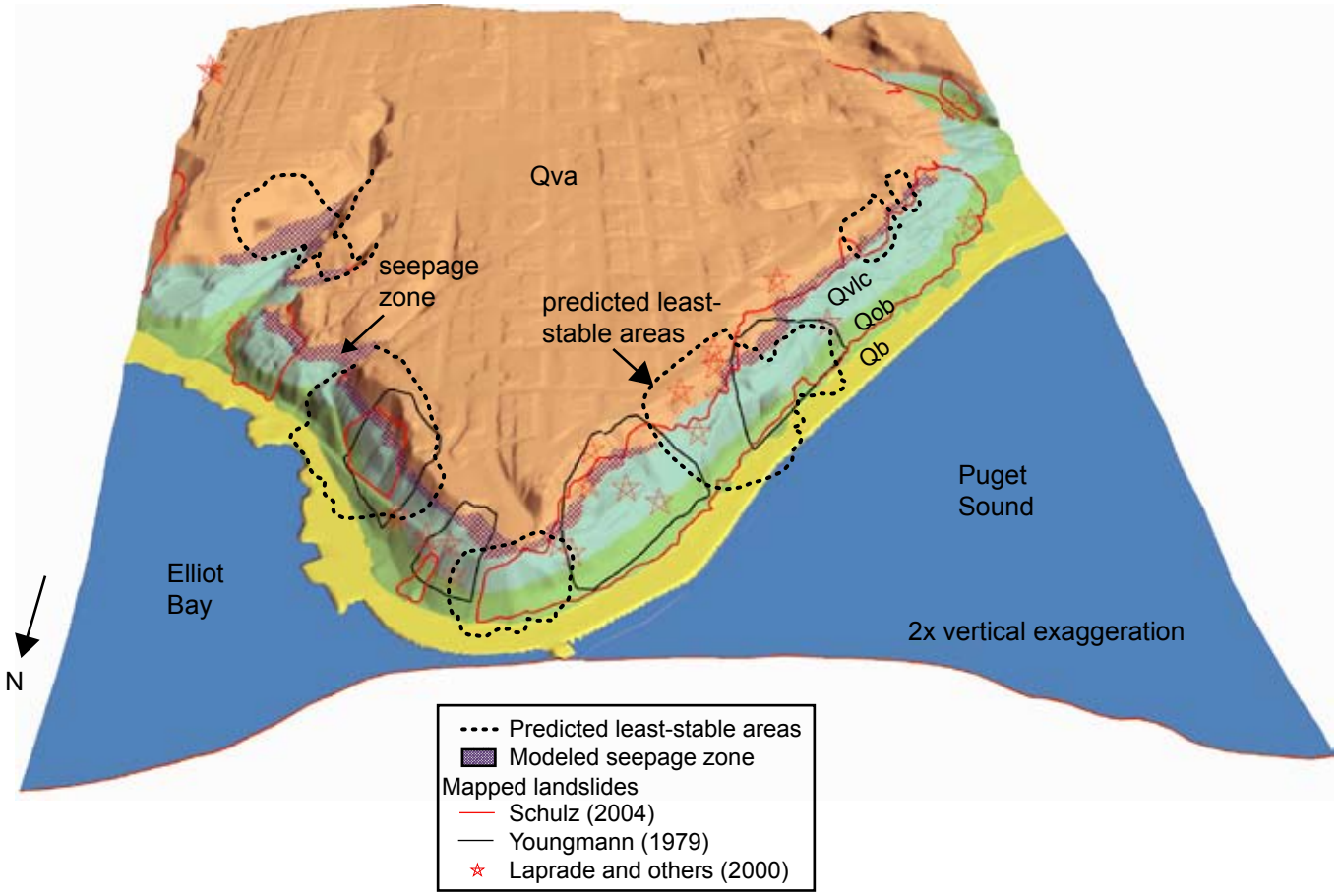

Figure 35. Image showing 3-D perspective view of landslides mapped by Youngmann (1979), Laprade and others (2000), and Schulz (2004), geologic units, seepage zone for average rainy-season recharge, and slope-stability results for very large volume potential failures and average rainy-season recharge. Red outline highlights the areas of relatively low factor of safety *($F < F_{min+30\%}$)*. See figure 3 for explanation of geologic unit symbols.

are the steeper areas adjacent to these historically active landslides.

(3) Our method can simulate potential failures over a wide range of volumes and geologic units. The potential failures resemble historical landslides in cross section. Although our approach cannot replace site-specific field investigations, our analysis tools can help identify parts of a slope that are potentially susceptible to deep-seated landsliding. The methods used in this study can be applied to coastal or inland landscapes in other areas of the world.

Acknowledgments

We thank Steve Ellen and William Schulz for their insightful reviews of this manuscript.

References Cited

Anderson, M.P., and Woessner, W.W., 1992, Applied groundwater modeling, simulation of flow and advective transport: San Diego, Academic Press, Inc., 381 p.

Baker, V.R., Kochel, R.C., Laily, J.E., and Howard, A.D., 1990, Spring sapping and valley network development, *in* Higgins, C.G., and Coates, D.R., eds., Groundwater geomorphology—the role of subsurface water in earth-surface processes and landforms: Geological Society of America Special Paper 252, p. 235-266.

Bates, R.L., and Jackson, J.A., eds., 1980, Glossary of geology: Falls Church, Virginia, American Geological Institute, 749 p.

Baum, R.L., Chleborad, A.F., and Schuster, R.L., 1998, Landslides triggered by the winter 1996-97 storms in the Puget Lowland, Washington: U.S. Geological Survey Open-File Report 98-239, 16 p.

Baum, R.L., Harp, E.L., and Hultman, W.A., 2000, Map showing recent and historical landslide activity on coastal bluffs of Puget Sound between Shilshole Bay and Everett, Washington: USGS Miscellaneous Field Studies Map 2346, 1 sheet, 1:24000.

Bird, E.C.F., and Schwartz, M.L., eds., 1985, The world's coastline: New York, Van Nostrand Reinhold Company, Inc., 1071 p.

Bishop, A.W., 1955, The use of slip circles in the stability analysis of slopes: Geotechnique, v. 5, p. 7-17.

Bromhead, E.N., Ibsen, M-L., Papanastassiou, X., and Zemichael, A.A, 2001, Three-dimensional stability analysis of a coastal landslide at Hanover Point, Isle of Wight: Quarterly Journal of Engineering Geology and Hydrogeology, v. 35, p. 79-88.

Chleborad, A.F., 2000, A method for anticipating the occurrence of precipitation-induced landslides in Seattle, Washington: U.S. Geological Survey Open-File Report 00-469, 29 p.

Chleborad, A.F., 2003, Preliminary evaluation of a precipitation threshold for anticipating the occurrence of landslides in the Seattle, Washington, Area: U.S. Geological Survey Open-File Report 03-463 [http://pubs.usgs.gov/of/2003/ofr-03-463/, last accessed 4/10/2007].

Debray, S., and Savage, W.Z., 2001, A preliminary finite-element analysis of a shallow landslide in the Alki Area of Seattle, Washington: U.S. Geological Survey Open-File Report 01-0357 [http://pubs.usgs.gov/of/2001/ofr-01-0357/, last accessed 4/10/2007].

Dunne, T., 1990, Hydrology, mechanics, and geomorphic implications of erosion by subsurface flow, *in* Higgins, C.G., and Coates, D.R., eds., Groundwater geomorphology—the role of subsurface water in earth-surface processes and landforms: Geological Society of America Special Paper 252, p. 1-28.

Emery, K.O., and Kuhn, G.G., 1982, Sea cliffs; their processes, profiles, and classification: Geological Society of America Bulletin, v. 93, p. 644-54.

Fabritz, J., Massmann, J., and Booth, D., 1998, Development of a three-dimensional, numerical groundwater flow model for the Duwamish River Basin, Duwamish Basin Groundwater Pathways: Center for Urban Water Resources Management, Department of Civil and Environmental Engineering, University of Washington, Seattle, WA [http://depts.washington.edu/cwws/Research/Reports/rc1.pdf, last accessed 4/10/2007].

Freeze, R.A., and Cherry, J.A., 1979, Groundwater: Englewood Cliffs, N.J., Prentice Hall, 804 p.

Galster, R.W., and Laprade, W.T., 1991, Geology of Seattle, Washington, United States of America: Bulletin of the Association of Engineering Geologists, v. 28, no. 3, p. 235-302.

Gerstel, W.J., Brunenego, M.J., Lingley, W.S., Logan, R.L., Shipman, H., and Walsh, T.J, 1997, Puget sound bluffs—the where, why, and when of landslides following the holiday 1996/97 storms: Washington Geology, v. 25, no. 1, p. 17-31 [http://www.dnr.wa.gov/geology/pugetls.htm, last accessed July 20, 2007].

Godt, J.W., 2004, Observed and modeled rainfall conditions for shallow landsliding in the Seattle, Washington Area: Univ. Colorado Ph.D thesis, 150 p.

Hampton, M.A., and Griggs, G.B., eds., 2004, Formation, evolution, and stability of coastal cliffs—status and trends: U.S. Geological Survey Professional Paper 1693, 129 p. [http://pubs.usgs.gov/pp/pp1693/, last accessed 4/10/2007].

Harbaugh, A.W., Banta, E.R., Hill, M.C., and McDonald, M.G., 2000, MODFLOW-2000, the U.S. Geolocial Survey modular ground-water model—user guide to modularization concepts and the ground-water flow process: U.S. Geological Survey Open-File Report 00-92, 121 p.

Harp, E.L., Chleborad, A.F., Schuster, R.L., Cannon, S.H., Reid, M.E., and Wilson, R.C., 1996, Landslides and landslide hazards in Washington State due to February 5-9 storm: U.S. Geological Survey Administrative Report, 29 p.

Harp, E.L, Michael, J.A., and Laprade, W.T, 2006, Shallow-Landslide Hazard Map of Seattle, Washington, U.S. Geological Survey Open-File Report 2006-1139 [http://pubs.usgs.gov/of/2006/1139/, last accessed 4/10/2007].

Haugerud, R.A., Harding, D.J., Johnson, S.Y., Harless, J.L., Weaver, C.S., Sherrod, B.L., 2003, High-resolution Lidar topography of the Puget Lowland, Washington—a bonanza for earth science: GSA Today, v. 13, no. 6, p. 4–10.

Higgins, C.G., Hill, B.R., and Lehre, A.K., 1990, Gully development, *in* Higgins, C.G., and Coates, D.R., eds., Groundwater geomorphology—the role of subsurface water in earth-surface processes and landforms: Geological Society of America Special Paper 252, p. 139-156.

Higgins, C.G., and Osterkamp, W.R., 1990, Seepage-induced cliff recession and regional denudation, *in* Higgins, C.G., and Coates, D.R., eds., Groundwater geomorphology – the role of subsurface water in earth-surface processes and landforms: Geological Society of America Special Paper 252, p. 291-318.

Hungr, O., 1987, An extension of Bishop's simplified method of slope stability analysis to three dimensions: Geotechnique, v. 37, p.113-117.

Jaffe, B., Kayen, R., Gibbons, H., Hendley, J.W., II, and Stauffer, P.H., 1998, Popular beach disappears underwater in huge coastal landslide—Sleeping Bear Dunes, Michigan: U.S. Geological Survey Fact Sheet 020-98 [http://pubs.usgs.gov/fs/1998/fs020-98/, last accessed 4/10/2007].

Jones, M.A., 1999, Geologic framework for the Puget Sound Aquifer System, Washington and British Columbia: U.S. Geological Survey Professional Paper 1424-C, 31 p.

Laprade, W.T., Kirkland, T.E., Nashem, W.D., and Robertson, C.A., 2000, Seattle Landslide Study: Shannon and Wilson, Inc., Internal Report W-7992-01, 164 p.

McDonald, M.G., and Harbaugh, A.W., 1988, A modular three-dimensional finite difference groundwater flow model: Techniques of Water-Resources Investigations of the United States Geological Survey, book 6, chapter A1, Modeling Techniques.

Montgomery, D.R., Greenberg, H.M., Laprade, W.T., and Nashem, W.D., 2001, Sliding in Seattle: Test of a model of shallow landsliding potential in an urban environment, *in* Wigmosta, M.S., and Burges, S.J., eds., Land use and watersheds, human influence on hydrology and geomorphology in urban and forest areas: Water Science and Application, v. 2, p. 59-73.

Morgan, D.S., and Jones, J.L., 1996, Numerical model analysis of the effects of ground-water withdrawals on discharge to streams and springs in small basins typical of the Puget Sound Lowland, Washington: U.S. Geological Survey Open-File Report 95-470 [http://wa.water.usgs.gov/pubs/ofr/ofr.95-470/index.htm, last accessed 4/10/2007].

Mullineaux, D. R., Waldron, H. H., and Rubin, M., 1965, Stratigraphy and chronology of late interglacial and early Vashon glacial time in the Seattle area, Washington: U.S. Geological Survey Bulletin 1194-O, 10 p.

Norris, R.M., and Back, W., 1990, Erosion of seacliffs by groundwater, *in* Higgins, C.G., and Coates, eds., D.R., Groundwater geomorphology—the role of subsurface water in earth-surface processes and landforms: Geological Society of America Special Paper 252, p. 283-290.

Reid, M.E., Christian, S.B., and Brien, D.L., 2000, Gravitational stability of three-dimensional stratovolcano edifices: Journal of Geophysical Research, v. 105, no. B3, p. 6043-6056.

Sapik, D.B., Bortleson, G.C., Drost, B.W., Jones, M.A., and Prych, E.A., 1988, Ground-water resources and simulation of flow in aquifers containing freshwater and seawater, Island County, Washington: U.S. Geological Survey Water-Resources Investigations Report 87-4182, 66 p.

Savage, W.Z., Baum, R.L., Morrissey, M.M., and Arndt, B.P., 2000a, Finite-element analysis of the Woodway Landslide, Washington: U.S. Geological Survey Bulletin 2180 [http://geology.cr.usgs.gov/pub/bulletins/2180, last accessed 4/10/2007].

Savage,W.Z., Morrissey, M.M, and Baum, R.L., 2000b, Geotechnical properties for landslide-prone Seattle-area glacial deposits: U.S. Geological Survey Open-File Report 00-228, 5 p.

Schulz, W.H., 2003, Modeling distribution of colluvium and shallow groundwater on landslide-susceptible slopes for parts of Seattle, Washington: Geological Survey of America Abstracts with Programs, v. 36, no. 5, p.332.

Schulz, W.H., 2004, Landslides mapped using LIDAR imagery, Seattle, WA: U.S. Geological Survey Open-file Report 2004-1396 [http://pubs.usgs.gov/of/2004/1396/, last accessed 4/10/2007].

Shannon &Wilson, Inc., 2000, Geotechnical Report, Alki Avenue / Duwamish Head Stabilization Project, Seattle, WA, submitted to Seattle Public Utilities.

Shipman, H., 2001, Coastal landsliding on Puget Sound: a review of landslides occurring between 1996 and 1999: Shorelands and Environmental Assistance Program, Washington Department of Ecology, Olympia Publication 01-06-019, 87 p.

Sterrett, R.J., and Edil, T.B., 1982, Ground-water flow systems and stability of a slope: Groundwater, v. 20, p. 5-11.

Terrapoint, 2000-2004, LIDAR Bare Earth DEM [computer file]: The Woodlands, Texas, available from Puget Sound LIDAR Consortium, Seattle, Wash. [http://pugetsoundlidar.ess.washington.edu/, last accessed 4/10/2007].

Terzaghi, K., 1950, Mechanism of landslides, *in* Paige, Sidney, chairman, Application of geology to engineering practice–Berkey volume: New York, The Geological Society of America, p. 83-123.

Troost, K.G., Booth, D.B., Wisher, A.P., and Shimel, S.A., 2005, The geologic map of Seattle–A progress report: U.S. Geological Survey Open-file Report 2005-1252 [http://pubs.usgs.gov/of/2005/1252/, last accessed 4/10/2007].

Tubbs, D.W., 1974, Landslides in Seattle: Washington Division of Geology and Earth Resources Information

Circular no. 52, 15 p.
Tubbs, D.W., 1975, Causes, mechanisms and prediction of landsliding in Seattle: Univ. Washington Ph.D. thesis, 88 p.
Tubbs, D.W., and Dunne, T., 1977, Geologic Hazards in Seattle, A field guide for the Geological Society of America Annual Meeting: [http://www.tubbs.com/geohaz77/geohaz77.htm, last accessed 4/10/2007].
Vaccaro, J.J., 1992, Plan of study for the Puget-Willamette Lowland regional aquifer-system analysis, Western Washington and Western Oregon: U.S. Geological Survey Water Resources Investigations Report 91-4189, 41 p.
Vaccaro, J.J., Hansen, Jr., A.J., and Jones, M.A., 1998, Hydrogeologic framework of the Puget Sound Aquifer System, Washington and British Columbia: U.S. Geological Survey Professional Paper 1424-D, 77 p., 1 sheet.
Varnes, D.J., 1958, Landslide types and processes, *in* Eckel, E., ed. Landslides and engineering practice: Highway research Board Special Report 29, Washington, D.C., p. 20-47.
Wait, T.C., 2001, Characteristics of Deep-Seated Landslides in Seattle, Washington: Colorado School of Mines, Masters thesis, 141 p., 3 plates.
Woodward, D.G., Packard, F.A., Dion, N.P., and Sumioka, S.S., 1995, Occurrence and quality of ground water in Southwestern King County, Washington: U.S. Geological Survey Water-Resources Investigations Report 92-4098, 69 p.
Xing, Z., 1988, Three-dimensional stability analysis of concave slopes in plan view: Journal of Geotechnical Engineering, American Society Civil Engineers, v. 114, no. 6, p. 658-671.
Youngmann, C., ed., 1979, King County—Coastal zone atlas of Washington: Olympia, Wash., Washington Department of Ecology [http://www.ecy.wa.gov/services/gis/data/data.htm, last accessed 4/10/2007].

Appendix A. DEM Comparison

This appendix compares the results of our 3-D slope-stability analysis under dry conditions using two different DEMs—(1) a 10-ft (~ 3-m) resolution DEM generated by using photogrammetry (City of Seattle, unpub. data), and (2) a 6-ft (~ 2-m) resolution DEM generated from light detection and ranging, LIDAR (Terrapoint, 2000-2004). In order to compare the results cell by cell, the LIDAR DEM was resampled to 10-ft resolution.

Slopes calculated from the two DEMs can vary significantly when comparing individual cells but have a similar overall pattern (figs. 36 and 37). Some areas on the LIDAR DEM contain unnatural linear features as a result of artifacts from processing (fig. 37, areas labeled 1, 2, 3). Because the slope-stability analysis is sensitive to steep slopes on the bluff, we used a modified version of the DEM (Schulz, written commun., 2004) in which one area on the west bluff within our analysis window was smoothed (fig. 37, no. 1). This modification still did not completely remove the linear artifact.

We ran our slope-stability analysis with both DEMs and found that, for our moderately large volume search, small local variations in slope revealed by LIDAR produced some change in computed slope stability (figs. 38 and 39). However, for dry conditions, the location of the least-stable areas ($F < F_{min+10\%}$ and $F < F_{min+30\%}$) changes only slightly, and these changes would not affect our overall conclusions.

Although LIDAR can better represent the ground surface in areas such as Seattle that have significant vegetation cover (Haugerud and others, 2003), we chose to use the City of Seattle DEM generated from photogrammetric techniques for two reasons—(1) the photogrammetric DEM was the topographic base for the geologic mapping used in this analysis (Troost and others, 2005) and (2) the LIDAR DEM contains artifacts from processing of the original data that do not represent real features in the landscape.

Appendix B. Geologic Contacts

The surfaces defining geologic contacts are an essential component of most 3-D geologic models. In our analysis, we delineate the geologic units to assign appropriate geotechnical properties for each unit. The locations of these subsurface geologic contacts can also control the flow of ground water.

We want to honor the geologic contacts as mapped on the ground surface as closely as possible. We considered software packages that offered a variety of surface-creation routines, but some methods created surfaces that did not retain the original data points. We provide this appendix to describe our method and thereby help investigators in future endeavors.

We performed our analysis in the ESRI™ (Environmental Systems Research Institute) software, ArcGIS™ ArcInfo Workstation 8.x, using Grid commands, although similar methods should be available in other software packages. To create a contact surface, we interpolated, using an inverse-distance-weighted method, from the mapped geologic contacts to locations in the subsurface where the contact elevations were not available. This method honored the mapped contacts and created a smooth contact surface in the subsurface. Starting with a grid of elevations (the DEM) and a line coverage of geologic contacts at the land surface, we used five steps to create each surface—(1) add extra vertices to the line coverage so that there is at least one vertex in each grid cell; (2) convert the vertices to points; (3) extract elevation values at each point from the DEM; (4) if the coverage containing the geologic contacts extends beyond the DEM, remove points with null values; and (5) interpolate a surface using inverse-distance weighting.

Here is an example of a script using ArcGIS™ ArcInfo Workstation commands to generate a surface. We use ESRI's™ convention for the syntax of commands, where <geographic_data_set> refers to the name of a grid or coverage, and lines starting with "/*" are comments. The inputs are:

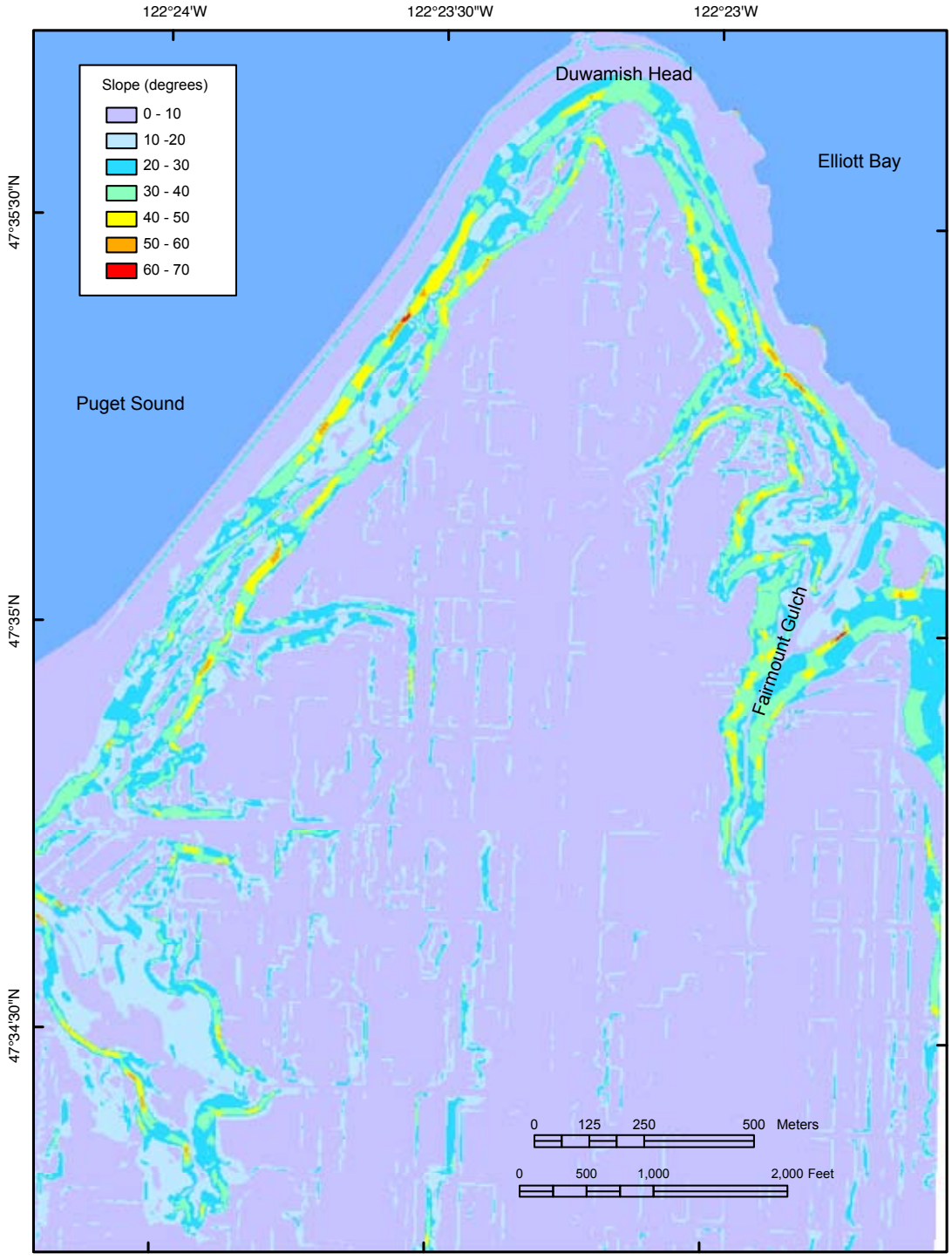

Figure 36. Slope map generated from digital elevation model (City of Seattle, unpub. data) of 10-ft (~3-m) resolution.

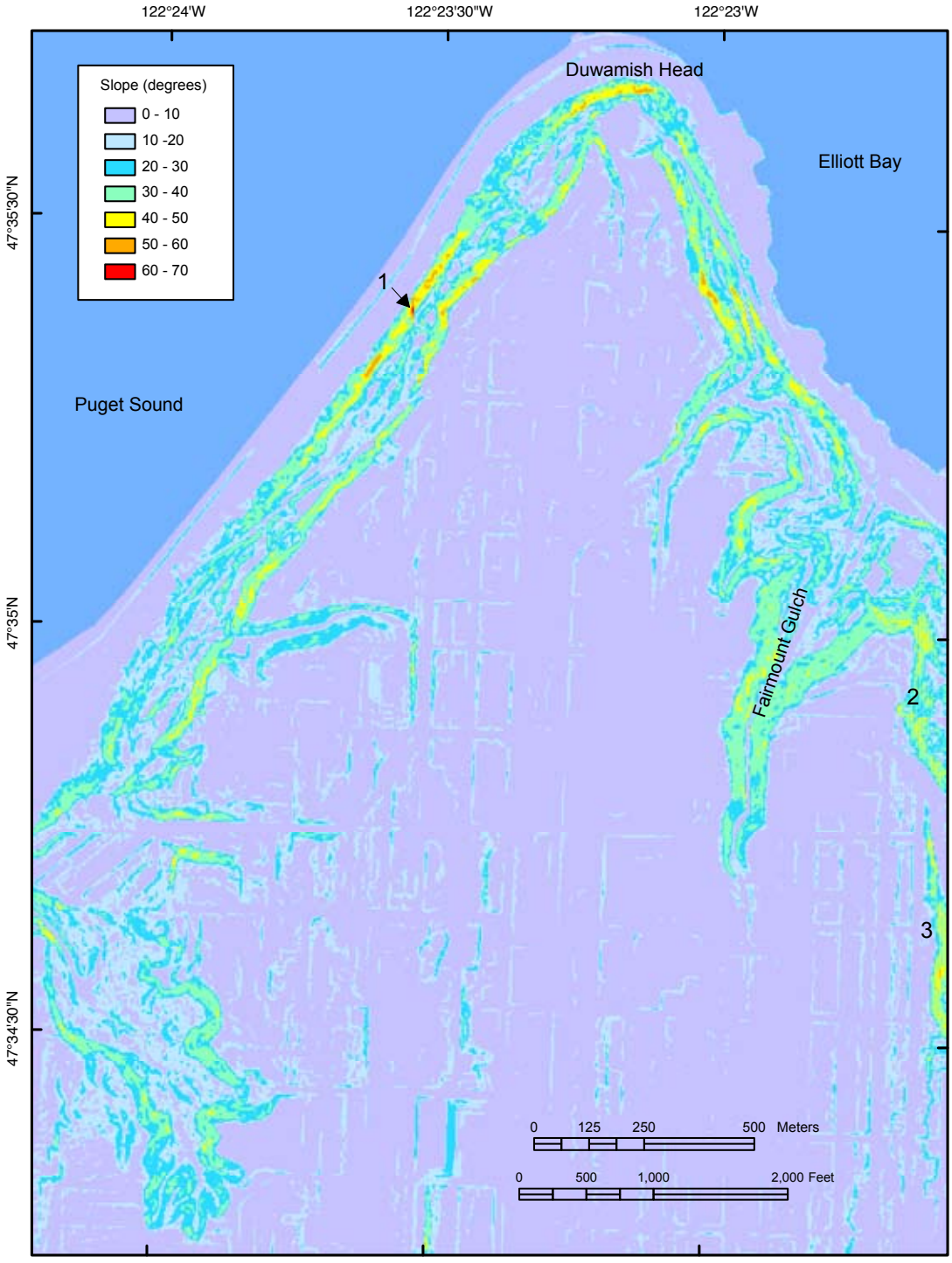

Figure 37. Slope map generated from light detection and ranging (LIDAR) digital elevation model (Terrapoint, 2000-2004) of 6-ft (~2-m) resolution resampled to 10-ft (~3-m) resolution. Numerals 1, 2, and 3 indicate areas with artifacts from processing of original data.

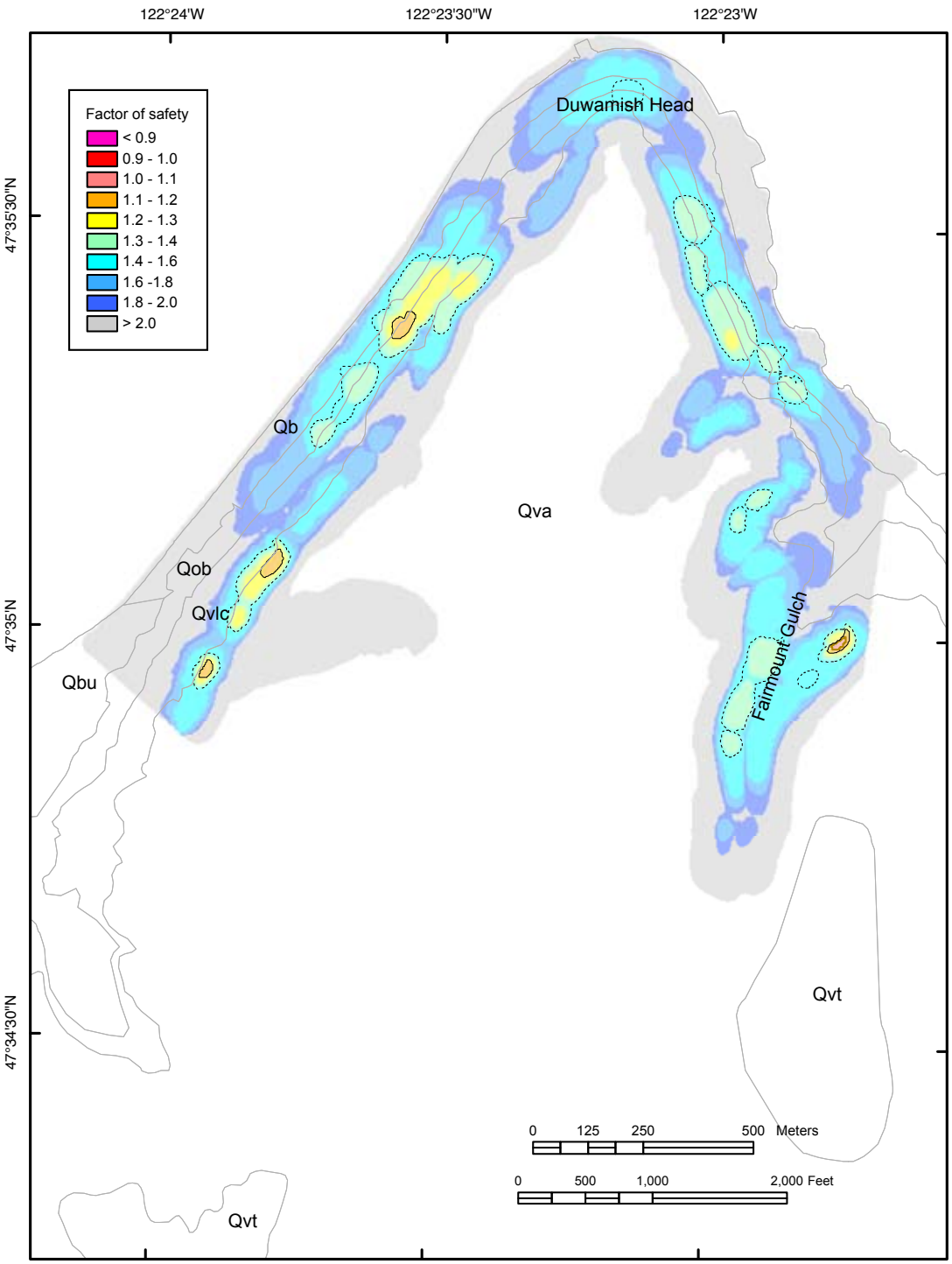

Figure 38. Factor of safety *(F)* for critical surfaces using City of Seattle 10-ft (~ 3-m) resolution digital elevation model (City of Seattle, unpub. data). *F* was calculated for dry conditions and volumes between 3,000 and 30,000 m^3. *F* is indicated by color, and areas of relatively low stability are outlined: $F < F_{min+10\%}$, solid black line, and $F < F_{min+30\%}$, dashed black line. Geologic contacts are shown as gray lines. See figure 3 for explanation of geologic unit symbols.

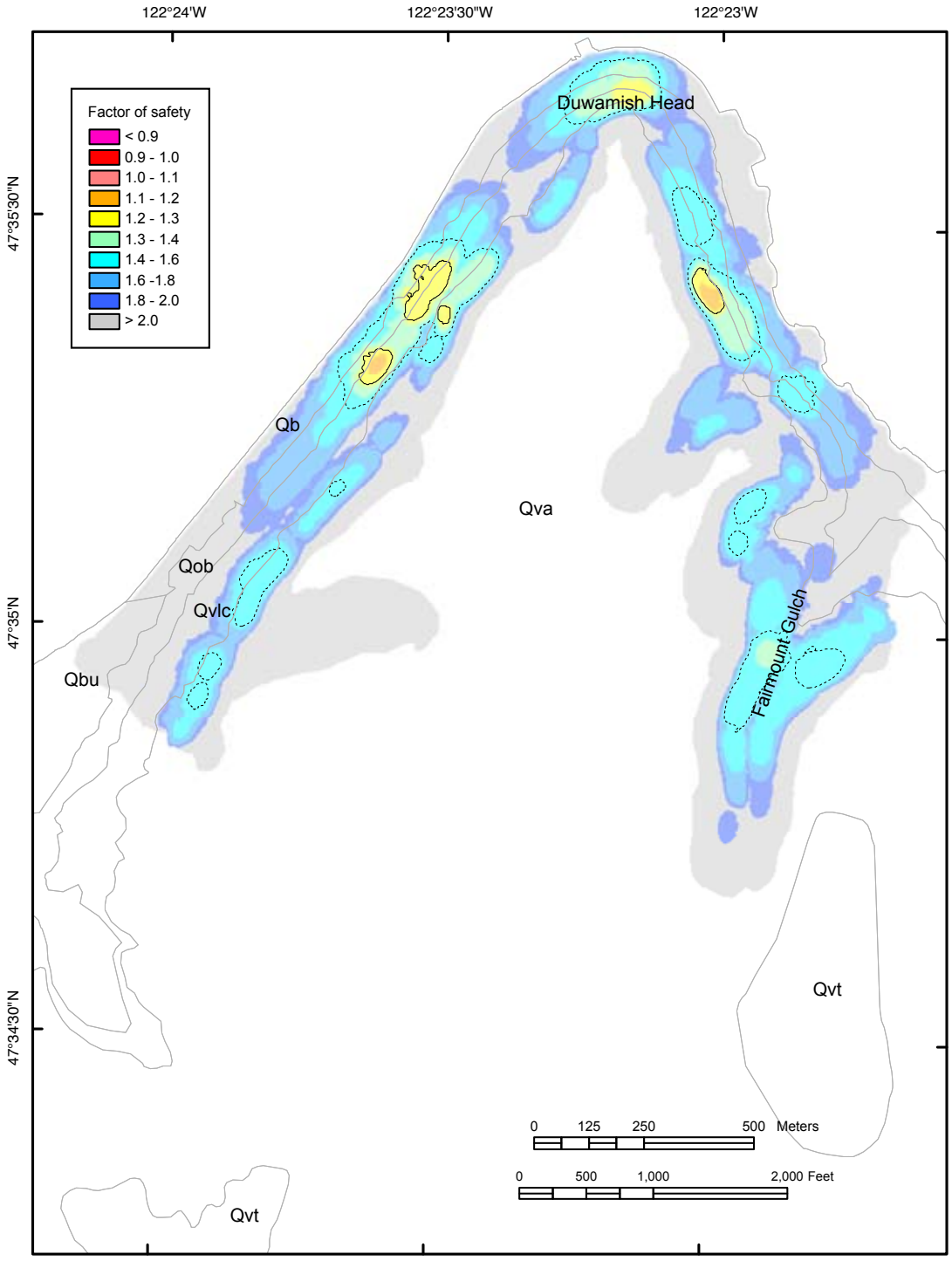

Figure 39. Factor of safety (F) for critical surfaces using LIDAR 6-ft (~2-m) resolution digital elevation model (Terrapoint, 2000-2004) resampled to 10-ft (~2-m) resolution. F was calculated for dry conditions and volumes between 3,000 and 30,000 m^3. F is indicated by color, and areas of relatively low stability are outlined: $F < F_{min+10\%}$, solid black line, and $F < F_{min+30\%}$, dashed black line. Geologic contacts are shown as gray lines. See figure 3 for explanation of geologic unit symbols.

<geocov> - line coverage of one mapped geologic contact,
<demgrid> - grid of land surface elevations (the DEM), and
<demclip> - optional grid for limiting the horizontal spatial extent of the surface
The commands are:

```
/* Add extra vertices to the lines describing a geologic contact, use an interval of 10 units.
densifyarc <geocov> <geocovdense> 10

/* Create a coverage, called geopt, containing points on the contact; note that spot_item can be any attribute of the coverage.
arcpoint <geocovdense> <geopt> line {spot_item}
/* Assign elevations to the points (from the DEM).
latticespot <demgrid> <geopt> elevation

/* If necessary, remove points outside of the extent of the DEM.
ae
edit <geopt>
ef point
sel for elevation = -9999
delete
save

/* Interpolate a surface using known elevation at the geologic contact
grid
setwindow <demclip> <demgrid>
setcell 10
<geoidw> = pointinterp(<geopt>,elevation,#,idw)

/* If necessary, clip layers to the extent of the area of the geologic unit; in this example, assign null
/* values to the area outside of extent of geologic unit defined by geology grid where the area of
/* the geologic unit is defined by grid defining the extent of the geologic unit (<geogrid>).
<geobot>  = con (<geogrd> == 1, <geoidw>)
/* Repeat these commands for each geologic unit.
```

Appendix C. Sensitivity to Strengths

For the slope-stability analysis presented in this paper, we used typical values (Harp and others, 2006) for the strength of geologic units (table 4). This appendix describes the sensitivity of the slope-stability results using lower strength values. Because we are interested in a conservative scenario, one that will result in lower stability, we did not calculate stability results using higher strength properties.

Under dry conditions, slope instability is not commonly observed along the Puget Sound bluffs, and factor of safety throughout the bluffs should be greater than one. Therefore, the strength properties that result in a factor of safety of approximately one under dry conditions represent a lower limit for the strengths considered. For Qva, this lower limit is approximately $c' = 6$ kPa and $\phi' = 32°$; for Qvlc the lower limit is $c' = 20$ kPa and $\phi' = 15°$. We used these lower limits on strengths to compare the effects of lowered strengths in Qva and Qvlc, the units where our least-stable surfaces occur with base-case strengths, discussed above. We examined the resulting factors of safety for critical surfaces using our moderately large volume search and average rainy-season recharge (fig. 40).

Compared to base-case strengths (fig. 40*A*), lowering the strength of Qva (fig. 40*B*) decreases the absolute factor of safety values but showed minimal change in location of the least-stable potential failures. With lower strength in Qvlc (fig. 40*C*), the absolute factors of safety decrease and the least-stable potential failures shifted to areas of highly elevated pore pressure in Qva, steep areas of Qvlc, or steep areas near the contact between Qva and Qvlc. When we lowered both the strength of Qva and Qvlc (fig. 40*D*), the least-stable surfaces occurred in areas of Qva where pore pressures are elevated and the ground is steep. In these comparisons using average rainy-season recharge, absolute factor of safety decreased with lowered strength properties. However, with lowered strength in Qva or lowered strengths in Qva and Qvlc, the areas of lowest stability changed only minimally; locations of the least-stable surfaces changed significantly only when strength of Qvlc alone was lowered.

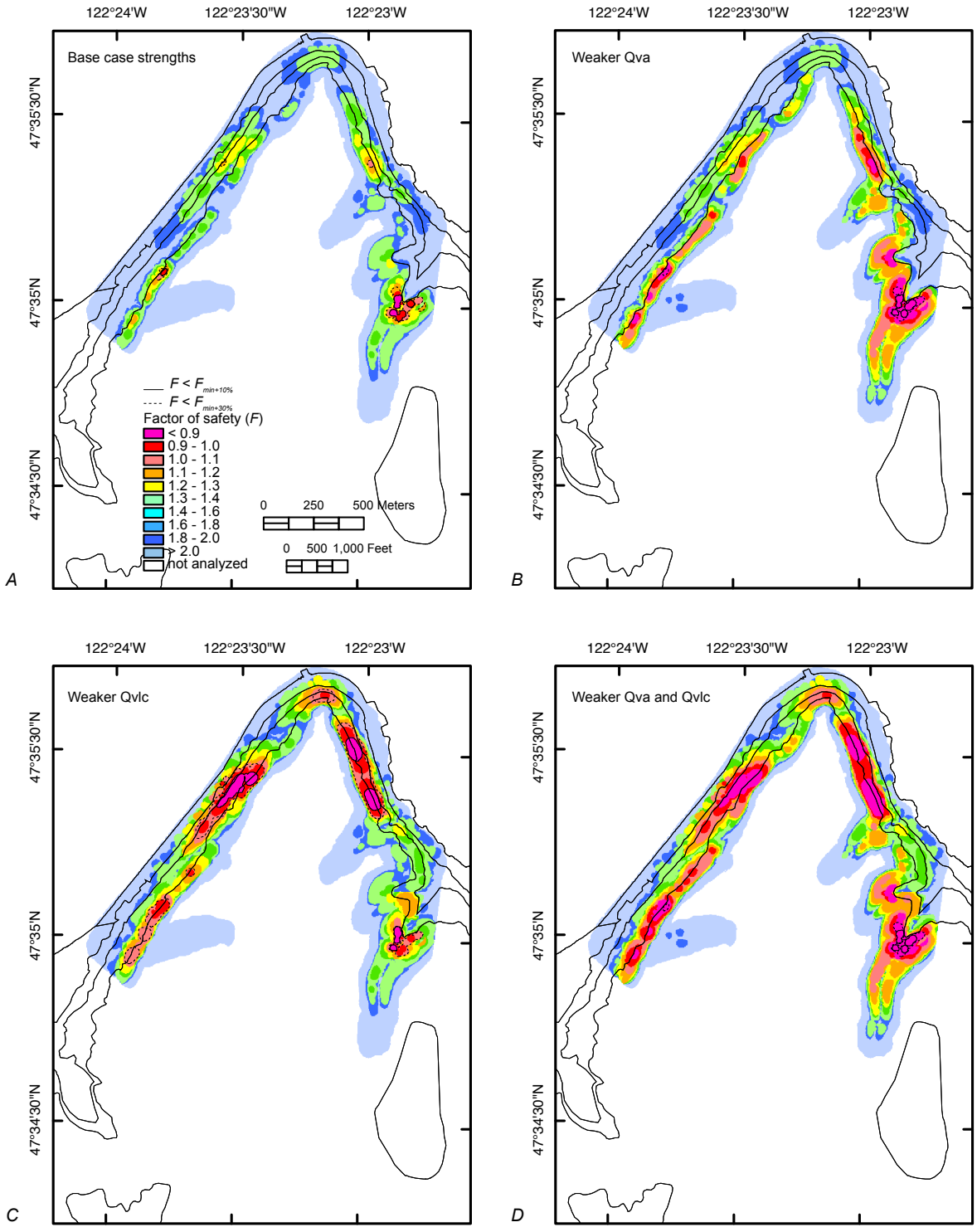

Figure 40. Factor of safety *(F)* for critical surfaces with associated volumes between 3,000 and 30,000 m^3 with average rainy-season recharge. *F* is indicated by color, and areas of relatively low stability are outlined: $F < F_{min+10\%}$, solid black line, and $F < F_{min+30\%}$, dashed black line. Results are shown for *(A)* base-case strengths, *(B)* lowered Qva strengths, *(C)* lowered Qvlc strengths, and *(D)* lowered Qva and Qvlc strengths combined. Geologic contacts are shown as black lines. See figure 3 for explanation of geologic unit symbols.